

**FINITE ELEMENT MODELING OF NiTiNOL IN TRANSCATHETER
AORTIC VALVE IMPLANTATION: ASSESSING MATERIAL
INFLUENCE ON SIMULATION RELIABILITY**

VERIFICATION, VALIDATION, AND UNCERTAINTY QUANTIFICATION OF
NiTiNOL BEHAVIOR IN TAVI COMPUTATIONAL MODELING

**FINITE ELEMENT MODELING OF NiTiNOL IN TRANSCATHETER
AORTIC VALVE IMPLANTATION: ASSESSING MATERIAL
INFLUENCE ON SIMULATION RELIABILITY**

**VERIFICATION, VALIDATION, AND UNCERTAINTY QUANTIFICATION OF
NiTiNOL BEHAVIOR IN TAVI COMPUTATIONAL MODELING**

by

Lorenzo FERILLI

Supervisory Team:

Technische Universiteit Delft

Dr. Mohammad Mirzaali Mazandarani

Dr. Behrooz Fereidoonzehad

4RealSim Services B.V.

Dr. Nils Götzen

Tahir Turgut

In partial fulfilment of the requirements for the degree of
Master of Science in Biomedical Engineering

Technische Universiteit Delft, The Netherlands, 2025

CONTENTS

Acknowledgements	vii
Preface	ix
Abstract	xi
1. Introduction	1
1.1. Research background	2
1.2. Problem definition	3
1.3. Research question and goal of the study	4
2. Materials and methods	7
2.1. Experimental activities	8
2.1.1. Sample Geometrical Measurements	8
2.1.2. Experimental Validation of Friction Coefficients	9
2.1.3. Mechanical Testing of TAVI Components	11
2.2. FE modelling and computational simulation activities	13
2.2.1. Computational model(s) setup and categorization	13
2.2.2. Materials and interactions modelling	22
2.2.3. Simulation conditions and parameters	23
2.3. Verification, Validation and Uncertainty Quantification activities	26
2.3.1. Model verification processes	26
2.3.2. Model validation strategies	28
2.3.3. Hypothesis exploration analysis	29
3. Framework results	31
3.1. Experimental activities results	32
3.1.1. Samples geometrical measurements	32
3.1.2. Experimental validation of friction coefficients	33
3.1.3. Mechanical testing of TAVI components	33
3.2. FE modelling and computational simulation activities findings	36
3.2.1. Model development outcomes	36
3.2.2. Validation simulations data analysis	38
3.3. Verification, Validation and Uncertainty Quantification activities results	41
3.3.1. Model verification	41
3.3.2. Validation strategies	48
3.4. Transvalvular pressure simulation results	54
4. Results discussion	57
4.1. Findings and implications for the predictive accuracy of TAVI FE Modeling	58
4.2. Known limitations and future developments	59
5. Conclusions	61
5.1. Conclusions	62

A. Appendix - Experimental test devices	67
A.1. Fastening device design	68
B. Appendix - Additional tables	71
B.1. Tables Chapter 2 - Materials and methods	72
B.2. Tables Chapter 3 - Results	75
C. List of Tables	81
D. Appendix - Additional figures	85
D.1. Figures Chapter 2 - Materials and methods	86
D.2. Figures Chapter 3 - Results	89
E. List of Figures	95

ACKNOWLEDGEMENTS

This thesis marks the final step of an intense and rewarding journey, one that would not have been possible without the support, guidance, and encouragement of many people along the way.

First and foremost, I would like to express my deepest gratitude to 4RealSim Services B.V. (Groene Dijk 2B, 3401 NJ IJsselstein, The Netherlands), the company that provided the foundation for this research and welcomed me into their team with open arms. A special and heartfelt thanks goes to my company supervisors, Nils Götzen and Tahir Turgut, whose insight, experience, and invaluable suggestions were not only deeply appreciated but proved vital to the success of this project. Their mentorship helped shape both the technical and strategic aspects of this work, providing me with a deeper understanding of computational modeling and its real-world applications.

Beyond my direct supervisors, I sincerely thank the entire 4RealSim team: Vincent, Gaëtan, Omar, Joost, and Mark, for creating an environment that was professional, supportive, and welcoming from the very first day. Their expertise, team spirit, and encouragement played an essential role in making this experience truly special.

Academically, I owe a profound thank you to my TU Delft supervisors, Dr. Mohammad Mirzaali Mazandarani and Dr. Behrooz Fereidoonzehad, who have been instrumental in guiding this complex research from its earliest definition. Their invaluable support and expert advice throughout the planning, execution, and supervision of experimental activities, as well as during the writing phase, ensured that this project met the level of scientific rigor and precision it demanded. Their patience, critical feedback, and unwavering support have been a major driving force behind this work.

I would also like to acknowledge Xeltis B.V. (De Lismortel 31, 5612 AR Eindhoven, The Netherlands), the manufacturer of the investigated TAVI valve, whose design remains protected under copyright, and ADMEDES GmbH (Am Muehlbach 6, 75172 Pforzheim, Germany) for their essential contribution in performing the tensile stress tests and radial compression resistance tests on the NiTiNol alloy samples, which were instrumental in validating the computational models developed within this work.

This project was carried out within the framework of the SimInSitu project, an initiative supported by the Horizon 2020 European Research and Innovation Programme, which provided both financial and research backing for the experimental and computational investigations of which this study represents only an infinitesimal portion. The support of this initiative has been crucial in facilitating the development of advanced in silico methodologies for biomedical applications.

Beyond the academic and professional sphere, I wish to extend my heartfelt appreciation to the friends who have always been a source of inspiration, despite being scattered across Europe, each immersed in their own academic and professional journeys. A special mention goes to the Shogunato dell'Acquario group, for the countless moments of support and encouragement.

To my parents and my sister, who have patiently waited far too long to see the end of this thesis project—I can only say thank you for your unwavering support. To my girlfriend, Teodora, for standing by my side through every challenge, for her patience, and for enduring my complete absorption in

this work—your presence made all the difference. I could not have done this without you.

Finally, a special thanks to my colleagues from the PIP club, who tolerated my endless attempts to talk about this project, and to my flatmates from Vechtstraat 12, who provided a much-needed balance between academic dedication and everyday life.

To all those who, in one way or another, contributed to this journey, thank you.

Lorenzo Ferilli

PREFACE

The study of finite element modeling in transcatheter aortic valve implantation is a rapidly evolving field, merging computational mechanics with medical applications to push the boundaries of cardiovascular research. The idea of contributing to this field, even in a small way, has been an exciting and humbling challenge.

Despite substantial advancements in computational engineering, the biomedical sector has historically been cautious in adopting methods such as finite element analysis, even though these have long been established standards in other industries. This caution is well-founded since the stakes in medicine are often far higher, requiring extremely verified, safe, and well-established methodologies before clinical adoption. However, in recent years, regulatory agencies have begun recognizing the value of computer-based simulations, marking a turning point in how computational modeling is integrated into medical research. The potential to reduce dependence on human and animal experimentation by using simulation-based studies presents an exciting opportunity for scientific and clinical advancement.

With this shift, however, comes a critical responsibility. Before computational tools can be relied upon for medical decision-making, they must be thoroughly perfected, validated, and sharpened to meet the highest standards of accuracy and reliability. This research, in its own capacity, aimed to contribute to that goal by refining the credibility of finite element models in transcatheter valve applications, ensuring that simulation outcomes remain robust, reliable, and independent of solver assumptions or numerical artifacts.

This thesis is the result of months of research, experimentation, and problem-solving. From the start, the project required a significant amount of trial and error, with further refinements and adjustments needed at every iteration, far exceeding the initial effort that was planned. Integrating computational modeling with experimental validation proved both challenging and highly rewarding. Balancing simulation accuracy with real-world constraints, validating results against experimental data, and refining methodological assumptions made this an intense yet fascinating process.

Perhaps the greatest challenge was ensuring the credibility of the finite element model, where seemingly minor decisions such as mesh refinement, material parameter selection, and solver settings could significantly impact results. The task of integrating experimental findings into computational predictions required patience, iteration, and a critical approach to every assumption. Overcoming these hurdles has deepened my understanding of how computer-based methodologies can be applied in biomedical engineering, reinforcing the importance of validation at every step.

Aside from the technical aspects, this journey significantly contributed to my personal and professional growth. This experience provided me with a first-hand understanding of what it means to work in a professional setting, collaborating side by side with experts in the field for more than a year. It offered me the opportunity to see how research, industry expertise, and engineering solutions come together in a real-world environment. Looking back, I recognize that this experience was not just about developing a reliable model but also about refining the thought process behind scientific

problem-solving and learning how to navigate the challenges of professional research.

I hope that the insights presented here contribute, in some capacity, to the ongoing efforts in the field of cardiovascular modeling and inspire further research toward improving patient-specific solutions in transcatheter heart valve interventions.

ABSTRACT

The accuracy and reliability of finite element (FE) modeling for transcatheter aortic valve implantation (TAVI) devices are highly dependent on the selection of shape-memory alloy (SMA) material parameters. This study investigates the impact of NiTiNol material parameter variations on simulation outcomes by developing a fully verified and validated FE model. A bottom-up validation approach, following ASME guidelines, was implemented to ensure that results remained independent of numerical solver settings, discretization errors, and modeling assumptions. Experimental validation against an independent dataset demonstrated strong agreement in mechanical response, with deviations mainly observed under conditions of extreme deformation.

A sensitivity analysis was conducted by first obtaining NiTiNol material parameters via a Monte Carlo parameter-fitting survey performed on three experimental datasets provided by an external partner company. This analysis identified a material parameter variability of 5.34%, which was subsequently applied as a $\pm 5.34\%$ uncertainty range to assess its impact on the TAVI simulation results' reliability. Simulation outcomes within this variability range were compared against those generated using broader, literature-derived parameter ranges. Results revealed minimal sensitivity of phase transformation parameters under nominal loading conditions, except for Austenite Young's modulus (E_A), which exhibited a linear correlation with the normalized root mean square error (NRMSE). The influence of σ_{tS}^L (start transformation stress in tension) became more pronounced at higher E_A values, where a larger portion of the stent underwent phase transformation due to the strain-controlled nature of the system. Other tested parameters had negligible impact, reinforcing that deep phase transformations did not occur under the given physiological loading scenario.

The findings underscore the inapplicability of generic NiTiNol material properties from literature in case-dependent simulations, as non-case-specific values introduced up to 30% variability in mechanical response. This effect is expected to be even more pronounced in applications involving severe phase transformations, such as valve deployment and patient-specific anatomical interactions. Despite some limitations, particularly the lack of experimental compression data for σ_{cS}^L calibration, this study provides a strong foundation for future research by emphasizing that credible FE modeling in biomedical applications requires reliable and case-specific material input data. Ensuring rigorous validation from the initial material characterization stage extends numerical accuracy, ensuring reliable predictions in clinical and engineering contexts.

1

INTRODUCTION

1.1. RESEARCH BACKGROUND

The *Aortic Valve Sclerosis* (AVs) is an asymptomatic cardiovascular condition characterized by thickening and/or calcification of the native aortic valve leaflets without significant flow obstruction [1]. While initially asymptomatic, a subset of 1.8% to 1.9% per year of affected patients progress into *Aortic Stenosis* (AS), a more severe condition that substantially reduces valve functionality [1]. The incidence of AVs increases with age, with rates rising from 1.7% to 8.8% per year, reaching up to 17% to 19% in individuals aged 80 to 86 years [1, 2]. Aortic stenosis affects approximately 3% of individuals aged over 75, representing a major clinical challenge due to its significant morbidity and mortality rates [3].

Given the advanced age and high comorbidity burden of most AS patients, conventional open-heart surgical aortic valve replacement (SAVR) is often deemed high-risk or infeasible. As an alternative, *Transcatheter Aortic Valve Implantation* (TAVI) has emerged as a minimally invasive procedure with lower perioperative risks, making it the preferred treatment for elderly and high-risk patients [3]. Initially introduced in 2002, TAVI has undergone significant advancements, evolving from a high-risk-only procedure to a widely adopted intervention across different risk categories [4]. Figure 1.1 illustrates examples of commercially available TAVI devices, highlighting the diversity in design and structure.

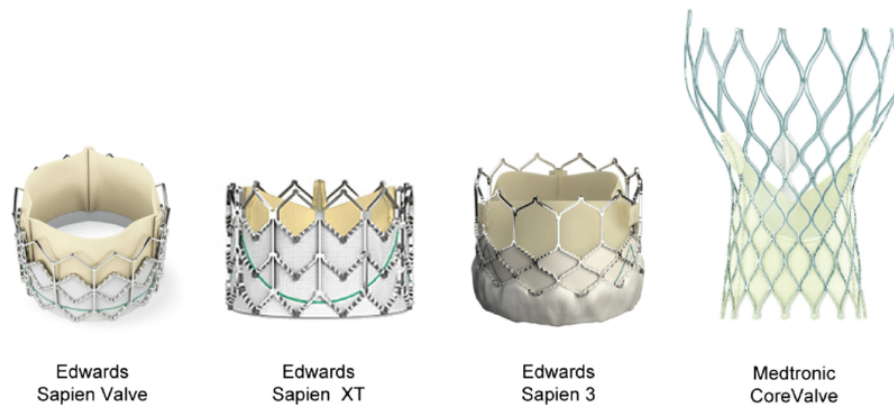


Figure 1.1. Examples of commercially available TAVI valves. The Edwards Sapien series (Edwards Lifesciences) are balloon-expandable valves with a cobalt-chromium frame and bovine pericardial leaflets. The Medtronic CoreValve (Medtronic) is a self-expanding valve with a nitinol frame, designed for enhanced adaptability to the native aortic anatomy. These devices are commonly used for treating severe aortic stenosis, as reported in *Kheradvar et al.* [5].

A critical phase of the TAVI implantation process is the crimping step, where the valve is compressed to reduce its diameter before being loaded onto the catheter-based delivery system. Following deployment, the valve must recover its functional geometry, ensuring proper anchoring and hemodynamic performance. The extreme deformations involved in this process have driven increasing interest in the use of Shape Memory Alloys (SMAs), such as NiTiNol, for TAVI valve manufacturing [6]. NiTiNol is a Nickel-Titanium alloy capable of transitioning between an austenitic and martensitic phase under controlled thermal or mechanical stimuli, enabling superelastic behavior and high recoverable strains. These properties are often modeled using the Auricchio-Taylor framework, which provides a robust theoretical basis for understanding the mechanical behavior of NiTiNol under physiological loading conditions [6, 7].

Advancements in computational modeling techniques have facilitated the use of Finite Element (FE) simulations for analyzing TAVI implantation mechanics and long-term valve performance [4, 8–18]. These models have proven valuable for predicting TAVI behavior, optimizing device design, and assessing patient-specific implantation outcomes. Moreover, regulatory agencies such as the

FDA have recently begun accepting in-silico trials as partial replacements for traditional clinical testing, provided that models adhere to credibility guidelines such as ASME V&V 40 [19–21].

Despite the widespread adoption of FE modeling in TAVI research, a recent systematic review highlighted significant heterogeneity in the modeling approaches used within the scientific community [22]. In particular, NiTiNol superelastic parameters are often poorly reported or inconsistently applied, raising concerns regarding the reproducibility and reliability of FE-based predictions. Ensuring the credibility of FE models for TAVI valves requires not only numerical accuracy but also rigorous verification, validation, and uncertainty quantification (VVUQ), in alignment with emerging regulatory frameworks.

1.2. PROBLEM DEFINITION

The accurate modeling of *shape-memory alloys* (SMAs), particularly *NiTiNol*, is essential for reliable FE simulation of TAVI devices. Although available standard constitutive models for super-elastic materials [7] accurately capture NiTiNol's complex nonlinear behavior driven by stress-induced and thermally-induced phase transformations, their predictive accuracy heavily relies on the availability of precise, experimentally-derived material parameters. While medical device manufacturers typically characterize their NiTiNol alloys using standardized mechanical tests, these proprietary datasets are generally withheld due to confidentiality and intellectual property restrictions. Consequently, the lack of openly accessible, reliable experimental data introduces uncertainty into current research-focused FE modeling practices.

This scarcity of standardized and publicly available datasets forces researchers to depend heavily on generic or literature-derived parameters, often ignoring variability stemming from specific manufacturing processes or alloy formulations. Limited accessibility to manufacturer-characterized datasets significantly constrains the reliability of FE model predictions, particularly under complex physiological conditions. Thus, despite well-established theoretical modeling frameworks, the practical challenge remains obtaining and validating accurate, case-specific NiTiNol properties for credible FE simulations.

The widespread practice of basing modeling assumptions on previous studies without rigorous validation exacerbates these challenges. Inconsistencies in material parameter selection, numerical solver settings, and discretization choices contribute to disparate and sometimes conflicting results across the literature, undermining confidence in FE-based predictions for TAVI valve performance. Moreover, without rigorous *verification, validation, and uncertainty quantification* (VVUQ), simulation outcomes may be influenced by numerical artifacts, rather than providing an accurate representation of the physical behavior of the device.

To accurately evaluate the impact of NiTiNol parameter variability on TAVI FE models, it is essential to develop a fully verified and validated computational framework. This model must adhere to the latest credibility guidelines, such as ASME V&V 40 [20], ensuring that any material-related observations remain independent of external confounding factors. By implementing a rigorous bottom-up validation strategy, this study aims to isolate the role of NiTiNol parameters in governing the mechanical response of the TAVI valve, eliminating unintended influences from numerical errors, solver-dependent behaviors, or non-case-specific assumptions.

The implications of this approach extend beyond simulation accuracy. As in-silico trials gain regulatory acceptance, FE modeling credibility is becoming increasingly important for clinical decision-making, device optimization, and regulatory approval [19, 21]. Ensuring that TAVI FE models are built upon experimentally validated material parameters is critical for enhancing their predictive accuracy, thereby improving their clinical applicability and supporting the broader adoption of TAVI technologies in patient-specific treatments.

1.3. RESEARCH QUESTION AND GOAL OF THE STUDY

This research aims to comprehensively assess the influence of material parameter variability in the FE modeling of TAVI valves, with a specific focus on the complexities presented by shape-memory alloys such as NiTiNol. The nonlinear stress-strain behavior of NiTiNol, characterized by superelasticity and stress-induced phase transformations, as illustrated in Figure 1.2, poses unique challenges for accurate numerical modeling. Given the increasing reliance on FE simulations for in-silico clinical trials, it is crucial to understand how NiTiNol parameter variability affects the predictive accuracy and reliability of TAVI valve modeling.

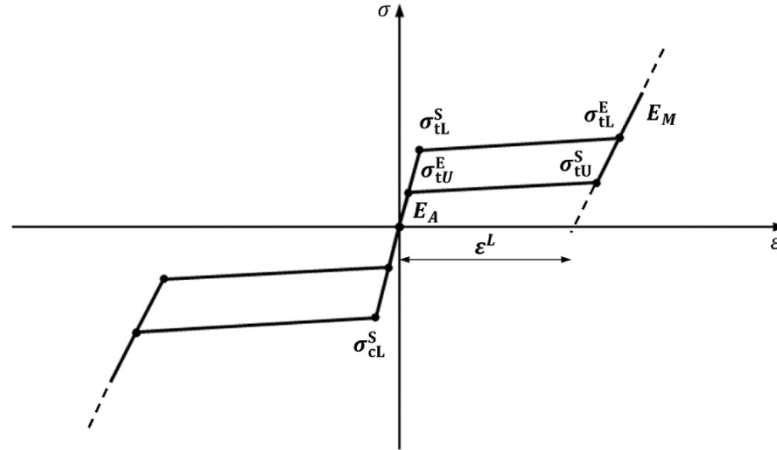


Figure 1.2. Stress-strain response of NiTiNol based on Auricchio's material formulation, illustrating pseudoelastic behavior with phase transformation between austenite and martensite. Adapted from *Carbonaro et al.* [22].

The primary research question guiding this study is:

How can variations in shape-memory alloy parameters within a finite element model influence the predictive accuracy and reliability of TAVI valve technologies under physiological conditions?

To address this question, the study follows a rigorous VVUQ framework, ensuring that findings are independent of numerical artifacts and solver-dependent influences. The methodology will conform to ASME V&V 40 [20] guidelines for computational modeling in biomedical applications, ensuring that the developed FE model adheres to the highest credibility standards.

The research is structured around three pivotal sub-questions, each addressing a key aspect of TAVI valve finite element modeling:

1. *How can verification procedures and validation experiments be designed and applied to ensure the reliability and accuracy of TAVI valve models?* This sub-question focuses on defining experimental protocols that allow for robust validation of the mechanical response of TAVI valves, reducing discrepancies between numerical predictions and real-world performance.
2. *How can the complex behavior of NiTiNol be accurately modeled in FE simulations of TAVI valves, specifically addressing the parameters of Austenite Young's modulus [E_A], Stress start of transformation (loading) [σ_{tL}^S], Stress end of transformation (loading and unloading) [σ_{tL}^E , σ_{tU}^E], and Stress start of transformation (compression) [σ_{cL}^S]?* This sub-question investigates the *sensitivity* of model predictions to variations in NiTiNol phase transformation parameters, ensuring that the material formulation is both accurate and case-specific.

3. *How can physiological load conditions be effectively simulated to test TAVI valve models' structural and functional performance in controlled environments?* This sub-question evaluates how different loading scenarios influence the mechanical response of TAVI valves, determining whether current simulation methodologies adequately represent realistic implantation conditions.

The overarching goal of this study is to enhance the predictive accuracy and robustness of TAVI valve models by integrating high-fidelity material characterization, rigorous verification and validation protocols, and physiologically relevant load conditions. By systematically addressing the proposed sub-questions, this research aims to improve the credibility and clinical applicability of FE modeling techniques for TAVI valves, providing a more reliable foundation for in-silico clinical trials and device optimization.

2

MATERIALS AND METHODS

2.1. EXPERIMENTAL ACTIVITIES

2.1.1. SAMPLE GEOMETRICAL MEASUREMENTS

Sample geometrical measurements are essential for validating computational models and assessing measurement uncertainties. Following ASME V&V 10-40 standards [20], these measurements ensure that *testing conditions, sample variability, and dataset size* are properly quantified to support the model validation process. A model accuracy exceeding 90% is considered sufficient for compliance with the *Context of Use* (COU) of this study.

Specimen population The geometrical parameters of both the TAVI stent and the complete TAVI valve were measured to validate the computational results from the *FE model implementation process* (see Figure 2.4). A total of 10 specimens were analyzed, consisting of 5 TAVI stents and 5 complete TAVI valves. The stent specimens were tested for four parameters, with three independent measurements per parameter, leading to 60 total measurements. The TAVI valve specimens were pretreated via submersion in tap water for 24 hours and tested for one parameter, with three independent measurements per specimen, resulting in 15 additional measurements. In total, 75 measurements were recorded across all specimens.

Experimental setup Measurements were taken using a *digital caliper* (sensitivity $\pm 0.01\text{ mm}$) to capture fine geometrical details of the stent and leaflets. The flare diameter (FD), internal diameter (ID), height (H), and radial thickness (RT) of the stents, along with the leaflet thickness (LT) of the polymeric structure, were recorded. Additionally, a digital thermometer and hygrometer continuously monitored *temperature* (T) and *humidity* (RH%) levels throughout the measurement process to ensure environmental consistency. Figure 2.1 depicts a graphical representation of the 4 stent geometrical parameters over the obtained stent FE model.

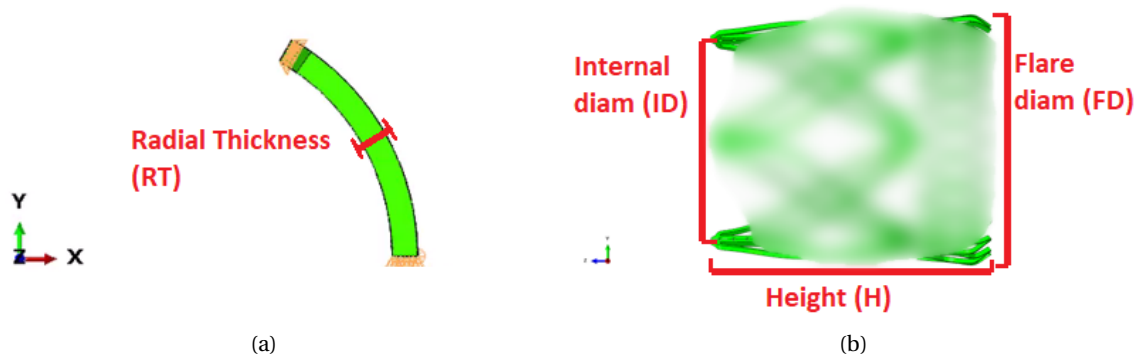


Figure 2.1. Graphical representation of the stent geometrical parameters. Subfigure 2.1a shows the XY plane and a detail of the Radial Thickness RT, while subfigure 2.1b shows the ZY plane and a detail of the flare diameter FD, the internal diameter ID and height H. To preserve intellectual property rights, the stent design has been partially obscured.

Data acquisition and processing The collected data were processed in Microsoft Excel (Microsoft Corporation, Redmond, WA) [23], where *mean values, standard deviations* and *variances* were calculated for each parameter. These statistical evaluations were compared with the nominal values provided by the TAVI manufacturer to assess measurement consistency and potential deviations.

List of components:

- **Precision digital caliper** (Sensitivity = $\pm 0.01\text{ mm}$) for measuring geometrical parameters.
- **Microsoft Excel** [23] for data entry, statistical analysis, and comparison with nominal values.
- **Digital thermometer:** for monitoring and recording temperature during the measurement process.

- **Digital hygrometer:** for monitoring and recording humidity levels during the measurement process.

Experimental procedure:

1. **Instrument Calibration:** Verify and calibrate the digital caliper to ensure measurement accuracy.
2. **Geometrical Measurement:** Measure each geometrical parameter three times per specimen.
3. **Environmental Monitoring:** Record temperature and humidity to maintain consistency across all measurements.
4. **Data Entry and Processing:** Document all measurements in Microsoft Excel and compute mean values, standard deviations, and variances.
5. **Comparison and Validation:** Assess the measured values against the nominal manufacturer specifications to evaluate potential deviations.

Table B.14 presents an overview of the measured geometrical and environmental parameters, together with their statistical analysis.

2.1.2. EXPERIMENTAL VALIDATION OF FRICTION COEFFICIENTS

Accurate determination of *friction coefficients* between critical material pairs is essential for validating the obtained FE models. This study specifically focuses on two key material interactions: NiTiNol alloy against an AlMg3/5754 H111 aluminum plate ($\mu_s^{Al-NiTi}$), relevant for the *crush resistance test* validation simulation, and a 3D-printed polymeric material against the polymeric TAVI valve leaflets (μ_s^{Le-3Dp}), which is critical for the *indentation test* validation simulation. These interactions directly influence the structural response in these simulations, aligning with ISO 5840-3 standards [24].

The friction coefficients were determined using the inclined plane method described by Budinski et al. [25], following ASTM testing standards. This method was selected for its ability to reduce error propagation by eliminating dependencies on specimen weight in the friction measurement, ensuring a more reliable estimation of frictional behavior. Additionally, the slow actuation speeds of the inclined plane approach closely replicate the conditions present in the model validation simulations, minimizing discrepancies between experimental and computational results.

By aligning the friction coefficient measurements with the requirements of the validation simulations, this method ensures that the experimental data provide a credible and applicable foundation for the FE models within the COU of the project.

Experimental setup

The inclined plane method was used to determine the static friction coefficients for two critical material pairs relevant to the

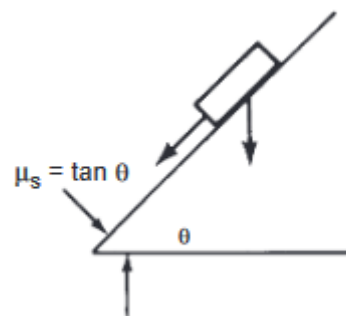


Figure 2.2. Schematic representation of the inclined plane method for measuring the static coefficient of friction μ_s . This method is widely used in frictional studies to characterize material surface interactions. Adapted from Kuhn and Medlin, *Testing Methods for Solid Friction* [25].

finite element model validation simulations, Al- Mg3/5754 H111 aluminum plates against NiTi-Nol stents, ensuring consistency with the crush resistance test validation simulation, and the 3D-printed polymeric surfaces against the polymeric leaflet material, replicating the indentation test validation simulation conditions.

The inclined plane setup consisted of a flat surface made of the selected material, with the specimen placed at an initial position and allowed to move freely once the inclined plane reached a critical angle. The NiTiNol stent specimens were tested in dry conditions, while the complete valves were tested in wet conditions to ensure the leaflet's mechanical response closely matched expected behavior under use.

Data acquisition and processing A digital camera mounted on a tripod recorded each test to minimize parallax errors, capturing the precise moment of specimen movement. The recorded footage was analyzed using Tracker software [26], where the static friction coefficient (μ_s) was calculated using the formula $\mu_s = \tan\theta = \frac{\sin\theta}{\cos\theta} = \frac{a}{b}$ (see Figure 2.2). The extracted coefficients were then entered into Microsoft Excel, where statistical analyses were performed to compute the mean values, standard deviations, and variances for each material pair. Throughout the experiment, temperature and humidity levels were recorded to maintain consistent environmental conditions.

List of components: The following equipment was used for both AlMg3/5754 H111 aluminum-NiTiNol stent friction tests and 3D-printed polymeric-leaflet surface friction tests:

- **Inclined plane surfaces:** AlMg3/5754 H111 aluminum plate for NiTiNol stents tests and 3D-printed polymeric flat surface replicating the indenter probe material for the complete valves tests.
- **Digital Camera with Tripod:** Captured specimen motion while minimizing parallax errors.
- **Millimeter-Scaled Meter:** Placed near the specimen for accurate measurement calibration in Tracker software.
- **Post-Processing Software:** Tracker software for analyzing video data and extracting friction coefficients.
- **Data Analysis Software:** Microsoft Excel for statistical analysis and record-keeping.
- **Thermometer:** Monitored temperature levels.
- **Hygrometer:** Measured relative humidity.

Experimental procedure:

1. **Setup Camera:** Position the digital camera in front of the testing assembly to minimize parallax errors.
2. **Position Specimen:** Place the specimen at the starting point on the inclined plane, ensuring proper alignment for measurement.
3. **Calibrate Measurement:** Place a millimeter-scaled meter near the specimen for accurate measurement calibration in Tracker software.
4. **Record Environmental Variables:** Document temperature and humidity levels to ensure consistency across multiple tests.
5. **Start Recording:** Begin video recording to capture the initial state and movement of the specimen.

6. **Induce Motion:** Gradually increase the inclination angle until the specimen begins to slide.
7. **Stop Recording:** End the video recording once sufficient data has been captured, noting any observations or adjustments.
8. **Data Processing:** Import the recorded footage into Tracker software, extract the friction coefficients, and analyze them in Microsoft Excel for further statistical evaluation.

The obtained friction coefficients for each material pair are summarized in Table 3.2.

2.1.3. MECHANICAL TESTING OF TAVI COMPONENTS

Mechanical tests were conducted to validate the structural response of the TAVI model at different stages of the FE model implementation process. These tests ensured that the model accurately captured the mechanical behavior of the device under testing loading conditions described in the ISO standard [24]. The experimental procedures focused on three primary tests: the *radial compression resistance test*, the *crush resistance test*, and the *indentation test*, each targeting a specific aspect of the TAVI valve's mechanical performance. The *radial compression resistance test* was conducted by a partner company and serves as an independent comparative dataset for validating the applied NiTiNol material model. Therefore, it will not be further detailed except for its role in the model validation process described in Section 3.3.2.2. The *crush resistance test* evaluated the mechanical stability of the fully expanded and shaped stent structure (see Figure 2.8), ensuring that its load-bearing capacity matched experimental results. The *indentation test* assessed the deformation and interactions of the complete valve assembly, focusing on the response of the leaflets to radial loading. To explicitly mitigate experimental uncertainties, such as slight variability in specimen alignment or loading symmetry, a dedicated custom fastening device was designed and employed, ensuring repeatable and accurate measurements, thereby increasing the reliability of experimental validation. These included a 3D-printed *Bridge* part to pin the stent or complete valve in place (see Figure 2.7 and 2.7a), a flat aluminum surface cut via laser and threaded with M6 threading to serve as a stable base, and a *Holder* piece to prevent specimen rotation around the pin, ensuring planar symmetry during testing. This setup, detailed in Appendix A.1 improved the correlation between mechanical lab tests and validation simulations. All test data were post-processed using a custom Python script [27] to ensure consistency in experimental data analysis and facilitate direct comparison with computational results.

Experimental setup Both the *crush resistance test* and the *indentation test* were performed using a *Lloyd Instruments LR 5K compression testing machine* (see Figure 2.3a), designed to apply controlled axial loading, equipped with a 50N load cell. The only difference between these two tests was the actuator mounted to the machine. For the *crush resistance test*, a *flat horizontal aluminum plate* was used to apply uniform axial compression on the stent structure. For the *indentation test*, a *3D-printed indenter probe* (see Figure 2.3b) was used to apply localized radial compression to the valve leaflets. In both cases, specimens were properly aligned in a custom-designed fixture to ensure repeatability and prevent unintended movement during testing. Temperature and humidity levels were continuously monitored to maintain environmental consistency.

Data acquisition and processing Reaction forces (RF, [N]) and displacement data [mm] were continuously recorded throughout the tests. The acquired datasets were stored on a local machine and analyzed using a custom Python post-processing script. This script extracted key mechanical parameters, including reaction force trends, structural stiffnesses, and deformation response, enabling direct comparison with computational model results.

List of components:

- **Lloyd compression testing machine** for applying axial loading.

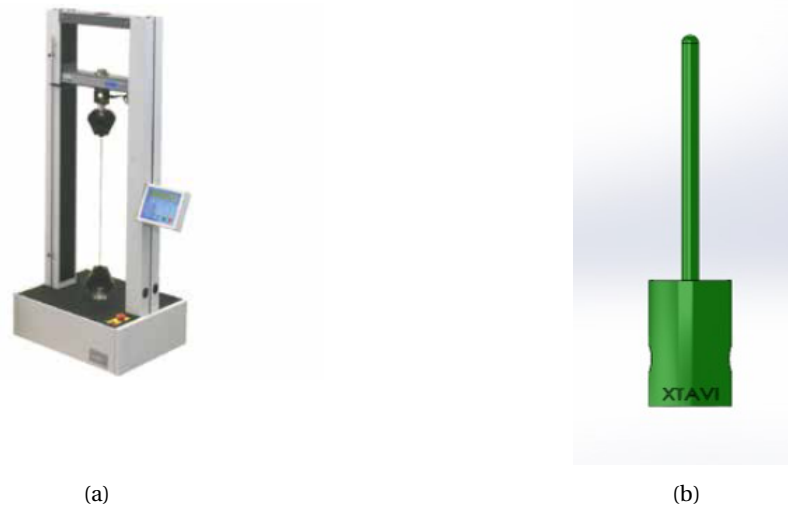


Figure 2.3. Experimental setup for the crush resistance test and indentation test. Subfigure 2.3a shows the Lloyd Instruments LR 5K compression testing machine, while subfigure 2.3b shows the 3D-printed indenter probe.

- **Flat aluminum plate** for uniform compression in the crush resistance test.
- **3D-printed indenter probe** for localized indentation testing.
- **3D-printed Bridge part** for securing specimens during testing.
- **Flat aluminum surface** with M6 threading for stable positioning.
- **Holder piece** to prevent specimen rotation and maintain planar symmetry.
- **Data acquisition system** for recording reaction force and displacement.
- **Thermometer** to monitor environmental temperature.
- **Hygrometer** to track relative humidity.
- **Digital camera with tripod** for additional visual data collection.

Experimental procedure:

1. **Setup and Calibration:** Position the specimen in the fixture, ensuring proper alignment using the Bridge part, aluminum surface, and Holder piece.
2. **Environmental Monitoring:** Record temperature and humidity before testing.
3. **Test Execution:** Apply axial or radial loading at a constant displacement rate, depending on the actuator used, and record reaction force.
4. **Data Collection Conclusion:** Stop the test after reaching the predefined displacement limit.
5. **Post-Processing:** Analyze data using Python scripts to evaluate structural stiffness and compare with simulation results.
6. **Data Analysis:** Compare experimental results with computational model predictions to validate the FE model.

This combined approach and the use of dedicated Python postprocessing scripts ensure methodological consistency between the *crush resistance test* and the *indentation test*, facilitating a unified validation framework for the TAVI valve model.

2.2. FE MODELLING AND COMPUTATIONAL SIMULATION ACTIVITIES

2.2.1. COMPUTATIONAL MODEL(S) SETUP AND CATEGORIZATION

The development of the complete TAVI computational model, a core aspect of this analysis, followed a bottom-up approach within the *FE model implementation process*, incorporating concurrent VVUQ activities to ensure alignment with current standards. This structured approach allowed for the gradual refinement and validation of each model component, ensuring accuracy at every stage of development. Python scripts and Microsoft Excel facilitated data management, ensuring repeatability across multiple simulation runs and parametric explorations while providing a robust framework for handling complex simulations with high precision.

2.2.1.1. SOFTWARE AND TOOLS

Finite element analyses were conducted using Abaqus 2021.HF3 (Dassault Systèmes, Vélizy-Villacoublay, France) [28]. To ensure consistency, all simulations were performed using *.inp* files, offering full control over solver settings and analysis parameters. Python 2.7 was employed in conjunction with Abaqus for scripting, enabling the parameterization of the FE model implementation process and ensuring repeatability in workflow execution. Python scripts managed the automation of simulation setup and post-processing, extracting relevant analysis results and storing them in Microsoft Excel for statistical analysis and validation.

2.2.1.2. FE MODEL IMPLEMENTATION PROCESS

This figure illustrates the structured approach taken to develop the FE model, ensuring accuracy and validation at each stage.

The FE model implementation process followed a structured bottom-up approach, consistent with industry standards in finite element modeling. This methodology allowed for testing and refining the model at incremental complexity levels, minimizing error propagation. The process, illustrated in Figure 2.4, consists of four levels:

- Computer-Aided Engineering (CAE) projects, in orange.
- Model development simulations, in blue.
- Validation simulations, in green.
- Hypothesis exploration, in white.

Each stage of the implementation process was designed to isolate and address specific aspects of the model, limiting the chances of errors being carried over from one phase to the next. A complete overview of the FE model implementation process with relative inputs and outputs is provided in Table 2.1.

Stent Frame (CAE Level) At the CAE level, the stent frame was provided as a flat shell geometry by a partner company. A Python script automated the analysis setup, defining reference systems and executing the extrusion and warping of the flat shell into a cylindrical, solid stent, adjusting the geometries of the shaping surfaces used to give the metallic stent its complex tridimensional shape. The script also defined NiTiNol material properties as outlined in Section 2.2.2, established

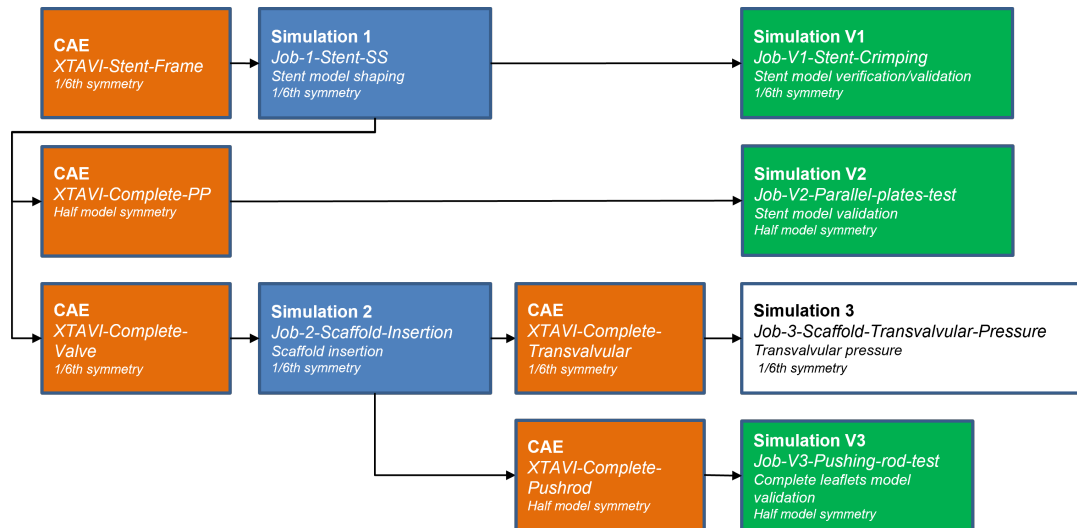


Figure 2.4. Implementation process followed to develop the complete Finite Element model of the TAVI valve, comprehensive of the CAE levels (in orange), the model development simulations (in blue), the validation simulations (in green), and the hypothesis exploration simulations (in white).

necessary contact interactions, and generated analysis parameters for the Stent Shaping simulation, exporting them in a *.inc* file. The initial state and final outcomes of this step are shown in Figure 2.5.

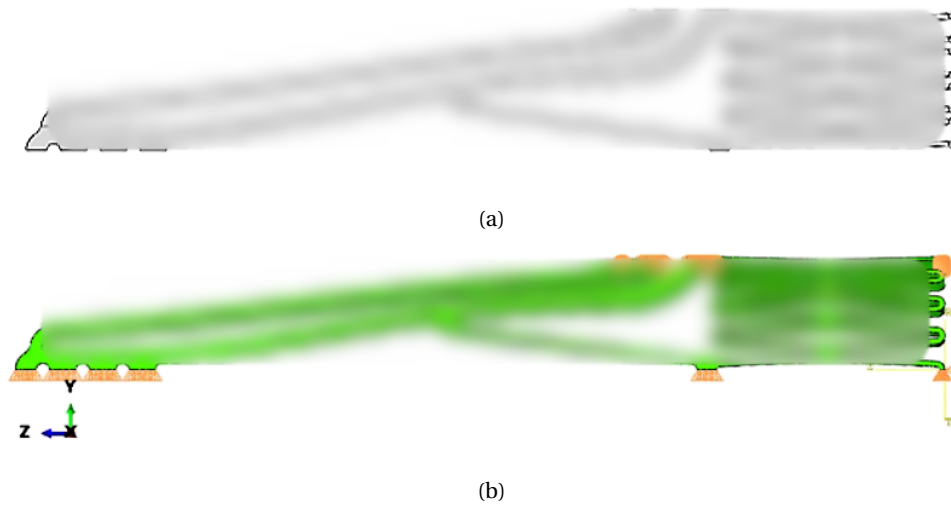


Figure 2.5. Flat geometry and obtained wrapped solid stent frame model. Figure 2.5a shows the flat geometry as provided by the partner company and imported into Abaqus CAE. Figure 2.5b shows the solid stent frame model obtained from the Python preprocessing script, after solid extrusion and cylindrical wrapping, as imported at the beginning of the Stent Shape Setting simulation. To preserve intellectual property rights, the stent design has been partially obscured.

Metallic Stent Shape Setting (Model Definition - Simulation 1) The first forming simulation shaped the metallic stent frame into its final three-dimensional configuration. This step used the *.inp* file generated in the previous step, an analysis definition file specifying the analysis sequence, and a *script-generated .inc* file containing the necessary parameters.

The simulation proceeded through four sequential phases: *radial expansion*, *shaping surface ad-*

justment, scaffold ring sealing shaping, and shaping surface removal. In the radial expansion phase, the *mandrel* (internal shaping surface) expanded the stent to its intended diameter, while the *crimper* (external shaping surface) applied controlled deformation to form the final stent shape. The shaping surfaces were then adjusted to refine the contours of the scaffold ring structure, followed by the gradual removal of shaping surfaces to release the stent from its constrained configuration. To eliminate residual stresses and phase transformations induced by deformation, *dedicated annealing steps* were included at the end of each shaping phase.

The output of this step was an *.odb file* containing the final stent geometry. A dedicated Python script exported selected geometrical parameters for validation against experimental measurements, as described in Section 2.1.1 and reported in Section 3.2.1.1. An XY-plane top view of the obtained solid model is depicted in Figure 2.6.

Radial Stiffness Test (Material Validation - Simulation V1) The first validation simulation aimed to verify the NiTiNol material model parameters, as determined in Section 2.2.2, using an independent dataset provided by a partner company. The analysis was initialized from the configuration obtained in *Step 2*, subjecting the metallic stent structure to radial compression by 80% and 30% of its original diameter using the crimper surface defined in Step 2. The simulation followed a two-phase sequence: *radial compression*, followed by *relaxation* in which the direction of displacement of the crimper is reversed. This simulation step has been developed to match as closely as possible the radial compression resistance test performed on the physical stent by the partner company providing the independent dataset used for validation purposes.

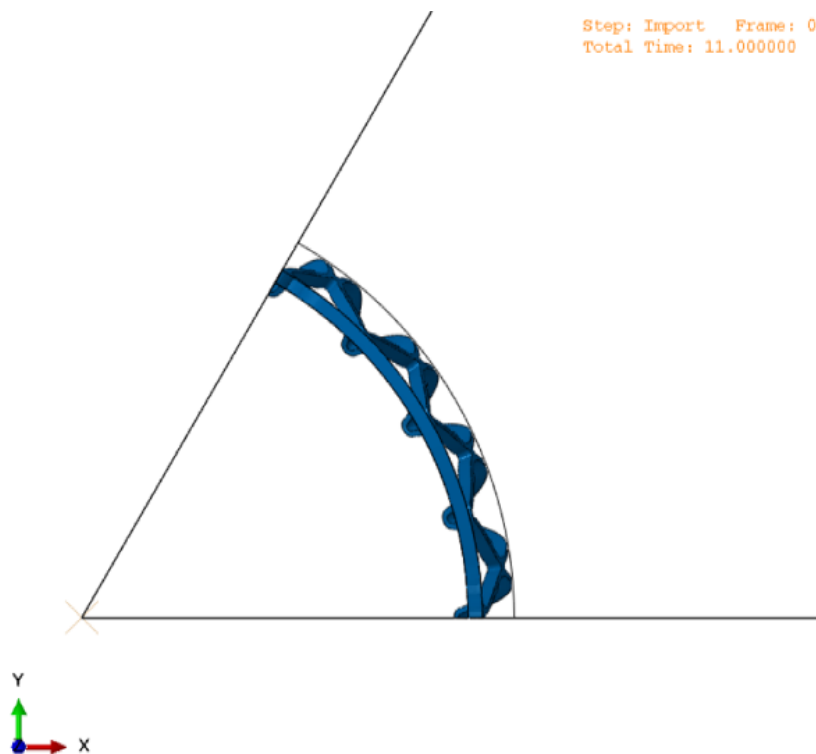


Figure 2.6. XY-plane view of the metallic stent model at the beginning of the radial stiffness test simulation, as obtained at the end of the Stent Shape Setting simulation.

Upon completion, a dedicated Python post-processing script extracted the FD reduction and RF of the crimper from the finite element analysis results. The extracted data were then interpolated to evaluate the *radial stiffness* k_{Radial} of the structure, facilitating a direct comparison with the in-

dependent experimental dataset. To mitigate the influence of structural self-contact, which can introduce numerical artifacts into stiffness evaluation, the script focused on a well-defined diameter range from 24 mm to 23 mm, capturing both compression and relaxation phases.

This selected range is present in both simulation and experimental datasets and encompasses the start of the transformation phase of the NiTiNol material, ensuring consistency in evaluating material behaviour. The specific interpolation methodology applied to the extracted data will be detailed in Section 3.2.2.1, where the simulation results are directly compared to experimental findings. Figure 3.19 presents the obtained force-displacement curve, while Figure 2.6 depicts the stent model as obtained at the end of the Stent Shape Setting simulation.

Half-Symmetry Model (CAE Level) This CAE step automated the creation of a half-symmetry model for the crush resistance test, incorporating *analytical horizontal surfaces* to replicate the aluminum plates of the experimental setup, an *analytical vertical surface* enforcing symmetry constraints, together with the Bridge part introduced in Section 2.1.3 and depicted in Figure 2.7a.

The Bridge part is a 3D-printed polymeric structure developed to secure the valve assembly during experimental tests. Its inclusion in the simulation was critical for accurately replicating the experimental setup, as it directly influenced the geometrical orientation and initial mechanical deformation of the metallic stent. By modeling the Bridge part as a deformable material, the simulation accounted for potential compliance effects while minimizing geometric discrepancies between the computational and experimental setups. This approach ensured that the validation process focused primarily on the stent's material properties and structural behaviour, reducing additional variability from fixture constraints.

The Python preprocessing script handled the automatic import of the stent geometry from Step 2, mirroring it to generate the half-symmetry model while ensuring proper unification of interface mesh nodes. Additionally, the script precisely positioned the Bridge part, adjusted key parameters such as the initial height of the top plate, and implemented the experimentally derived Aluminum - NiTiNol friction coefficient (see Section 2.1.2).

To ensure realistic initial boundary conditions, the script executed a preliminary simulation in which the Bridge part was lowered into contact with the bottom fixed plate, allowing it to pre-deform the stent structure. This step, shown in Figure 2.7b and Figure 2.7c replicated the physical test conditions by mimicking the mechanical settling of the assembly before load application, improving the accuracy of the computational-experimental comparison.

Details of the developed fastening devices used to secure the experimental setup are provided in Appendix A.1.

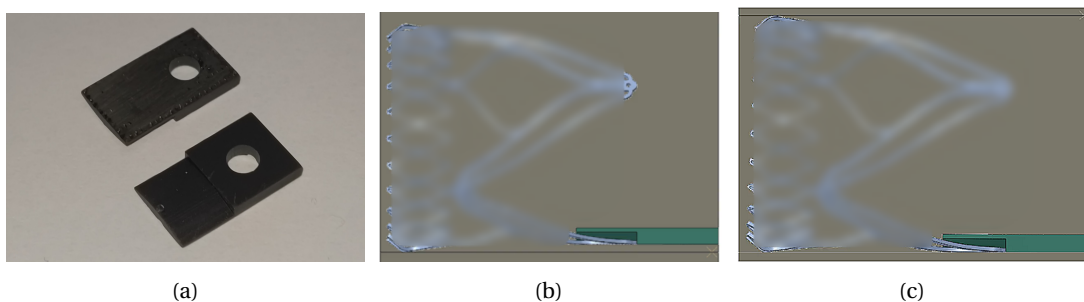


Figure 2.7. Half-symmetry model and physical parts for the crush resistance test. Figure 2.7a shows the 3D-printed Bridge part used to secure the valve assembly during the experimental tests. Figure 2.7b shows the initial configuration of the half-symmetry model, completed of the Bridge part model used for fastening, while Figure 2.7c shows the Bridge and the top plate parts lowered by the Python preprocessing script into their final position for the crush resistance test simulation. To preserve intellectual property rights, the stent design has been partially obscured.

Crush Resistance Test (Stent Geometry Validation - Simulation V2) The goal of this step is to validate the complete stent model in its final geometrical configuration, using the NiTiNol material parameters validated in the Radial Stiffness Test and depicted in Section 3.2.1.2. The test procedure is executed in strict accordance with the experimental protocol presented in Section 2.1.3 to ensure consistency between numerical and experimental testing conditions, and starts from the deformed stent geometry and deformable Bridge part, both obtained through the Python preprocessing script executed at the preceding CAE step.

The simulation follows a two-phase sequence: *compression*, applying controlled axial displacement to replicate mechanical loading conditions, and *relaxation*, allowing for elastic recovery upon reversion of the top analytical surface displacement. At completion, a post-processing Python script extracts relevant data, including FD [mm] and RF [N], from the analysis results. These values are then processed for direct comparison with the experimental dataset, enabling quantitative assessment of the model's accuracy in replicating the mechanical response of the stent, and reported in Section 3.1.3. Figure 2.8 illustrates the initial and final states of the compression step of the crush resistance test simulation.

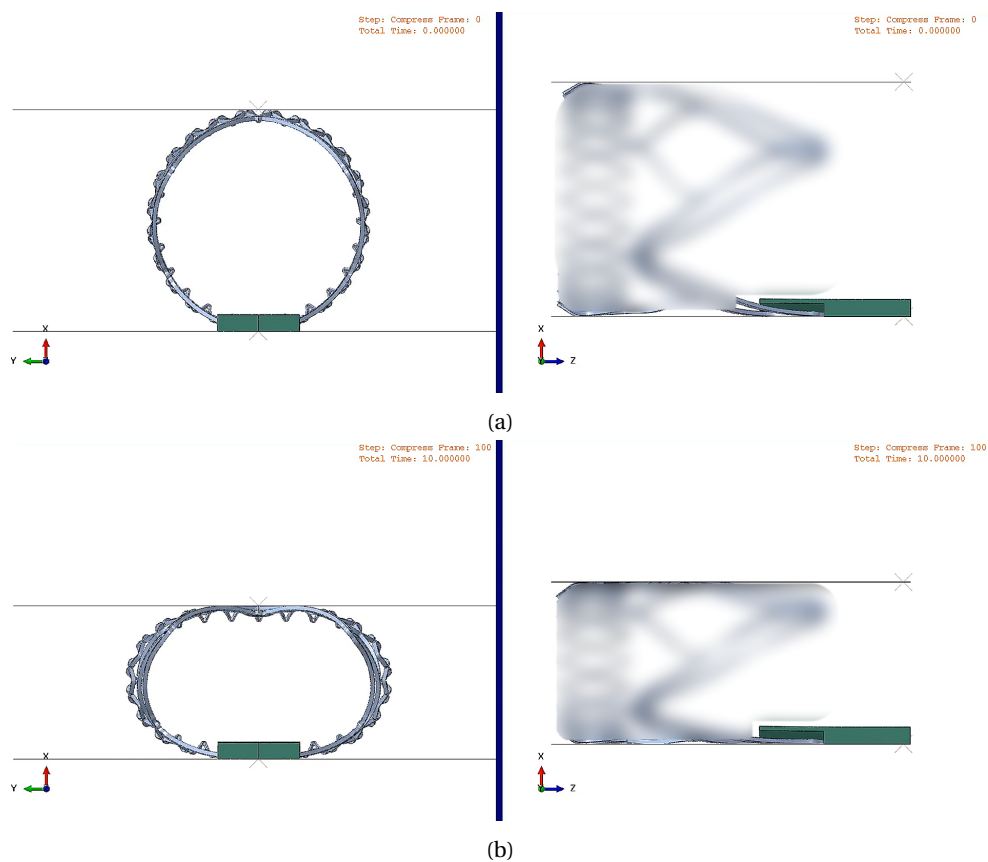


Figure 2.8. Crush resistance test simulation phases. Figure 2.8a shows the initial configuration of the half-symmetry model at the beginning of the crush resistance test simulation, with the Bridge part and top plate already lowered in their starting positions, while Figure 2.8b shows the model at the end of the compression phase. To preserve intellectual property rights, the stent design has been partially obscured.

Complete valve model (CAE level) This CAE step incorporates the shell element leaflets geometry and a smaller crimp surface designed to reduce the diameter of the ring sealing section of the stent, facilitating the insertion of the leaflets model into its final position. The Python preprocess-

ing script reads the results from the stent shape setting analysis and adjusts the geometries of the analysis surfaces accordingly to ensure a seamless transition between simulation steps.

The script also defines the necessary sets, contact properties, and boundary conditions while managing the meshing of the leaflets model to optimize the *discretization error* (DE) analysis. As output, it generates a 1/6th symmetry model that includes both the stent and leaflets components, ensuring that the leaflets are correctly positioned for insertion through a dedicated analysis.

Leaflets insertion (Model definition - Simulation 2) The second forming simulation places the polymeric leaflets in their final position within the TAVI valve assembly. It takes as input the .inp model file generated from the complete valve CAE level and proceeds through four sequential steps: the crimping of the ring sealing section of the metallic stent using a dedicated, smaller *crimper* surface, the guided sliding of the polymeric leaflets into place via specific boundary conditions, the release of the crimper surface, and the viscoelastic relaxation of the leaflets material.

To accurately model the *time-dependent behaviour* of the leaflets, this simulation employs a solver specifically adapted for viscoelastic materials (see Section 2.2.3.2). This ensures that the gradual stress relaxation and creep behaviour inherent to the polymeric material are properly captured, enhancing the accuracy of the final valve configuration, as shown in Figure D.1. Figure 2.9 shows the four sequential steps of the leaflets insertion simulation.

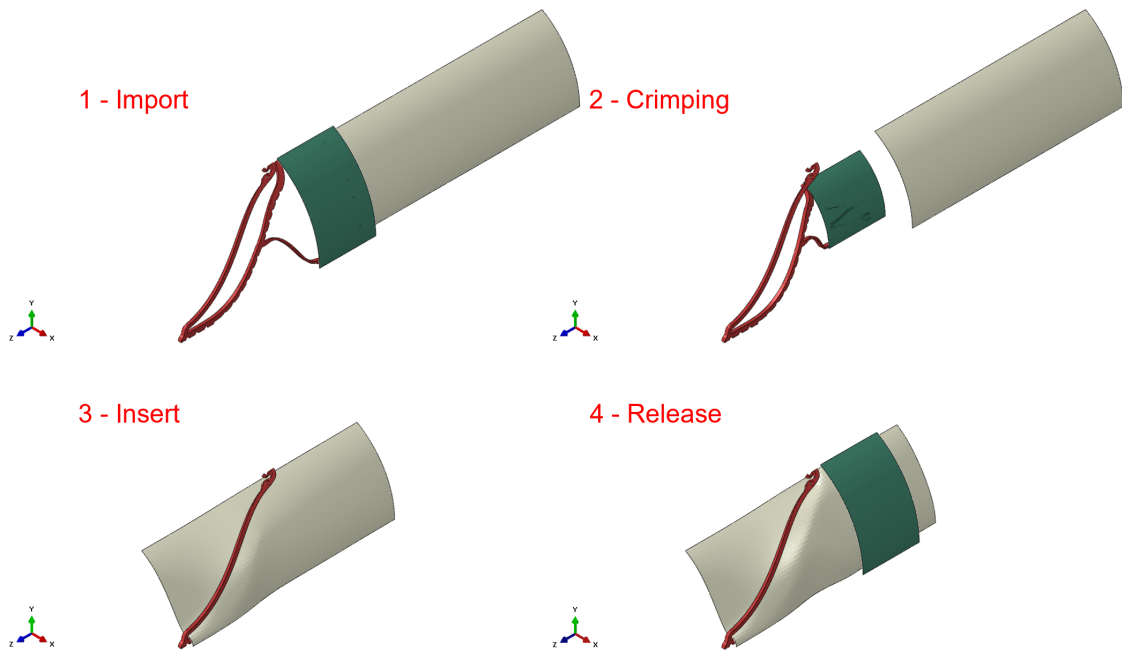


Figure 2.9. Leaflets insertion simulation steps. *Import* represents the model as imported from previous results. *Crimping* shows the crimping of the ring sealing section of the stent. *Insert* depicts the insertion of the leaflets model into the stent structure. *Release* shows the release of the ring sealing section of the stent.

Complete valve transvalvular pressure model (CAE level) This fourth CAE step imports the results from the leaflets insertion simulation and modifies the contact algorithm to implement cohesive behaviour between the stent and leaflets surfaces in contact, as described in Section 2.2.3.2 and shown in Figure D.3. This cohesive interaction simplifies the modeling of the complex yet relatively negligible behaviour at the interface between the leaflets and the suture points present in the real valve.

The implementation of cohesive contact behaviour ensures numerical stability while maintaining the physical adherence of the leaflets to the stent structure. This simplification is supported by previous studies, which have demonstrated that the leaflets model has a minimal impact on the overall FE simulation results [10], making a more detailed interface representation unnecessary for the goal COU of this project.

Cardiac pressure application (Hypothesis exploration - Simulation 3) The transvalvular pressure simulation, the final step of the FE model implementation process, explores the influence of NiTiNol material model parameter variability on the mechanical response of the valve. It compares the parameter ranges obtained within this study with the broader ranges commonly reported in the scientific literature [22].

The simulation applies a physiological aortic valve transvalvular pressure in accordance with the *ISO 5840-1* standard [29] and shown in Figure 2.11 to the internal and external surfaces of the polymeric leaflets model. A preconditioning phase is included to gradually increase the applied pressures to nominal values at the onset of the systolic phase, ensuring numerical stability. The simulation then runs for three complete cardiac cycles to capture the valve behaviour.

A dedicated Python post-processing script extracts the relevant quantities, allowing for the statistical inter-model comparisons described in Section 3.4 and shown in Figure 3.22. These comparisons assess the sensitivity of the valve's mechanical response to variations in NiTiNol material parameters, allowing for a reliable and sensible test of the hypothesis presented in this study. Samples of the Cardiac pressure application simulation results are shown in Figure D.4.

Complete valve indentation test model (CAE level) At this step, a Python preprocessing script imports the results from the leaflets insertion simulation into a CAE model that already contains the indenter probe. This integration allows for further validation of the complete TAVI valve assembly through comparisons with experimental data.

Following the same approach as in the previous CAE step, the script enforces cohesive contact behaviour between the leaflets and the stent, preventing any relative translations between the two components. This ensures that the leaflets remain securely positioned within the stent structure, accurately replicating the experimental setup.

Indentation test (Complete model validation - Simulation V3) This simulation validates the complete assembly model by comparing its mechanical response and deformation behaviour to the experimental dataset obtained from the indentation test described in Section 2.1.3. A 10 mm probe is used to replicate the indentation process applied to the valve leaflets, ensuring consistency with the experimental procedure.

The simulation is divided into two sequential steps. In the first step, the probe is lowered radially onto the leaflets, compressing the structure to evaluate its mechanical response under load. In the second step, the probe is raised, allowing the leaflets to recover. Throughout both steps, the system records data on the leaflets' mechanical response and geometrical configuration, enabling direct comparison with experimental results. An overview of the FE results for the indentation test simulation is provided in Section 3.2.2.3 and shown in Figure D.5.

2.2.1.3. MODEL GEOMETRIES

The development of the final three-dimensional model begins with the flat $\frac{1}{6}$ symmetry CAD geometry provided by the manufacturer. This geometry is imported into Abaqus CAE, where the base 2D external perimeter is extracted, and relevant feature sets are identified for mesh control and discretization error analysis (Figure 2.5a).

Table 2.1. Summary of inputs and outputs for each step of the FE model implementation process, from initial geometry processing to final TAVI assembly.

Inputs	Outputs
Stent Frame CAE Step	
Provided flat geometry User selected parameters Python preprocessing script	Solid model .inp file Analysis parameters
Stent Model Shaping Simulation	
Solid model .inp file Analysis parameters .inc Analysis definition .inp Python postprocessing script	Metallic stent final geometry Geometrical validation parameters
Stent Model Crimping Simulation	
Step 2 from .odb file Analysis definition .inp Python postprocessing script	Stent model reaction forces [N] Stent model FD [mm] Stent model $k_{Radial} [\frac{N}{mm}]$
Half-Symmetry Model CAE Level	
CAE file Solid model from .odb file Python preprocessing script	Deformed bridge assembly .odb
Crush Resistance Test Analysis	
Solid model .inp file Analysis definition .inp Python postprocessing script	Stent model RF [N] Stent model FD [mm] Stent model $k_{Crush} [\frac{N}{mm}]$
Complete Assembly CAE Level	
CAE file Step 2 from .odb file Python preprocessing script	Complete model .inp file
Leaflets Insertion Simulation	
Complete model .inp file Analysis definition .inp	Complete TAVI .odb file
Complete Assembly CAE (Post Leaflet Insertion)	
Complete assembly .odb file Python preprocessing script	Complete TAVI .inp file
Transvalvular Pressure Simulation	
Complete TAVI .inp file Analysis definition .inp	Metallic stent ID [mm] Complete assembly RF [N] Complete model $k_{TransVP} [\frac{N}{mm}]$
Indentation Probe CAE Level	
Complete TAVI .odb file Indentation probe CAE Python preprocessing script	Complete TAVI/Indenter .inp file
Indentation Test Simulation	
Complete TAVI .inp file Analysis definition .inp	Indenter probe translation [mm] Indenter probe RF [N] Complete model $k_{Indent} [\frac{N}{mm}]$

A dedicated Python preprocessing script extrudes the flat geometry into a planar three-dimensional solid model and warps it over a cylindrical reference. This cylindrical solid flat geometry serves as the starting point for the first forming simulation. During the initial phase of this simulation, the flat stent structure is radially expanded using two undeformable analytical surfaces: an internal mandrel and an external crimper. Once the stent reaches the final intended internal radius of 12.5 mm (25 mm ID), the mandrel and crimper surfaces slide along the z-axis by approximately 9

mm, fully uncovering the leaflets sealing ring structure of the expanded metallic stent.

The Table B.13 provides a comprehensive list of relevant geometrical parameters for the metallic stent model and the polymeric scaffold, along with the measurements tolerances. Table 3.1 offers a comparison between the nominal values provided by the manufacturer, and upon which the complete FE modelling phase is based, and the experimental means of the values found in Section 3.1.1.

In the second shaping phase of the stent shaping simulation, two shorter, ring-shaped mandrel and crimper surfaces are positioned over the sealing ring structure, maintaining a clearance of 0.02 mm from the stent surface. These surfaces clamp and bend the stent into the final desired form for the sealing ring. After shaping, the stent is released, and the analytical surfaces are removed, except for the complete crimper surface, which is lowered back by approximately 8.98 mm and remains in place for use in the radial stiffness test simulation for material model validation.

The model is further refined in the leaflets insertion simulation, where a smaller, cylindrical crimper surface radially compresses only the ring structure of the stent, while the stent tip and feeler remain fixed. This targeted deformation creates the necessary clearance between the main stent body and the feeler, allowing the leaflets model to slide into position. The thickness of the polymeric leaflets was not provided by the manufacturer of the valve. Thus, the initial thickness of the leaflets was retrieved from the experimental measurements presented in Section 2.1.1, where a mean thickness of 0.57 mm was recorded.

Following the placement of the leaflets, the crimper surface is released, and the leaflets material undergoes viscoelastic relaxation, completing the computational model of the TAVI valve assembly. Relevant geometrical parameters for the leaflets model are reported in Table B.13. Other structures, such as the indentation probe, the bridge holder, and the testing base surface for fastening, were designed using SolidWorks 2023 [30] and are reported in Appendix A.1.

2.2.1.4. MODEL DISCRETIZATION

Model discretization is the process of subdividing a complex mathematical model representing the reality of interest into smaller, easier-to-compute elements. The stent model was discretized using a grid of three-dimensional, 8-node continuum elements (C3D8). The mesh was generated with a global element size of 0.028125 mm, a deviation factor of 0.01, and a minimum size factor of 0.5. These meshing parameters were determined based on the *Discretization Error (DE)* verification analysis presented in Section 2.3.1, ensuring both result accuracy and solver numerical stability.

The leaflets ring sealing structure, characterized by its symmetrical and repetitive geometry, was seeded with a uniform pattern via part sets created in Step 1 of the FE model implementation process (Figure 2.5a). Given the high bending deformations experienced by this structure during the shape-setting simulation, particular attention was given to its meshing: a minimum of four elements was used in both the radial and angular transversal directions to prevent hour-glassing issues, while the semicircles of the ring sealing structure were seeded with 16 divisions per π rotation.

To account for the slender, beam-like structures of the leaflets ring, a mesh bias factor was applied. Specifically, the transversal plane of the ring structure was assigned a bias factor of 3, while the longitudinal dimension used a bias factor of 4.5, as illustrated in Figure 2.10. The complete set of meshing parameters for both the stent and leaflets models is summarized in Table 2.2 and is consistent with the discretization error analysis

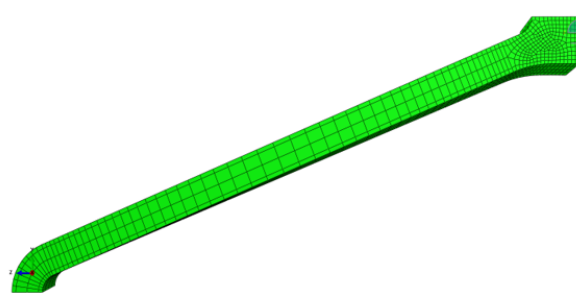


Figure 2.10. Example of a 4.5 bias factor application along the longitudinal direction of the ring sealing structure.

conducted.

Table 2.2. Discretization parameters applied for the meshing process of the stent and the leaflets models, with details on meshing size, element type selection, and key meshing parameters.

Parameter	Stent model	Leaflets model
Element type	C3D8	S4R
Element thickness [mm]	-	0.57
Global mesh seed [mm]	0.028125	0.25
Mesh deviation factor	0.01	0.01
Mesh minimum size factor	0.5	0.01
Uniform seeding circular section ring structure	$\sim 5.09 \frac{\text{node}}{\text{rad}}$	-
Radial amount of elements	4	-
Angular amount of elements	4	-
Angular bias factor	3	-
Longitudinal bias factor	4.5	-

2.2.2. MATERIALS AND INTERACTIONS MODELLING

This section details the material formulations used in the model, specifically NiTiNol alloy, and the interaction properties within the parts that compose the assembly. The NiTiNol material behaviour follows Auricchio's model [7], with parameters obtained through a *Monte Carlo* (MC) sampling statistical fitting within this project, via setting a goal function described by three independent uniaxial tensile stress tests performed by a partner company. Contrarily, the development, verification, and validation of the Abaqus *UMAT* routine used to model the polymeric leaflets were conducted by an external research partner within the research consortium and falls outside the scope of this study. Given its demonstrated minimal influence on the valve's mechanical response [10], and the study's focus on NiTiNol parameter variability, the leaflets material model will not be further detailed.

2.2.2.1. NiTiNOL MATERIAL COEFFICIENTS CALIBRATION

The calibration of the NiTiNol material model was performed through MC simulation-based parameter fitting survey, using an independent strain-controlled uniaxial tensile stress test dataset composed of three probes, each undergoing a loading-unloading cycle twice. The obtained NiTiNol characteristic stress-strain curve is presented in Figure 3.8. This approach allowed for an optimized determination of Auricchio's material model parameters.

To conduct the calibration, a single regular cubic specimen was created in Abaqus CAE and subjected to a strain-controlled uniaxial tensile stress test. The test was implemented by applying a dedicated set of BCs on the YZ-planar surface, while rigid body motion and translations were fully constrained along all three axes. The applied displacement BCs are designed to ensure that the entire phase transformation of the NiTiNol alloy along the strain axis was captured, closely mimicking the performed experimental test and enabling accurate parameter fitting.

The material parameters calibrated through this process include austenitic phase Young modulus E_A , the martensitic phase Young's modulus E_M , transformation strain value ϵ_L , start and end transformation stresses during loading σ_{tL}^S , σ_{tL}^E , and start and end transformation stresses during unloading σ_{tU}^S , σ_{tU}^E . Although different from the set of parameters highlighted in *Carbonaro et al.*[22], the absence of a uniaxial compressive test prevented the correct parameterization of the start transformation stresses in loading compression σ_{cL}^S . For this reason, this parameter has been excluded from the Monte Carlo simulation, and its estimation relies on the average of the parameter range commonly found in literature.

The results of the Monte Carlo simulation are presented in Section 3.2.1.2, where the calibrated material parameters are compared to the starting, nominal values. The calibration process targeted a maximum NRMSE of 10%, ensuring alignment with the desired final accuracy of the model. The calibrated material parameters are then used in the radial compression resistance test simulation to validate the material model, as described in Section 2.2.1.2 and Section 3.3.2.2.

2.2.2.2. INTERACTION MODELLING

To ensure an accurate representation of contact interactions within the computational model, intra- and inter-model interactions are explicitly defined within the .inp files. The leading surface in each contact pair is assigned to the coarser mesh and the stiffer material to enhance numerical stability.

Contact interactions are primarily modeled as *general*, *hard contact* with only normal behaviour considered, except in validation simulations V2 and V3, where additional tangential behaviour is included. The contact stiffness coefficient $E_{Contact}$ is derived from the material stiffness, improving numerical stability while ensuring computational efficiency without compromising physical accuracy.

Following the completion of the leaflets insertion simulation, cohesive contact behaviour is applied between the external stent surface and the internal leaflets surface. This interaction model simulates the fastening mechanism that secures the polymeric leaflets to the stent structure, preventing relative motion between the two components, and the results of its implementation are available in Figure D.3. Table 2.3 summarizes the implemented contact formulations, stiffness values, and friction coefficients for each simulation step.

Table 2.3. Summary of interaction modelling parameters applied throughout the FE model implementation process, with details on the specific contact pairs involved and the Simulations in which they are implemented.

Interaction	Formulation	$E_{Contact}$	μ_s	Simulations
NiTi - Shaping surfaces	Edge-to-Surface	$0.1E_A^{NiTi}$	-	1, V1, 2
NiTi - NiTi	Edge-to-Edge	$0.01E_A^{NiTi}$	-	V1
NiTi - Polymer	Edge-to-Edge	$0.1E_A^{Lflt}$	-	2, 3, V3
NiTi - Al	Edge-to-Surface	$0.1E_A^{NiTi}$	0.277	V2
Leaflets - Indenter	Edge-to-Surface	$0.1E_A^{Lflt}$	0.581	V3

2.2.3. SIMULATION CONDITIONS AND PARAMETERS

To ensure numerical stability and physical consistency throughout the FE model implementation process, all simulations adhere to controlled boundary conditions, solver parameters, and applied loads designed to replicate realistic mechanical interactions. The majority of simulations are strain-controlled, with displacements applied to relevant geometric entities to evaluate the structural response. Boundary conditions enforce appropriate constraints for symmetry, preventing rigid body motion while allowing for the natural deformation of the components. Contact interactions between different model parts are rigorously defined to capture mechanical behavior accurately. Numerical solver parameters are carefully selected to balance computational efficiency and solution accuracy, ensuring stable convergence, and tested in Section 2.3.1 in accordance with the ASME guidelines [20]. External loading conditions are limited to the transvalvular pressure simulation, where a physiologically accurate pressure waveform is imposed on the valve structure to simulate cardiac function. The following sections detail the applied boundary conditions, contact interactions, solver settings, and loading parameters governing the computational model.

2.2.3.1. BOUNDARY CONDITIONS

With the exception of the transvalvular pressure simulation, where a dynamic load is applied, all simulations in the FE model implementation process are strain-controlled. In these cases, BCs dictate the total displacement of relevant geometric or mesh sets, allowing for the evaluation of stresses and mechanical strains. All BCs are defined in a cylindrical reference system, with the exception of Simulation V2 and V3, and in order to enforce symmetry, solid models and shaping surfaces are constrained along the theta-axis, as shown in Figure 2.5b.

Stent shaping simulation (Simulation 1) The undeformable crimper and mandrel surfaces are radially expanded to achieve the stent's intended final diameter. Once expanded, these surfaces are translated along the z-axis to expose the leaflets ring sealing section of the expanded cylindrical stent. The smaller, curved crimper and mandrel surfaces then clamp onto the stent, shaping it into its final three-dimensional form. In the final releasing step, only the crimper is translated back in place, preserving it for the next validation simulation. The required radial translation of the shaping surfaces is evaluated via a Python script at the first CAE level and stored as an additional .inc file.

Radial compression resistance test simulation (Simulation V1) The crimper surface radius is first reduced by 30% or 80% of its original value before being released, allowing for elastic rebound. Translation along the theta-axis is restricted, while the stent height is left unconstrained, except for the lowest section of the model, which is fixed over the z-axis to prevent rigid body motion. This arrangement allows the stent model to deform along the z-axis, as expected, during compression and release phases.

Crush resistance test simulation (Simulation V2) The stent is constrained only along the theta-axis to maintain symmetry. A speed BC is applied to the top plate analytical surface, directed along the x-axis in a rectangular reference system, mimicking the experimental protocol. Additionally, the section of the bridge not in contact with the TAVI model is constrained along the x, y, and z axes in a rectangular reference system.

Leaflets insertion simulation (Simulation 2) The small crimper surface is radially displaced by 50% of the original ID, while the feeler and top tip of the stent are fully constrained along the r, theta, and z axes. The leaflets model is then slid into place via displacement BCs along the z-axis, and the small crimper is released, allowing for elastic rebound of the metallic structure, followed by time-dependent creep due to the leaflets' viscoelasticity. To allow for radial relaxation, particularly in the leaflets ring sealing structure, constraints along the r and z axes are applied only to the uppermost sections of the model. Lateral edges of the models are constrained along the theta-axis to enforce radial symmetry. A graphical evaluation of the difference in FD between the leaflets insertion simulation and the initial stent shape setting simulation is presented in Figure D.1.

Transvalvular pressure simulation (Simulation 3) The complete assembly is secured by constraining the leaflets ring sealing section of the complete TAVI valve model along the r, theta, and z axes, preventing rigid body motion during the application of the physiological pressure load. This arrangement of BCs allows the top tip of the TAVI valve assembly to radially bend under valve operational conditions, while the implemented cohesive contact behaviour ensure contact continuity between the unconstrained sections of the assembled stent and leaflets models.

Indentation test simulation (Simulation V3) A displacement BC applied to a reference point forces the indenter probe along the r-axis, replicating the experimental protocol. The same BCs constraining the complete leaflets ring sealing structure in the transvalvular pressure simulation constrain

the model from translations while allowing the top tip of the structure to bend and tilt accordingly to applied loads. The Bridge part, although present in the actual experimental setup, was intentionally excluded from the numerical simulation, meaning its mechanical stabilizing effect is absent in the FE model. Consequently, a larger deviation between numerical predictions and experimental observations is anticipated due to this simplification.

Table 2.4. Summary of BCs applied across simulations, detailing constraints and displacements for stent shaping, mechanical tests, and leaflet insertion and interactions, together with the final application simulation.

Boundary Conditions Summary		
Simulation	BC Module	Application
Stent shaping (Sim. 1)	~+7.97 mm	Crimper/mandrel
	~+8.98 mm	All shaping surfaces
	±1.025 mm	Shaping crimper/mandrel surfaces, crimper
	~-8.98 mm	Crimper surface
	~-48.98 mm	Mandrel, shaping surfaces
Radial stiffness test (Sim. V1)	-3.75 (-10) mm	Crimper
	+3.75 (+10) mm	Crimper
Crush resistance test (Sim. V2)	-0.83 mm/s	Top plate
	+0.83 mm/s	Top plate
Leaflets insertion (Sim. 2)	-6.75 mm	Small crimper
	+29.7 mm	Leaflets
	+6.75 mm	Small crimper
Transvalvular pressure test (Sim. 3)	Constrained	Leaflets ring sealing structure
Indentation test (Sim. V3)	-0.83 mm/s	Indenter probe
	+0.83 mm/s	Indenter probe

2.2.3.2. COMPUTATIONAL SOLVER PARAMETERS

The numerical solver parameters used in this study are critical in ensuring the *stability, accuracy, and reliability* of the computational model. While these parameters do not directly correspond to physical quantities, they significantly impact the *convergence behavior, numerical robustness, and overall computational efficiency* of the finite element simulations.

All simulations were performed using a *general non-linear static stress analysis*, with the exception of the *relaxation phase of the leaflets insertion simulation*, which was modeled as a *general non-linear quasi-static stress analysis*. This distinction accounts for the time-dependent viscoelastic behavior of the leaflets material.

To enhance *numerical stability*, an automatic stabilization algorithm is applied, setting the *maximum dissipated energy fraction* to 2×10^{-4} . This stabilization is dynamically regulated by the ALLSDTOL parameter, set to the default value of 0.05, as recommended by the Abaqus documentation. These standard Abaqus-suggested values provide a suitable starting point for simulations, typically achieving sufficient artificial damping without compromising result accuracy or significantly influencing the energy balance.

Additionally, *contact stiffness coefficients*, discussed in Section 2.2.2, play a crucial role in ensuring accurate force transmission between contacting surfaces. These parameters are carefully calibrated to balance *numerical stability and computational efficiency*, preventing artificial penetrations or excessive stiffness that could lead to solver instabilities. The full list of solver parameters implemented in this study and included in the Verification process is summarized in Table 2.5.

2.2.3.3. LOADING CONDITIONS

Across the FE model implementation process, no external static or dynamic loads are applied, except in the *transvalvular pressure simulation*. In this case, a distributed load (DLOAD) of variable amplitude is imposed on both the internal and external surfaces of the leaflets model to replicate physiological loading conditions.

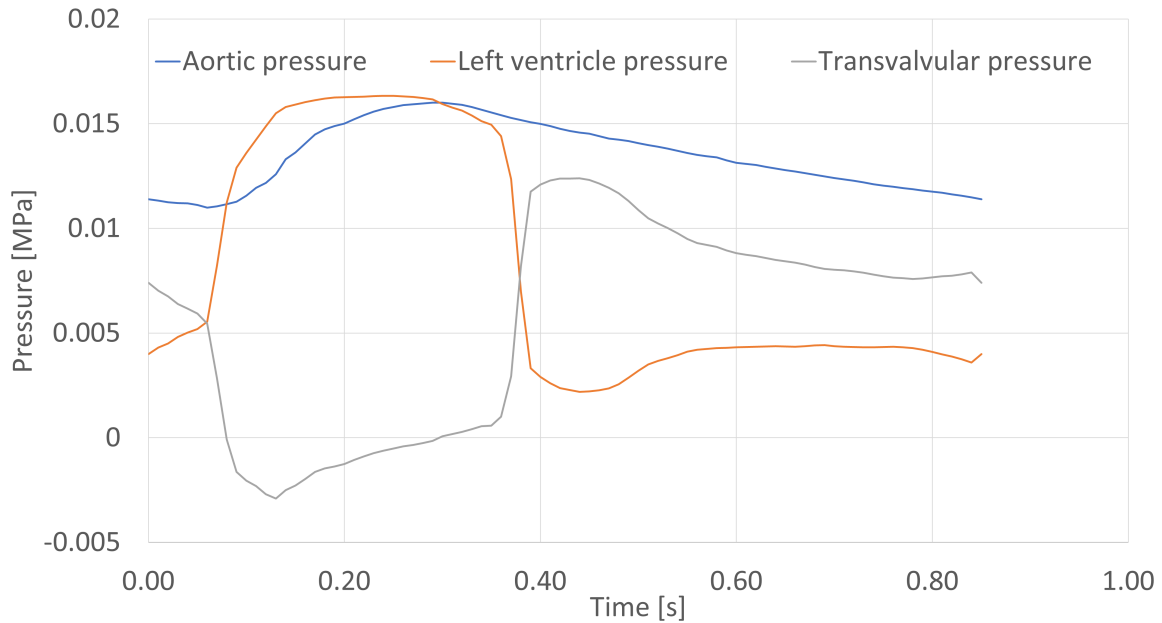


Figure 2.11. Pressure curves applied to the internal and external surfaces of the leaflet model in the transvalvular pressure simulation, showing aortic and left ventricular pressures along with the resulting transvalvular pressure difference.

On the internal surface of the leaflets model, a pressure waveform characteristic of the left ventricular pressure is applied, while a corresponding aortic pressure waveform is imposed on the external surface. These pressure curves, obtained from the ISO 5840-1 standard [29], are normalized for standard physiological conditions. The applied loading conditions assume a cardiac output of 5.0 L/min, a heart rate of 70 bpm, a stroke volume of 71.4 mL, and a peak systolic aortic pressure of 120 mmHg (~ 0.16 MPa), representing normative blood pressure conditions in the left heart of an average adult human male. The time-dependent variations of these applied pressure conditions are illustrated in Figure 2.11, while a summary of the applied loading conditions is provided in Table B.12.

2.3. VERIFICATION, VALIDATION AND UNCERTAINTY QUANTIFICATION ACTIVITIES

2.3.1. MODEL VERIFICATION PROCESSES

The verification of a computational model ensures the correct implementation of modeling techniques and the solver's ability to accurately resolve the mathematical representation of the system, independent of its correlation with the physical system. The ASME V&V 40-2018 [20] identifies two primary branches of verification: *code verification* and *calculation verification*. While no code verification activities were performed in this project, calculation verification was considered essential to ensure the correct implementation of the mathematical model.

To conduct verification activities efficiently, a smaller, computationally lighter section of the stent

model was selected as representative of the full 1/6th symmetry model. This section, corresponding to the 1/4th ring quarter-cell model, is shown in Figure 2.10. Its selection was guided by initial modeling observations and computational challenges, offering multiple benefits. This region experiences the highest deformations during stent shaping and leaflets insertion simulations, making it the most critical for result accuracy while also being part of a repeating, geometrically identical pattern. This selection allowed for a reduced computational cost without compromising the representativeness of the overall stent model.

For independent verification of the leaflets model, a half-symmetry, leaflets-only model was created using a modified version of the Python script developed for the complete valve CAE level (Figure 2.12, depicting the discretized leaflet geometry). Unlike the insertion model used in the FE model implementation process, this version does not import results from previous simulations. Instead, it revolves the leaflets geometry over a π angle, rather than the standard $\frac{\pi}{3}$, and integrates the pushrod indenter probe to conduct an indentation test.

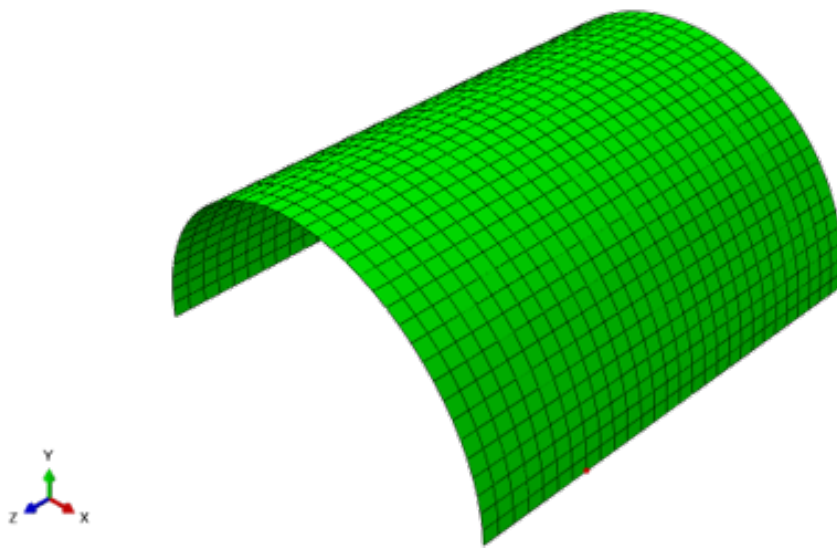


Figure 2.12. Half-symmetry leaflets FE model used for DE analysis. The model geometry represents half of the leaflet structure, meshed with shell elements, and is employed to independently evaluate the numerical accuracy and computational stability of the indentation test simulation.

A complete *spatial discretization error analysis* was performed through mesh convergence studies for both the leaflets and stent models, while a *numerical solver error analysis* was performed on key solver parameters to assess their impact on computational stability and accuracy. Although not independently tested, the *use error* was minimized through the implementation of automated Python scripts across the FE model implementation process, reducing reliance on manual input and ensuring repeatability, consistency, and error mitigation across multiple model iterations.

2.3.1.1. NUMERICAL SOLVER ERROR (NSE)

The NSE refers to errors in the solution that arise from the specific selection of solver parameters. According to ASME V&V 40 [20], the highest level of NSE verification consists of a problem-specific sensitivity study, demonstrating that the results remain independent of the chosen solver settings.

To achieve this, five key parameters were evaluated across a wide range of values, covering different aspects of the numerical solution process. Three of these parameters pertain to Abaqus step settings, influencing the solver's initial conditions and progression through the simulation, while

the remaining two focus on interaction algorithms, governing how contact between model components is detected and enforced. The complete list of tested parameters and their respective ranges is presented in Table 2.5.

To quantify the NSE, the radial stiffness of the model was evaluated across the tested parameter ranges and compared against the nominal case. The NRMSE was calculated between the nominal case and the extreme values of the selected testing ranges, providing a clear measure of the solver parameter influence on the model's numerical stability and accuracy (see Section 3.3.1 for detailed results).

Table 2.5. Numerical Solver Error (NSE) parameter selection and relative variability ranges investigated as part of the verification process. The table is divided in two parts: the top section shows the parameters involved in the solver setup, while the bottom section shows an overview of the applied contact parameters.

Parameter	Nominal value	Range	Model
Dissipated energy fraction	2×10^{-4}	$0.0 - 2 \times 10^{-3}$	1/4th ring quarter-cell model
ALLSDTOL	0.05	0.0 - 0.10	1/4th ring quarter-cell model
Dynamic step application	Quasi-static	Moderate dissipation	Indentation test
NiTi contact stiffness	$0.1E_A^{NiTi}$	$(0.01 - 1)E_A^{NiTi}$	1/4th ring quarter-cell model
Polymer contact stiffness	$0.1E^{Flt}$	$(0.01 - 1)E^{Flt}$	Indentation test

2.3.1.2. DISCRETIZATION ERROR (DE)

The discretization error was estimated through geometrical and mathematical parameterization fields, assessing the progressive refinement of the mesh and the influence of element type selection on the final results.

The stent model DE analysis consists of multiple tests, each addressing a specific aspect of mesh quality and its impact on computational accuracy and efficiency. The leaflets model underwent a separate discretization error assessment due to its different material properties and geometric complexity.

A full overview of the tested element types, mesh refinement levels, and evaluation criteria is provided in Section 3.3.1, where the results of the discretization error analysis are presented.

2.3.2. MODEL VALIDATION STRATEGIES

Model validation assesses the model's ability to accurately represent the physical system under analysis, ensuring that its results are comparable to experimental measurements. Validation is typically performed by comparing the mathematical model outputs with experimental data, verifying that the computational framework reliably replicates the mechanical response of the system [20].

Aside from the Validation Simulations (V1, V2, and V3) introduced in Section 2.2.1, which validate the model's mechanical response under different experimental conditions, the model inputs have also been validated through direct measurements and statistical evaluation of key geometrical parameters, presented in Section 2.1.1. Uncertainty quantification was performed on key geometrical inputs. However, the propagation of these uncertainties was deemed negligible for the scope of this study, as the focus is on the sensitivity of the model to the NiTiNol material parameters presented in Section 1.3. Consequently, all simulations employ nominal values for model inputs, with the sole

exemption of the NiTiNol material model parameters, ensuring a controlled evaluation of material parameter influence on model behaviour.

2.3.3. HYPOTHESIS EXPLORATION ANALYSIS

The hypothesis exploration analysis evaluates how the mechanical response of the complete TAVI model depends on the accuracy of NiTiNol material properties, as well as their verification and validation. Two distinct parameter ranges were considered: the first, derived from the Monte Carlo statistical parameter fitting in Section 2.2.2, defines its upper and lower bounds by symmetrically adjusting the fitted parameters around their nominal values. The second range encompasses the broader material property variations commonly reported in the literature [22].

To quantify the impact of these variations, a total of 21 transvalvular pressure simulations (Step 9) were performed, comprising one nominal case, ten simulations exploring the Monte Carlo-derived parameter range, and ten additional simulations covering the literature-reported parameter variations. A Python post-processing script extracted the simulation results, computing the total radial stiffness of the model, reaction forces, and leaflet radial coordinates at the tip, with comparisons performed against the nominal case via NRMSE calculations.

A complete breakdown of the tested parameters and their influence is provided in Section 3.4, where the results of the hypothesis exploration analysis and sensitivity analysis are presented.

3

FRAMEWORK RESULTS

3.1. EXPERIMENTAL ACTIVITIES RESULTS

3.1.1. SAMPLES GEOMETRICAL MEASUREMENTS

3.1.1.1. STENT GEOMETRICAL MEASUREMENTS

A total of three independent measurement sets in dry conditions were conducted on five TAVI stents, evaluating key geometrical variables: *flare diameter* (FD), *internal diameter* (ID), *specimen height* (H), and *stent radial thickness* (RT). Environmental conditions, including *temperature* (T) and *relative humidity* (RH%), were recorded to ensure consistency across measurements.

The results were statistically processed in Microsoft Excel [23]. Table 3.1 provides the summarized mean values of the measurements, while a full dataset, including individual measurements, standard deviations, and intra-sample variability, is provided in Appendix B (Table B.14).

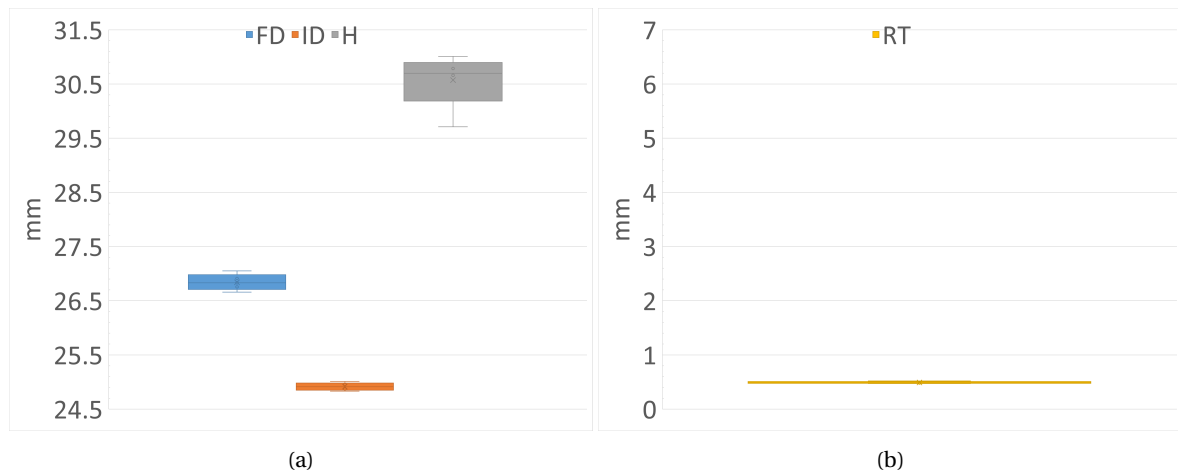


Figure 3.1. Box-and-whisker plots of key stent geometrical variables: final diameter (FD), initial diameter (ID), height (H) in 3.1a, and radial thickness (RT) in 3.1b. The plots show median values, interquartile ranges, and whiskers extending to the minimum and maximum measured values.

3.1.1.2. LEAFLETS GEOMETRICAL MEASUREMENTS

The *leaflet thickness* (LT) was measured on five wet specimens of complete TAVI valves to evaluate dimensional consistency. Environmental conditions, including *temperature* (T) and *relative humidity* (RH%), were recorded to ensure controlled testing conditions.

The results were statistically analyzed in Microsoft Excel [23]. Table 3.1 provides a summary of the mean thickness values across all measured specimens. Full detailed measurements, including intra-sample variability and individual values, are provided in Appendix B (Table B.15).

Table 3.1. Nominal and mean values of key geometrical parameters obtained from experimental measurements of five stent specimens and five complete TAVI specimens, along with their standard deviations.

Parameter	Nominal value [mm]	Mean exp value [mm]	ST.D.
Flare Diameter (FD)	27.5	26.84	0.11
Internal Diameter (ID)	25.0	24.91	0.05
Height (H)	31.1	30.67	0.29
Radial Thickness (RT)	0.45	0.49	0.01
Leaflet Thickness (LT)	-	0.57	0.02

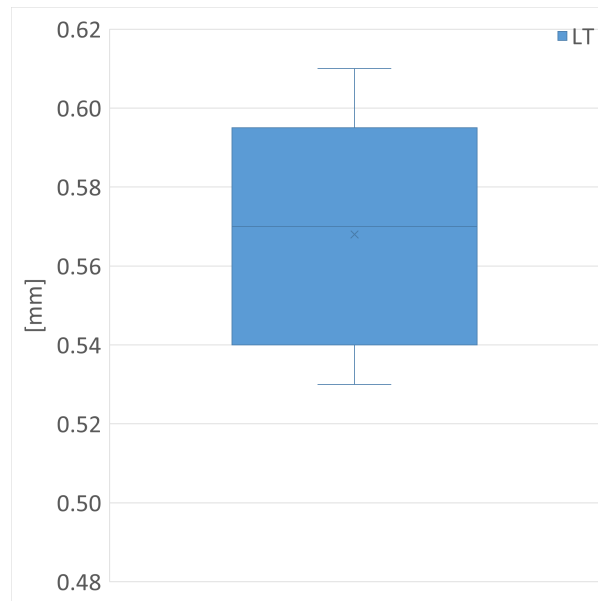


Figure 3.2. Box-and-whisker plot of leaflet thickness (LT) measurements from five complete TAVI specimens, showing the mean, interquartile range, and whiskers extending to the minimum and maximum values.

3.1.2. EXPERIMENTAL VALIDATION OF FRICTION COEFFICIENTS

3.1.2.1. ALUMINIUM - NiTiNOL (AL-NiTiNOL) FRICTION COEFFICIENT

The *static friction coefficient* $\mu_s^{Al-NiTi}$ for the Aluminium - NiTiNol pair was experimentally determined using an *inclined plane test*, ensuring controlled and repeatable conditions. The tests were conducted under recorded temperature and relative humidity to account for environmental influences.

The results were extracted via video post-processing, analyzed in Tracker software [26], and further processed in Microsoft Excel for statistical evaluation [23]. However, some sample recordings (S1-2, S5-1, and S5-2) were excluded from the analysis due to poor video resolution and inadequate frame sampling, making precise evaluation infeasible.

Table 3.2 summarizes the mean friction coefficient $\mu_s^{Al-NiTi}$ found and its variability, while a complete list of individual test results can be found in Appendix B (Table B.16).

3.1.2.2. LEAFLETS - INDENTER FRICTION COEFFICIENT

The friction coefficient $\mu_s^{Llt-Prb}$ for the leaflet/indenter polymer pair was experimentally determined using an *inclined plane test*, with a single test run recorded for each of the five wet specimens. Environmental conditions, including temperature (T) and relative humidity (RH%), were monitored to ensure consistency across measurements.

The results were extracted via video post-processing, analyzed in Tracker software [26], and statistically processed in Microsoft Excel [23].

Table 3.2 summarizes the mean friction coefficients and standard deviations, while a complete dataset of individual test results can be found in Appendix B (Table B.17).

3.1.3. MECHANICAL TESTING OF TAVI COMPONENTS

3.1.3.1. RADIAL STIFFNESS TEST

The *radial stiffness test* was conducted by an external company on a single metallic stent specimen, evaluating the structural response under 30% and 80% diameter reduction conditions. The overall

Table 3.2. Experimentally measured friction coefficients and their standard deviations for two material pairs: Aluminium-NiTiNol and Leaflet-Indenter. These values characterize the static friction interactions relevant to the mechanical behavior of the tested components.

Parameter	Value [/]	SD
$\mu_s^{Al-NiTi}$	0.277	0.066
$\mu_s^{Llt-Prb}$	0.581	0.068

3

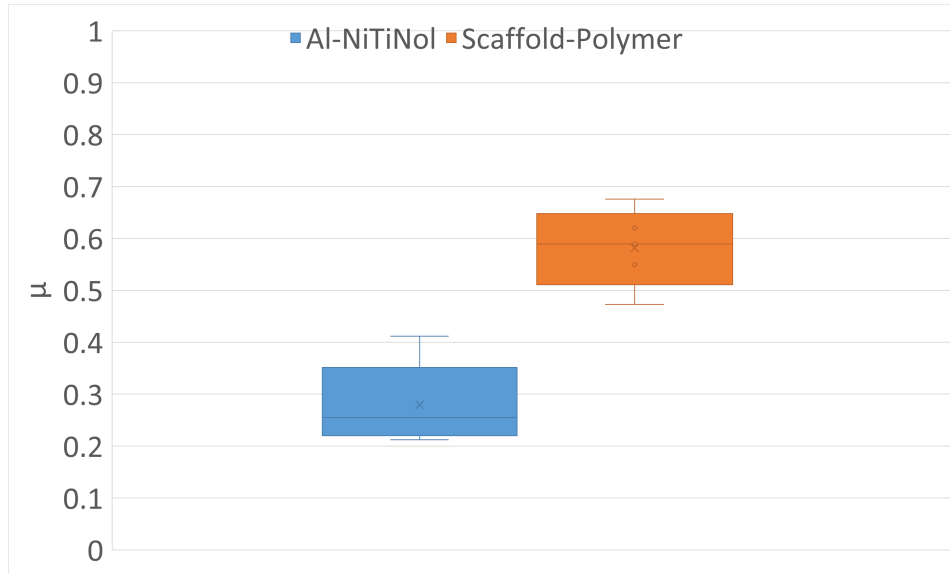


Figure 3.3. Box-and-whisker plot of the measured friction coefficients for both Al-NiTiNol and Scaffold-Polymer friction tests, illustrating the variability and spread of the experimental results across different test samples. The plot includes mean values, interquartile ranges, and whiskers extending to the minimum and maximum values of the evaluated friction coefficients.

reaction force vs. diameter curve is presented in Figure D.6.

The experimental results were extracted and post-processed using a Python script, ensuring accurate data refinement for stiffness evaluation. The radial stiffness was computed within the 23–24 mm FD range, resulting in a stiffness $k_{Radial-30\%}^{Stent}$ of 1.2945 N/mm for the 30% crimping case, with an R-value of 99.11%, while the 80% crimping case yielded a stiffness of $k_{Radial-80\%}^{Stent}$ 1.2986 N/mm with an R-value of 99.31%. These experimental results are compared with the FE model predictions in Table 3.15, validating the implemented material model.

A notable feature of the obtained curve is the pronounced spike in reaction forces around an 8 mm diameter, attributed to stent self-contact at high crimping levels. This behavior emphasizes the importance of accurately modeling geometric constraints, as they have a significant influence on the mechanical response.

Additionally, an hysteresis cycle is observed even for the limited 30% crimping test, indicating that a phase transformation begins to occur even under relatively low stress levels. This suggests that the superelastic behavior of NiTiNol is already active at moderate deformations, influencing the stent's structural performance throughout the loading-unloading cycle. The experimental findings align with finite element simulations discussed in Section 3.2.2.1, confirming the presence of nonlinear material response.

3.1.3.2. CRUSH RESISTANCE TEST

A total of five tests per specimen were conducted on five stent specimens, measuring sensed reaction forces (RFs) during compression. The full dataset and statistical results are provided in Appendix B (Table B.18).

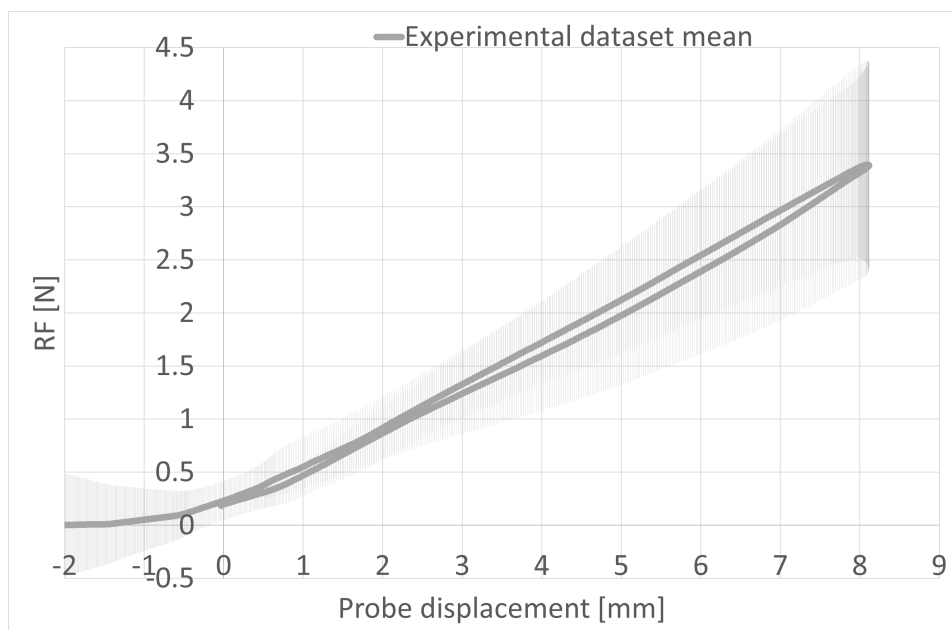


Figure 3.4. Mean reaction force–displacement curve with experimental standard deviation from the crush resistance test on NiTiNol stent specimens.

A Python post-processing script was used to analyze the stent's mechanical response and quantify variability across multiple runs. The mean stiffness was computed over the 0.5–3.5 mm displacement range, ensuring comparability across specimens. Individual stiffness values were then evaluated against the average stiffness per specimen to assess intra-sample variability. The found mean stiffness was $k_{Crush}^{Stent} = 0.4018$ N/mm, with a standard deviation of 0.012, confirming the consistency of the mechanical response across tested samples. A comparison between these experimental values and the FE model predictions is provided in Table 3.16, reinforcing the validity of the obtained tridimensional configuration for the stent FE model.

The mean reaction force vs. displacement curve is presented in Figure 3.4, while Figure D.9 illustrates the complete dataset, showing the variability across individual runs.

The statistical distribution of the measured stiffness values is shown in Figure 3.6, while Figures D.7a and D.7b provide a comparative breakdown of stiffness values for each run, grouped by specimen.

3.1.3.3. INDENTATION TEST

The indentation test was performed on five TAVI valve specimens, with five test repetitions per specimen, recording the reaction forces sensed by the load cell during the indentation process. The full dataset, including individual stiffness values and environmental conditions, is provided in Appendix B (Table B.19).

A Python post-processing script analyzed the mechanical response and quantified variations across runs and specimens. The assembly stiffness was computed over the 3–5 mm indentation range to ensure consistent comparability between trials. The mean stiffness was found to be $k_{Indent}^{TAVI} = 0.3058$ N/mm, with a standard deviation of 0.022, confirming the reliability of the test data across specimens. A comparison between these experimental values and the FE model predictions is provided

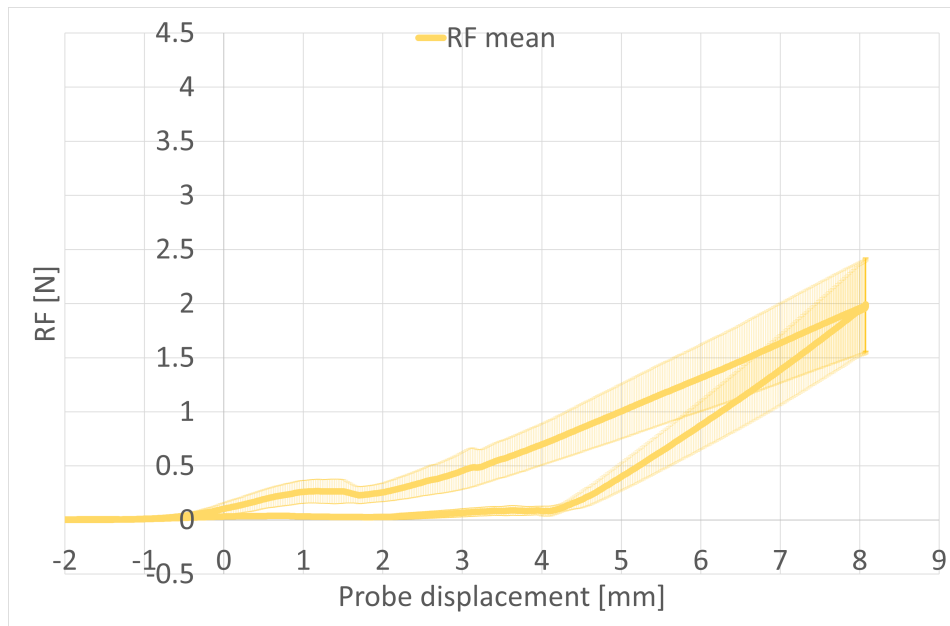


Figure 3.5. Mean reaction force–displacement curve with experimental standard deviation from the indentation test on complete TAVI valve specimens.

in Table 3.17, completing the validation of the complete TAVI FE model. Table 3.4 contains a concise overview of the mean stiffnesses k_{Radial}^{Stent} , k_{Crush}^{Stent} and k_{Indent}^{TAVI} found in the validation simulations.

Figure 3.5 presents the mean force-displacement curve, while Figure D.10 illustrates the variability across individual tests.

A distinct feature in the loading curve is the pronounced bump between 0 and 2 mm of the indenter total displacement range, which corresponds to the folding of the leaflets along the loading axis. This deformation stage introduces a localized increase in reaction force before further compression occurs.

The statistical distribution of stiffness values is provided in Figure 3.6, while Figures D.8a and D.8b compare retrieved stiffnesses per sample, illustrating structural response variability.

3.2. FE MODELLING AND COMPUTATIONAL SIMULATION ACTIVITIES FINDINGS

3.2.1. MODEL DEVELOPMENT OUTCOMES

3.2.1.1. STENT MODEL GEOMETRICAL PARAMETERS

The geometrical parameters of the stent model, which undergo validation as described in Section 2.3.2, were extracted at the end of the Stent Shaping simulation (Step 2 of the model development pipeline) using a Python post-processing script.

The script identifies FD by locating the node with the maximum radial coordinate, while ID is determined from the radial coordinate of the internal node at the tip of the stent. The specimen height (H) is computed by identifying the node with the highest z-coordinate at the intersection of the internal surface nodes and the lateral symmetry-bounded surfaces, comparing it to the lowest z-coordinate node on the external surface. RT is measured at the stent tip, as shown in Figure 3.7, where the external node is selected through set intersection in a manner similar to the internal node, and their radial coordinates are compared. The full geometrical evaluation is summarized in Table 3.3.

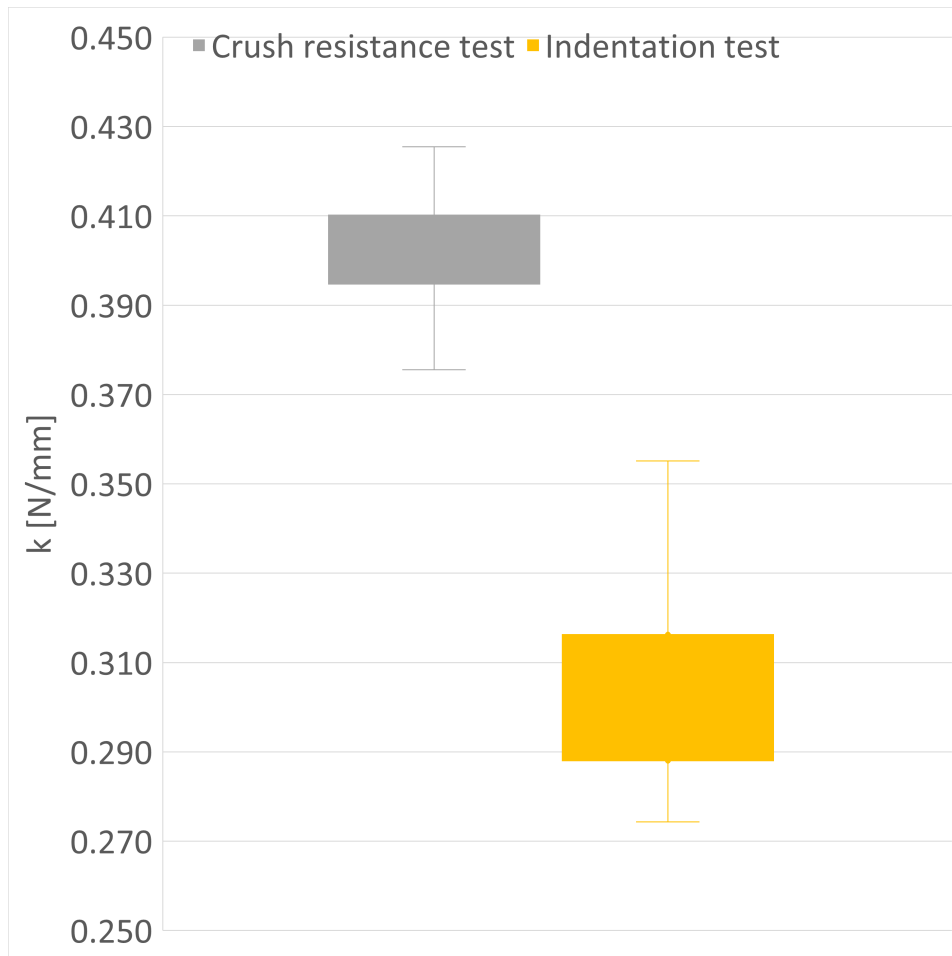


Figure 3.6. Box-and-whisker plot of evaluated experimental stiffness values from crush resistance and indentation tests, displaying mean values, interquartile ranges, and whiskers extending to the minimum and maximum measured values.

Table 3.3. Selected geometrical parameters relative to the metallic stent, as found in the stent model at the end of the Stent Shape Setting simulation and extracted by the Python postprocessing script. compared with their nominal values as provided from the manufacturing company.

Parameter	Nominal value [mm]	Model value [mm]
Flare Diameter (FD)	27.5	27.88
Internal Diameter (ID)	25.00	25.00
Height (H)	31.1	30.69
Radial Thickness (RT)	0.45	0.45

3.2.1.2. MATERIAL MODEL PARAMETERS FITTING

The material model parameters used in the finite element simulations were derived from an independent dataset consisting of uniaxial tensile stress tests performed on three NiTiNol samples. The Auricchio material model [7] was calibrated through a Monte Carlo parameter fitting procedure to ensure accurate representation of the superelastic behavior of NiTiNol.

The fitting process required 58 simulation runs and converged to a NRMSE of 8.0% for the first sample, 3.89% for the second, and 4.13% for the third. The dataset did not provide sufficient information to determine the loading and unloading transformation thresholds in compression, leaving

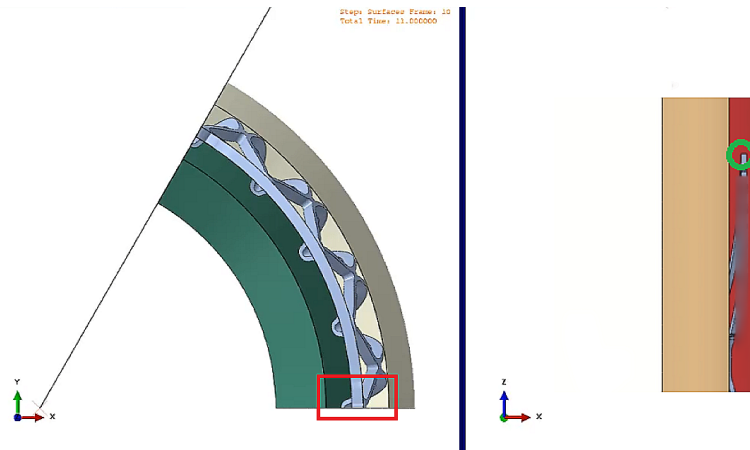


Figure 3.7. Steps of the Stent Shape Setting simulation, including the used shaping surfaces. The detail marked via a red square over the XY-plane view on the left highlights the top tip of the metallic stent model, where RT is evaluated by the Python postprocessing script.

these values undefined. The final fitted material parameters are presented in Table B.20.

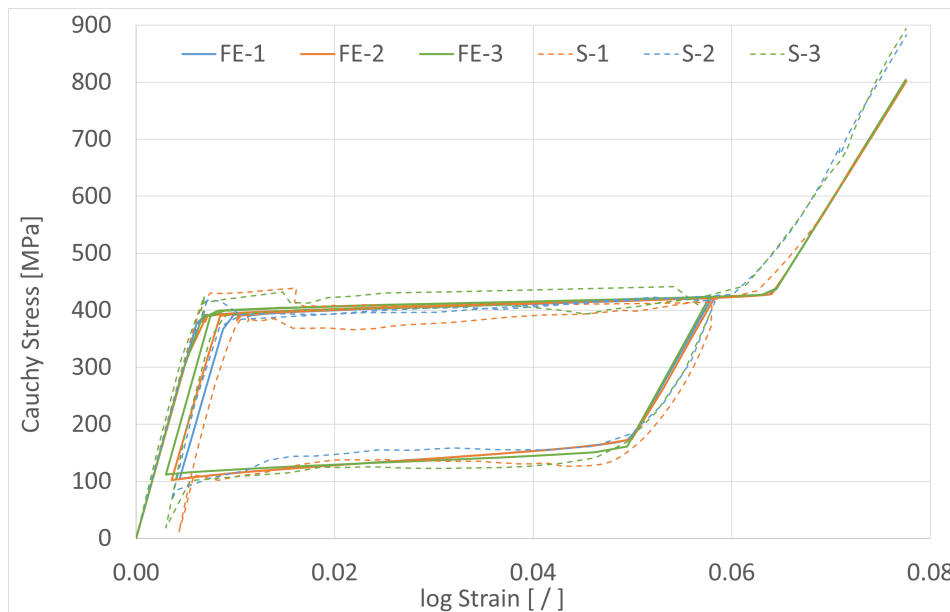


Figure 3.8. Stress-strain curves of the NiTiNol material, comparing experimental data from the partner company (dotted lines) with Monte Carlo parameter fitting results (solid lines)

Figure 3.8 illustrates the simulation performance compared to the experimental datasets, demonstrating the calibration accuracy. The final material properties were obtained by weighting the results of the individual simulation runs to ensure an optimal balance across all tested samples, achieving a total objective function NRMSE of 5.34%.

3.2.2. VALIDATION SIMULATIONS DATA ANALYSIS

3.2.2.1. RADIAL COMPRESSION TEST SIMULATION RESULTS

The radial compression test simulations evaluated the structural response of the stent model under 30% and 80% diameter reduction conditions. The analysis focused on the reaction force vs. displacement behavior and the computed radial stiffness k_{Radial}^{Stent} within the 24–23 mm FD range,

extracted via a Python post-processing script.

Results show that, for the 30% diameter reduction scenario, the model achieved a radial stiffness $k_{Radial-30\%}^{Stent}$ of $1.2214 \frac{N}{mm}$, with a high correlation coefficient (R-value = 99.83%), indicating a reliable structural response. In the 80% diameter reduction case, the $k_{Radial-80\%}^{Stent}$ resulted equal to $1.3215 \frac{N}{mm}$, with an R-value of 97.94%, thus without demonstrating greater deformation-induced variations along similar interpolation ranges.

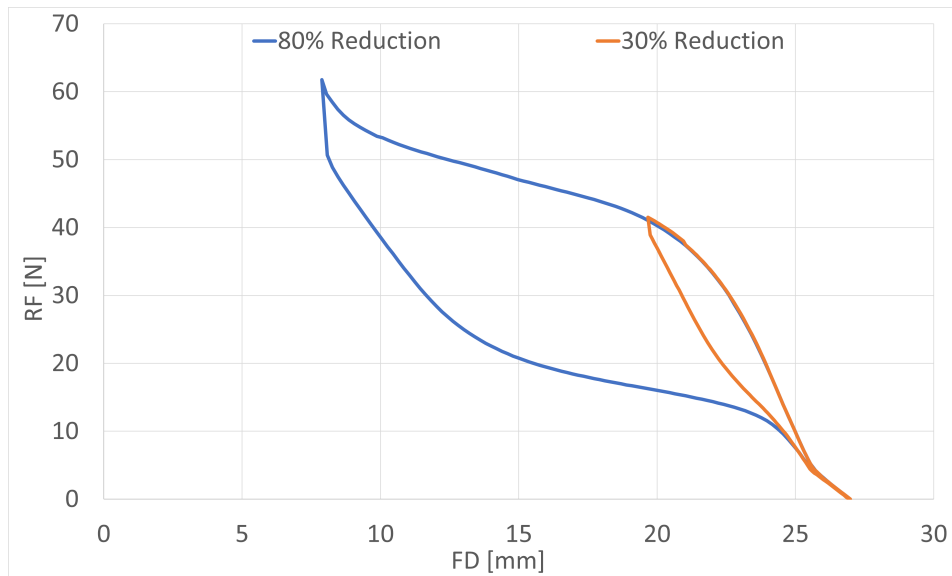


Figure 3.9. Reaction force vs. flare diameter curve from the FE validation models of radial compression tests, comparing the structural response under 30% and 80% original diameter reduction conditions.

The reaction force-displacement curves shown in Figure 3.9 highlight the nonlinear mechanical response of the stent, characterized by a clear hysteresis cycle and a noticeable increase in stiffness at higher compression levels. The observed behavior aligns with the expected deformation mechanics of the model, emphasizing the role of structural constraints and material properties in shaping its performance.

3.2.2.2. STENT MODEL CRUSH RESISTANCE TEST SIMULATION RESULTS

The crush resistance test simulations assessed the mechanical response of the stent model under axial compression, analyzing the reaction force vs. displacement behavior over the 0.5–3.5 mm range. The radial stiffness k_{Crush}^{Stent} was extracted using a Python post-processing script, ensuring consistency in the evaluation process.

The results indicate that the model exhibited a k_{Crush}^{Stent} of 0.3781 N/mm, with an R-value of 99.90%. The force-displacement curve, shown in Figure 3.10, highlights the progressive stiffening behavior of the structure, demonstrating the influence of geometrical constraints and material properties on the stent's load-bearing capacity.

3.2.2.3. INDENTATION TEST SIMULATION RESULTS

The indentation test simulations assessed the mechanical response of the complete TAVI valve assembly, evaluating the structural stiffness k_{Indent}^{TAVI} over the 3-5 mm indentation range.

The results show a stiffness of 0.3805 N/mm, with an R-value of 94.87%, highlighting a well-correlated structural response compared to the previous tests, although the increased model complexity afflicts the interpolation process as demonstrated by the lower R-value. The force-displacement curve reveals a progressive stiffening trend, with a noticeable nonlinearity attributed to de-

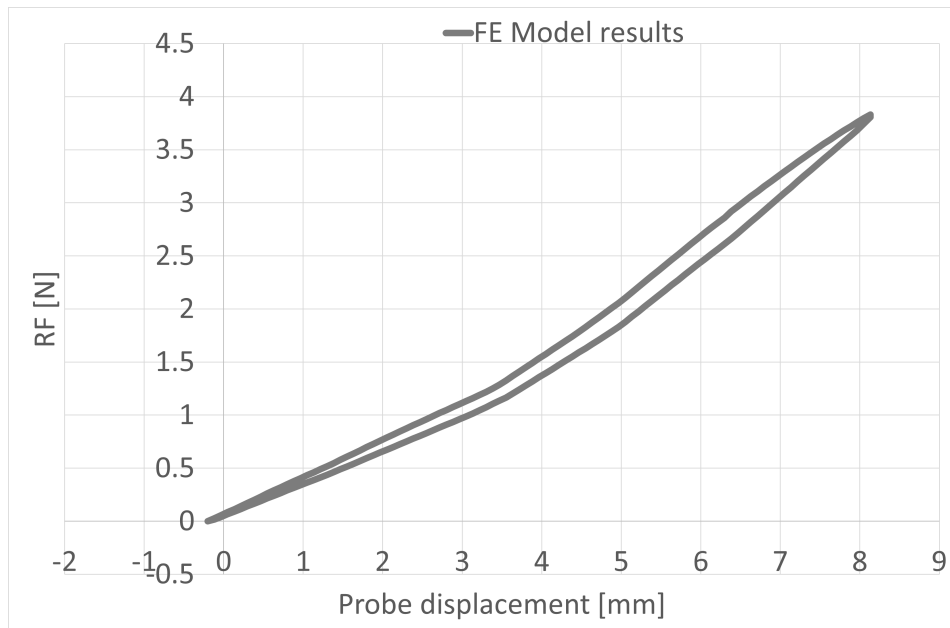


Figure 3.10. Reaction force vs. top plate vertical displacement curve from the FE simulation of the crush resistance test on the stent model, illustrating the progressive stiffening behavior of the structure.

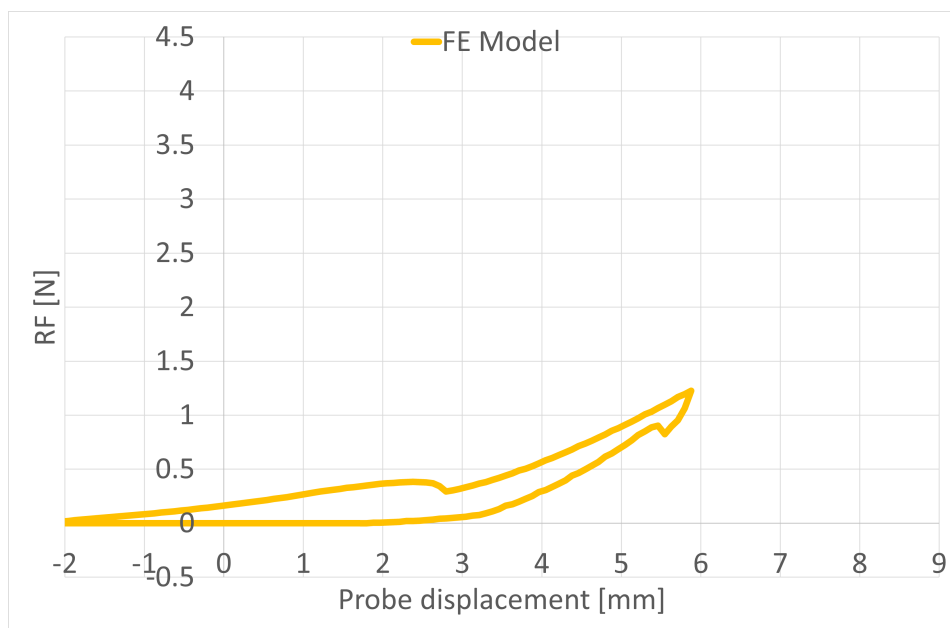


Figure 3.11. Reaction force - indenter probe displacement curve obtained for indentation test simulation, together with the characteristic small bump observed between 1 - 3 mm indentation and attributed to the internal folding of the polymeric leaflets

formation mechanisms within the leaflets and structural interactions. A small dip in the sensed reaction forces around 2-3 mm, similar to the one observed in the experimental data, corresponds to the folding of the leaflets along the loading axis.

The findings confirm the complex mechanical behavior of the assembled model under indentation, emphasizing the influence of material properties, geometrical constraints, and the accuracy of interaction modeling on the simulation results.

Table 3.4. Summary of stiffness values obtained from FE model validation simulations, including radial compression, crush resistance, and indentation tests, with corresponding correlation coefficients

Model stiffness	k [N/mm]	$R_{value}^{\%}$
$k_{Radial30\%}^{Stent}$	1.2214	99.83
$k_{Radial80\%}^{Stent}$	1.3215	97.94
k_{Crush}^{Stent}	0.3781	99.90
k_{TAVI}^{Indent}	0.3805	94.87

3.3. VERIFICATION, VALIDATION AND UNCERTAINTY QUANTIFICATION ACTIVITIES RESULTS

3.3.1. MODEL VERIFICATION

3.3.1.1. NSE ESTIMATION

The first three solver parameters were tested using the 1/4th scaffold ring sealing structure cell model shown in Figure 2.10, while the fourth and fifth parameters were evaluated using a dedicated scaffold-indenter half-symmetry model.

Table 3.5. Numerical solver error analysis results, showing the evaluated radial stiffness k_{NSE} for nominal, minimum, and maximum values of explored solver parameter ranges

Parameter	Case	k_{NSE} [N/mm]	$R_{value}^{\%}$	$E_k^{\%}$
Stent	Nominal	0.036	99.79	
Scaffold	Nominal	0.013	99.88	
Dissipated energy	Max	0.036	99.79	0.00
Dissipated energy	Min	0.036	99.79	0.02
ALLSDTOL	Max	0.036	99.79	0.02
ALLSDTOL	Min	0.036	99.79	-1.10
Dynamic step application	Moderate dissipation	0.013	99.84	0.55
NiTi contact	Max	0.036	99.79	0.02
NiTi contact	Min	0.036	99.79	0.01
Leaflet contact	Max	0.013	99.88	0.11
Leaflet contact	Min	0.013	99.86	-0.11

The stiffness calculations, presented in Table 3.5 and illustrated in Figure D.11a and detail Figure D.11b, indicate that no significant variations were observed across the tested simulations, except for the minimum value of parameter 2, where no stabilization energy was allowed in the simulation. While the variations in stiffness appear minor, further analysis of the internal energy (ALLIE) and stabilization energy (ALLSD) reveals that the simulation results are invalid, as the ratio between ALLSD and ALLIE exceeds the 5% threshold, violating the numerical stability requirements. Based on these findings, the selected nominal numerical solver parameters were considered verified within the scope of this project.

3.3.1.2. DE INFLUENCE EXPLORATION

Stent model DE analysis The 1/4th scaffold ring sealing structure cell was used in **Test 1** of the mesh convergence study to select an appropriate global seed size (GBS) for the stent model. The results indicate that GBS = 0.1125 mm exhibited an underestimation followed by an overestima-

tion of the sensed reaction forces along the transformation strain, compared to $GBS = 0.056$ mm, suggesting that only two elements along ST suffer from hourglassing, even when mitigated by the second-order C3D20R elements (Figure 3.12a and detail Figure 3.12b). On the other hand, $GBS = 0.014$ mm significantly increased computational time by nearly 70% compared to $GBS = 0.028$ mm, without appreciable improvements in accuracy.

Table 3.6. Results of DE analysis (Test 1), comparing four global seed size values (GBS) in terms of evaluated stiffness precision, sensed reaction forces precision and computation time.

GBS [mm]	$k[\frac{N}{mm}]$	$E_k\%$	$R_{value}\%$	$RF_{r=17}$ [N]	$\Delta_{RF}\%$	T_{Cmpl} [s]	$\Delta T_{Cmpl}\%$
0.1125	0.0375	0.26	99.99	0.1969	3.41%	696	-99.8
0.056	0.0374	0.14	99.98	0.1975	3.11%	7090	-97.7
0.028	0.0374	0.05	99.98	0.1998	1.95%	96104	-68.3
0.014	0.0374		99.98	0.2038		303502	

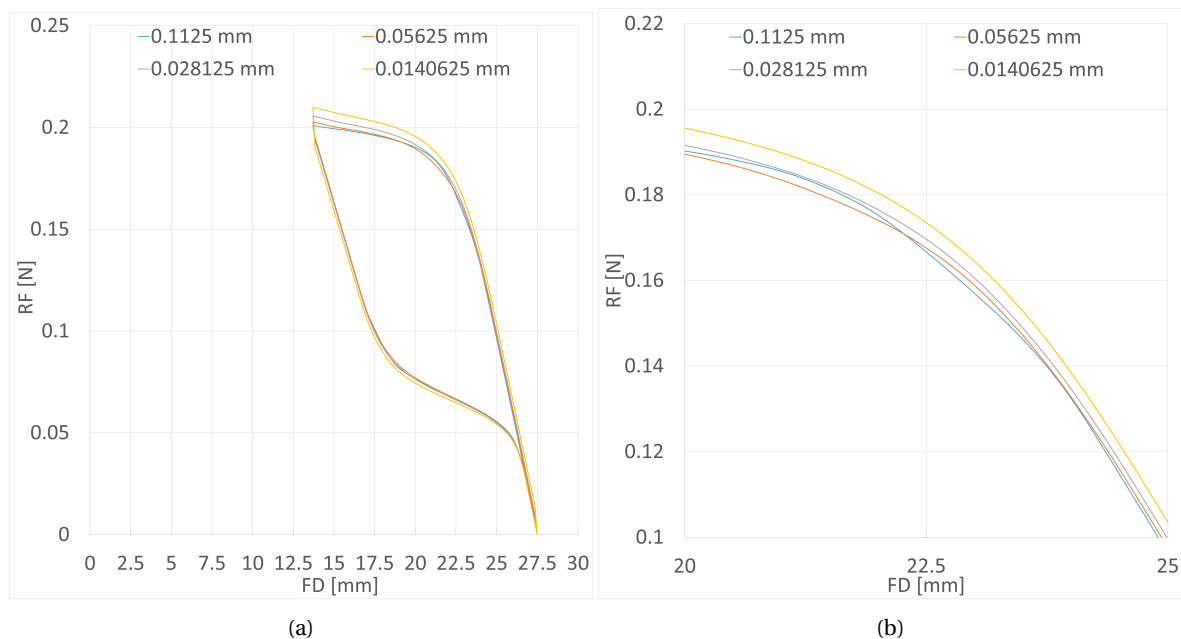


Figure 3.12. Stent model discretization error analysis, Test 1 results. The radial displacement - reaction force curves as found for the four different GBS size tested. Figure 3.12a shows the complete RF-FD curves, while Figure 3.12b focuses on the overshoot noticeable for the coarsest mesh at the beginning of the transformation phase characteristic plateau.

Test 2 refined the selection by using $GBS = 0.056$ mm, 0.028 mm, and 0.014 mm on a selection of C3D8, C3D8I, C3D8R and C3D20R elements. While $GBS = 0.056$ mm demonstrated notable improvements in computational efficiency, it also provided reliable results ($<1\%$ error) only when using second-order elements (C3D20R) or incompatible mode elements (C3D8I), reinforcing the strong dependence of the results on the ability of the finite elements to properly represent shear stresses. The C3D8I elements consistently delivered acceptable results, showing particularly good runtime performance at $GBS = 0.056$ mm. They were only surpassed by second-order elements, which, while highly accurate, increased computational time by 28.6% in coarser meshes and almost doubled it for $GBS = 0.014$ mm. C3D8 full integration elements produced more credible results than their reduced integration counterparts (C3D8R), particularly at $GBS = 0.028$ mm and 0.014 mm. Consequently, C3D8 and C3D8R were tested in Test 3 only at $GBS = 0.028$ mm and 0.014 mm, while C3D8I elements were propagated using $GBS = 0.056$ mm.

Table 3.7. Discretization error analysis results, comparing the performance of different element types under various global seed sizes (GBS) in terms of evaluated stiffness, accuracy, and computational efficiency.

Elem.Type	GBS [mm]	$k[\frac{N}{mm}]$	$E_k^{\%}$	$R_{value}^{\%}$	T_{Cmpl} [s]	$\Delta T_{Cmpl}^{\%}$
C3D20R	0.056	0.0375	0.14	99.98	7090	-97.7
	0.028	0.0374	0.05	99.98	96104	-68.3
	0.014	0.0374		99.98	303521	
C3D8	0.056	0.0380	1.66	99.99	13612	-95.5
	0.028	0.0376	0.54	99.98	80217	-73.6
	0.014	0.0375	0.13	99.97	143741	-52.6
C3D8I	0.056	0.0377	0.85	99.98	5822	-98.1
	0.028	0.0370	0.29	99.98	86790	-71.4
	0.014	0.0373	0.08	99.98	154994	-48.93
C3D8R	0.056	0.0356	0.85	99.99	5579	-98.1
	0.028	0.0370	0.29	99.98	86892	-71.4
	0.014	0.0373	0.08	99.98	164303	-45.9

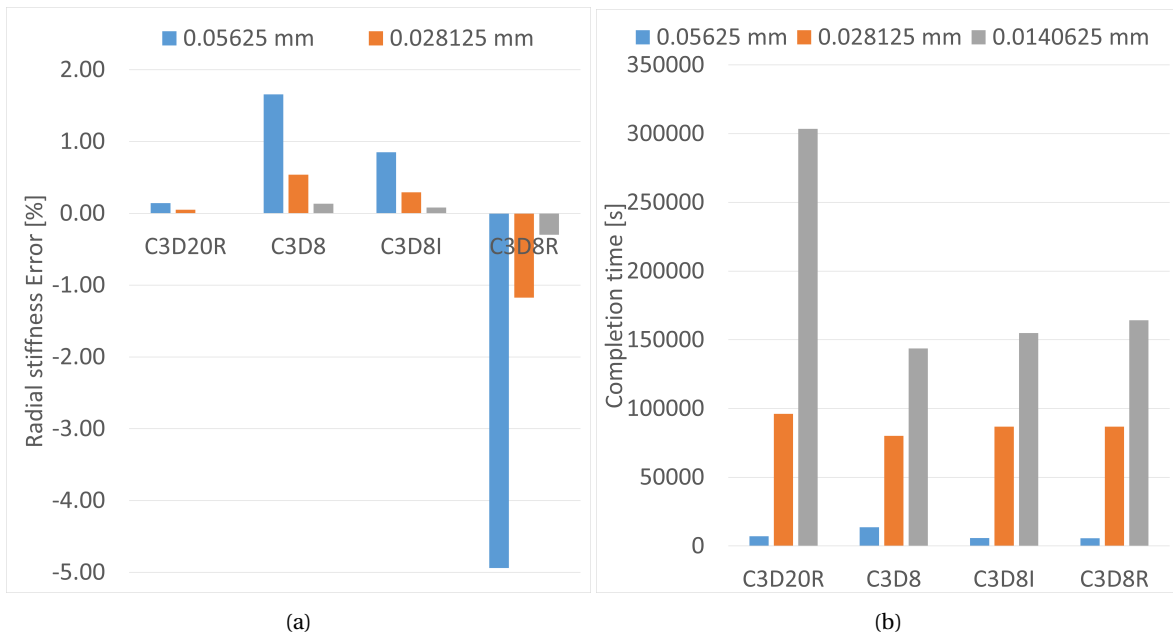


Figure 3.13. Stent model discretization error analysis Test 2 results. Figure 3.13a shows the percentage error in stiffness evaluation as depending from the element type, while Figure 3.13b gives an overview of the completion time (in seconds) as a function of the element type.

Test 3, evaluating the number of elements along the RT, revealed that C3D8R elements failed when compared to the C3D20R mesh with 32 elements along RT, whereas C3D8 only failed at 4 elements along RT. The C3D8I elements with 4 elements along RT provided the best compromise between runtime and accuracy, but their formulation was highly dependent on aspect ratio, making them unsuitable for the biased meshing approaches tested in Stent DE Tests 4 and 5.

Test 4 introduced a biased mesh strategy, using C3D8R-4RT, C3D8-4RT, and C3D8-8RT, where -xRT denotes the number of elements along RT. As expected, increased element density in high-stress bending zones improved solution accuracy, as shown in Table. However, all reduced integration elements failed in terms of both computational time and result accuracy and were removed from

Table 3.8. Discretization error analysis results, examining the influence of the number of elements along the radial thickness (RT) under different element types and global seed sizes (GBS) in terms of stiffness evaluation and computational performance.

Elem.Type	GBS [mm]	RT	ST	$k[\frac{N}{mm}]$	E_k	T_{Cmpl} [s]	$\Delta T_{Cmpl}^{\%}$
C3D8I	0.056	4	4	0.0377	0.87	2497	-99.2
	0.056	8	4	0.0377	0.85	5822	-98.1
C3D8R	0.028	4	8	0.0369	-1.28	16983	-94.4
	0.028	8	8	0.0370	-1.19	37492	-87.6
	0.028	16	8	0.0370	-1.17	86892	-71.4
C3D8	0.028	4	8	0.0379	1.19	14263	-95.3
	0.028	8	8	0.0377	0.68	32283	-89.4
	0.028	16	8	0.0376	0.54	80217	-73.6
C3D20R	0.014	32	16	0.0374		303521	

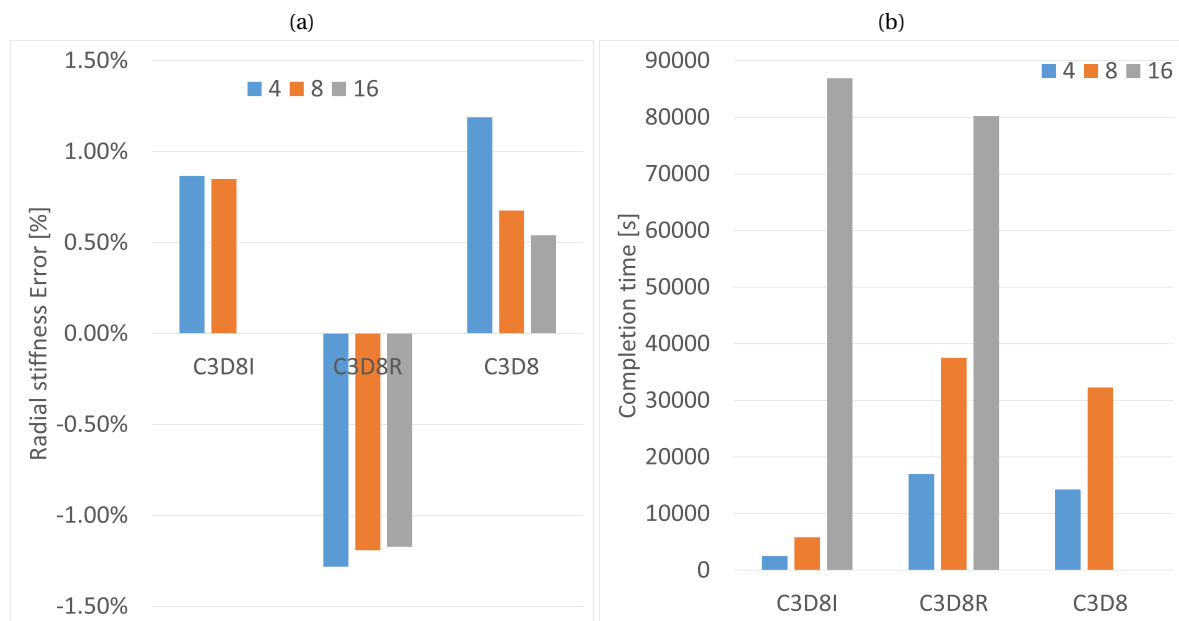


Figure 3.14. Stent model discretization error analysis Test 3 results. Figure 3.14a shows the percentage error in stiffness evaluation as depending from the number of elements along RT, while Figure 3.13b gives an overview of the influence of the number of elements along RT over the completion time (in seconds).

further testing. The C3D8 elements, on the other hand, performed well with a bias ratio of 2.0 along ST, exhibiting minimal hourglassing issues. Due to its strong runtime performance and an error only 0.07% above the threshold, C3D8-4WT-3STb was retained for Test 5.

Test 5 identified C3D8-4RT-2STb-1Sb and C3D8-4RT-3STb-4.5Sb as highly accurate, with the latter being 2.5 times faster. In terms of computational efficiency, the C3D8I elements at GBS = 0.056 mm provided results within the 1% tolerance limit in the shortest runtime, making them an effective choice for balancing computational cost and accuracy.

In conclusion, the C3D8I element, GBS = 0.056 mm with 4 elements along RT and no bias mesh results to ensure the shorter analysis execution times without hindering the quality of the obtained results.

Table 3.9. Discretization error analysis, exploration of the influence of the implementation of a biased meshing approach along the structural thickness ST (Test 4). The table compares the Test 4 analysis results with the results from the C3D20R-0.014-32RT-16ST case.

Element	RT	ST	Bias ST	$k[\frac{N}{mm}]$	$E_k^{\%}$	T_{Cmpl} [s]	$\Delta T_{Cmpl}^{\%}$
C3D8R	4	8	1	0.0369	-1.28	16983	-94.4
	4	6	1.5	0.0365	-2.37	12362	-95.9
	4	5	2	0.0358	-4.41	9875	-96.7
	4	4	3	0.0343	-8.32	23981	-92.1
C3D8	4	8	1	0.0379	1.19	14263	-95.3
	4	6	1.5	0.0378	0.87	10938	-96.4
	4	5	2	0.0375	0.22	9713	-96.8
	4	4	3	0.0370	-1.07	7972	-97.4
C3D8	8	8	1	0.0377	0.68	32283	-89.4
	8	6	1.5	0.0376	0.37	25790	-91.5
	8	5	2	0.0373	-0.25	22643	-92.5
	8	4	3	0.0369	-1.48	21323	-93.0
C3D20R	32	16	1	0.0374		303521	

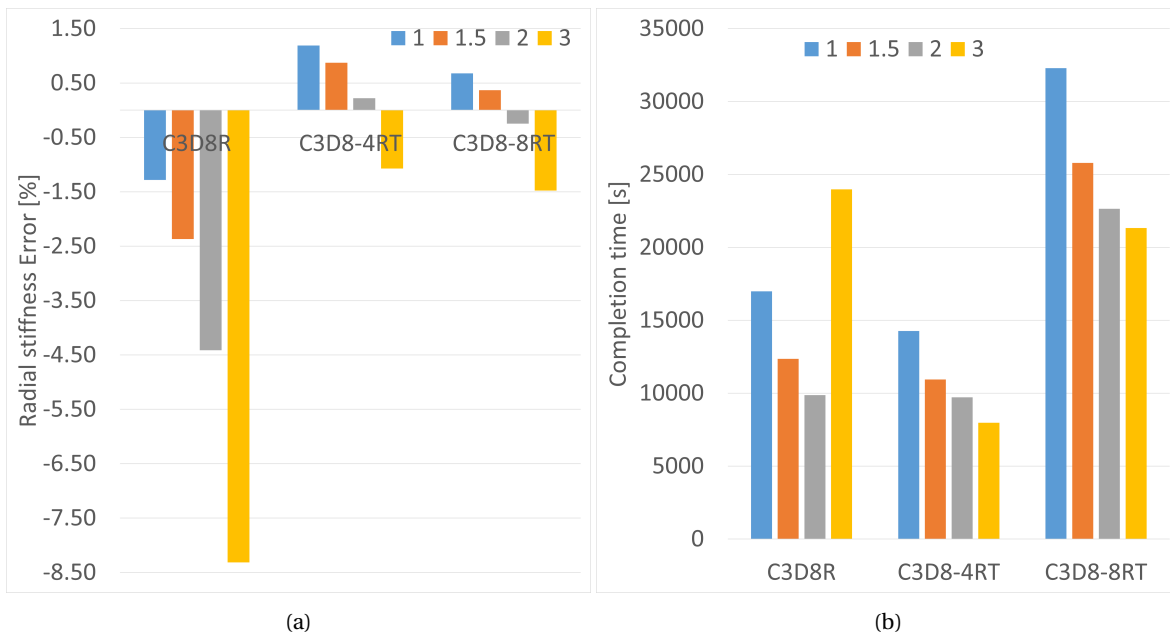


Figure 3.15. Stent model discretization error analysis Test 4 results. Figure 3.15a shows the percentage error in stiffness evaluation as depending from the bias factor along ST, while Figure 3.14b gives an overview of the influence of implementing a biased approach along ST over the completion time (in seconds).

Table 3.10. Discretization error analysis, exploration of the influence of the implementation of a biased meshing approach along the longitudinal direction of the stent feeler (Test 5). The table compares the Test 5 analysis results with the results from the C3D20R-0.014-32RT-16ST case.

Element	RT	STb	Bias L	$k[\frac{N}{mm}]$	$E_k^{\%}$	T_{Cmpl} [s]	$\Delta T_{Cmpl}^{\%}$
C3D8	4	2.0	1.0	0.0375	0.22	9713	-96.8
	4	2.0	1.5	0.0376	0.34	7316	-97.6
	4	2.0	3	0.0377	0.84	4860	-98.4
	4	2.0	4.5	0.0380	1.49	3913	-98.7
C3D8	4	3.0	1	0.0370	-1.07	7972	-97.8
	4	3.0	1.5	0.0371	-0.96	6490	-97.9
	4	3.0	3	0.0373	-0.45	4475	-98.5
	4	3.0	4.5	0.0375	0.20	3784	-98.7
C3D8I	4	4	1	0.0377	0.87	2497	-99.18
C3D20R	32	16	1	0.0374		303521	

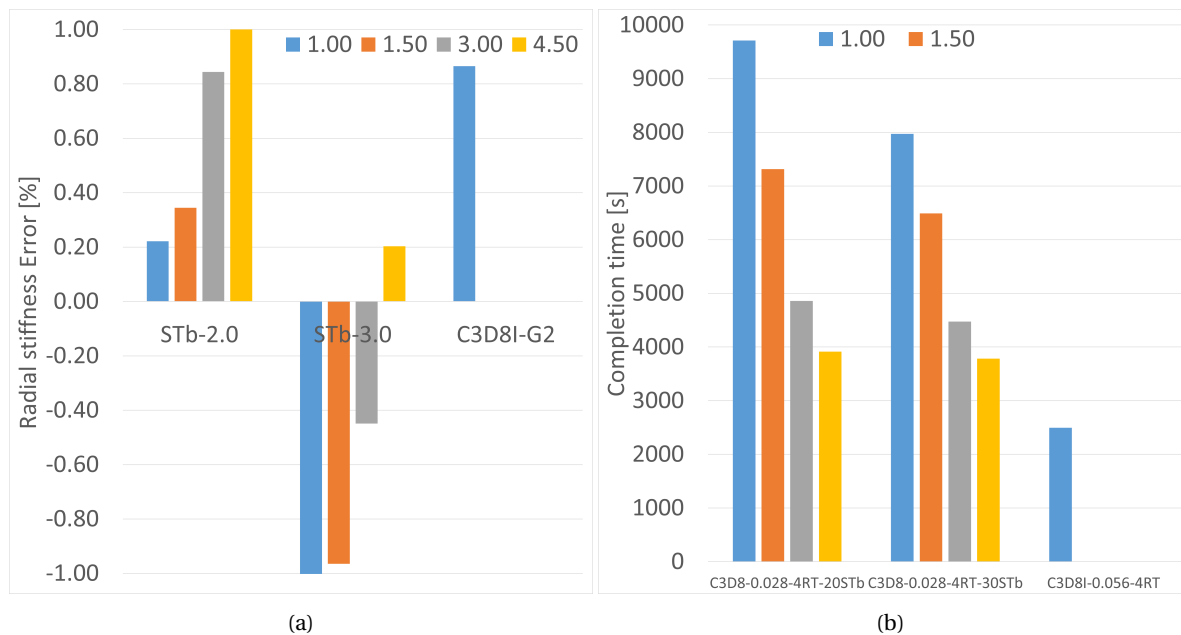


Figure 3.16. Stent model discretization error analysis Test 5 results. Figure 3.16a shows the percentage error in stiffness evaluation as depending from the application of a bias factor along the longitudinal direction of the stent feeler, while Figure 3.16b gives an overview of the influence of implementing a biased approach along the feeler over the analysis completion time (in seconds). For an easier readability of Figure 3.16b, the completion time relative to the C3D20R elements, uniform mesh has been neglected.

Scaffold model DE analysis The mesh of the leaflet model consists of a simple cylindrical shell surface, with thickness values derived from the experimental activities presented in Section 2.1.1. Due to its simplified geometry and the narrower range of possible elements, the DE analysis for the leaflet model consists of two tests.

Test 1 evaluated four different GBS values (1 mm, 0.5 mm, 0.25 mm, and 0.125 mm) to assess their impact on model accuracy and computational efficiency. The results revealed a negligible error in the radial stiffness estimation (-0.68%) and reaction force tracking (1.79%), suggesting that stiffness-related calculations are relatively insensitive to mesh refinement. However, as the leaflet model employs shell elements, it is particularly sensitive to in-plane stress distributions. The results indicate that the coarser mesh underestimated minimum in-plane shear stresses by almost 30%, as shown in Figure 3.17a. The computational cost followed an exponential trend, increasing five-fold between the finest mesh and GBS = 0.25 mm, while the transition from GBS = 0.5 mm to GBS = 0.25 mm led to an almost tenfold increase in computational cost, following an exponential scaling behavior, as shown in Figure 3.17b.

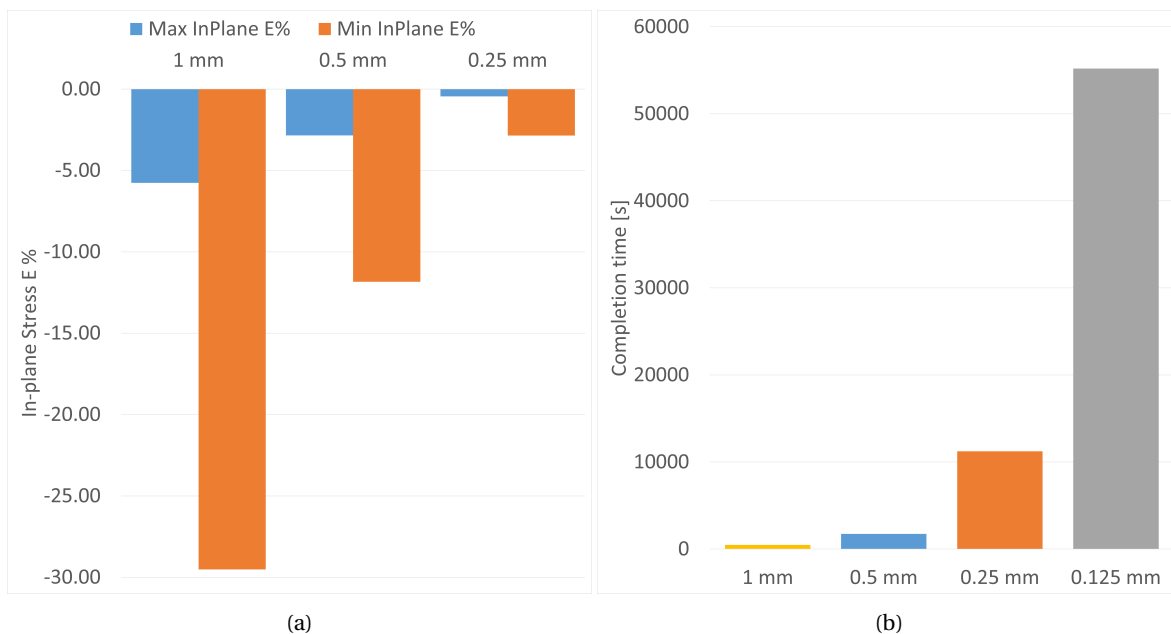


Figure 3.17. Results overview of the Scaffold Discretization Error analysis Test 1. Figure 3.17a shows the percentage error on the maximal and minimal in-plane stresses as per function of the global mesh seed sizes (1, 0.5 and 0.25), while Figure 3.17b shows the influence of the global mesh size on the analysis completion time, in seconds.

Test 2 focused on element type selection, comparing S4 and S4R 4-node shell elements, analyzing the same quantities as in Test 1. While no significant variations were observed in radial stiffness or reaction force tracking, the minimum in-plane stress estimation error increased by -11.84% in both GBS = 0.5 mm cases, leading to its exclusion from further analysis. With GBS = 0.25 mm, the differences between S4 and S4R elements were minimal in terms of accuracy. However, S4R elements completed the analysis 36.6% faster, making them the final choice for the leaflet model mesh.

The scaffold DE analysis results are presented in three separate tables: Table 3.11, detailing the stiffness and reaction force estimation errors, Table 3.12, reporting the in-plane stress evaluation, and Table 3.13, listing the computational completion times. The full dataset, including all variables in a single table, can be found in Appendix B.2, where Table B.21 provides the complete breakdown.

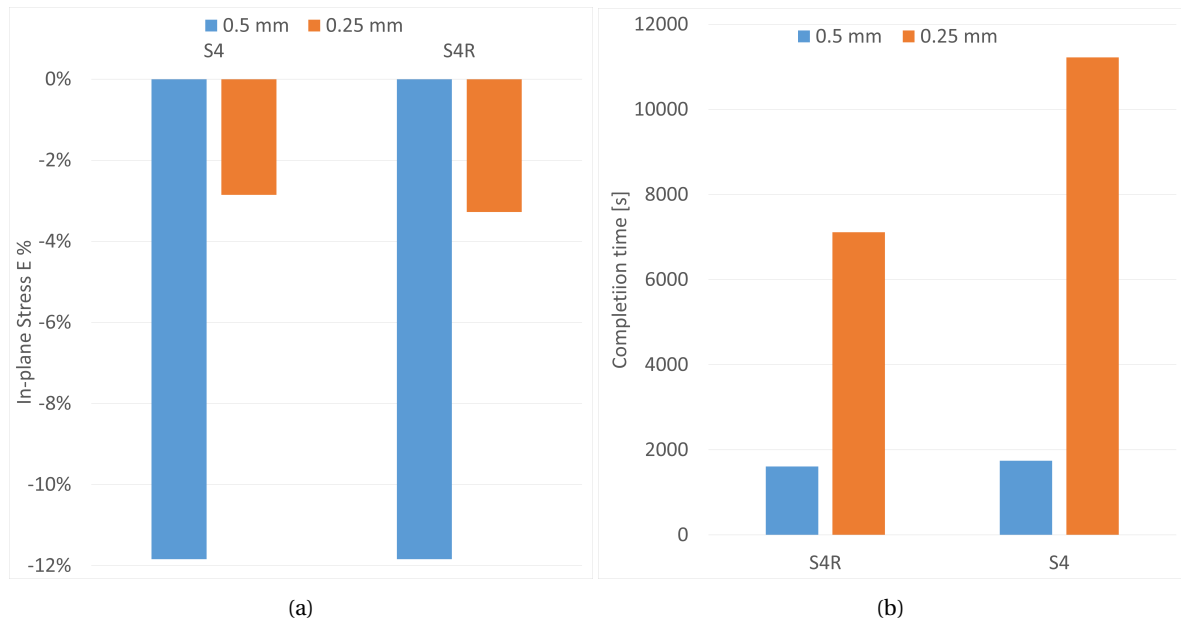


Figure 3.18. Results overview of the Scaffold Discretization Error analysis, Test 2. The influence of the element type over the model accuracy in accurately representing the maximal and minimal in-plane stresses is shown in Figure a, while Figure 3.18b shows the element type influence over the analysis completion time, in seconds.

Table 3.11. Percentage errors in stiffness and reaction force evaluation from the Scaffold model discretization error analysis. The table provides an overview of Test 1 (variation in global seed size, GBS) and Test 2 (comparison of element types).

Element	GBS [mm]	$E_k^{\%}$	$E_{RF}^{\%}$
S4	1	-0.68	1.79
S4	0.5	-0.68	0.44
S4R	0.5	-0.28	0.44
S4	0.25	-0.10	0.04
S4R	0.25	-0.08	0.04

Table 3.12. Percentage errors in maximal and minimal in-plane stresses from the Scaffold model discretization error analysis. The table presents results from Test 1 (variation in global seed size, GBS) and Test 2 (comparison of element types).

Element	GBS [mm]	$E_{\sigma_{Max}}^{\%}$	$E_{\sigma_{Min}}^{\%}$
S4	1	-5.76	-29.52
S4	0.5	-2.84	-11.84
S4R	0.5	-2.84	-11.84
S4	0.25	-0.44	-2.86
S4R	0.25	-0.82	-3.28

3.3.2. VALIDATION STRATEGIES

3.3.2.1. GEOMETRICAL MEASUREMENTS AND MODEL GEOMETRICAL PARAMETERS COMPARISON

The experimental geometrical measurements of the stent and valve leaflet structure were compared to the nominal specifications and the obtained model parameters after the shaping simulation. Table 3.14 reports the mean experimental values and the FE model results, alongside their absolute

Table 3.13. Differences in completion time observed in the Scaffold model discretization error analysis, comparing results from Test 1 (variation in global seed size, GBS) and Test 2 (comparison of element types).

Element	GBS [mm]	T_{Cmpl} [s]	$\Delta T_{Cmpl}^{\%}$
S4	1	474	-99.14
S4	0.5	1744	-96.84
S4R	0.5	1609	-87.1
S4	0.25	11223	-79.7
S4R	0.25	7115	-87.1
S4	0.125	55198	

and relative differences from the nominal specifications.

A limited deviation is observed in FD, with experimental measurements showing a -2.39% reduction relative to the nominal specifications. This discrepancy is likely due to manufacturing tolerances and post-processing effects on the real specimens. In contrast, the FE model closely matches the nominal values, with only a +1.37% increase in FD, confirming that the computational model retains the expected stent geometry.

Similarly, ID and H show minimal deviation across both the experimental and computational cases, reinforcing the structural fidelity of the FE representation. RT, however, exhibits a 9.19% deviation in the experimental data. As with FD, this higher percentage error might arise from the relatively small nominal value of RT, where even minor absolute differences yield a larger normalized deviation. The FE model achieves a negligible absolute error of 0.02%, highlighting the sensitivity of RT measurements and potential mesh influence in the FE model.

Table 3.14. Comparison of mean experimental measurements and FE model geometrical parameters, showing absolute and percentage errors relative to nominal values, as evaluated using a Python post-processing script.

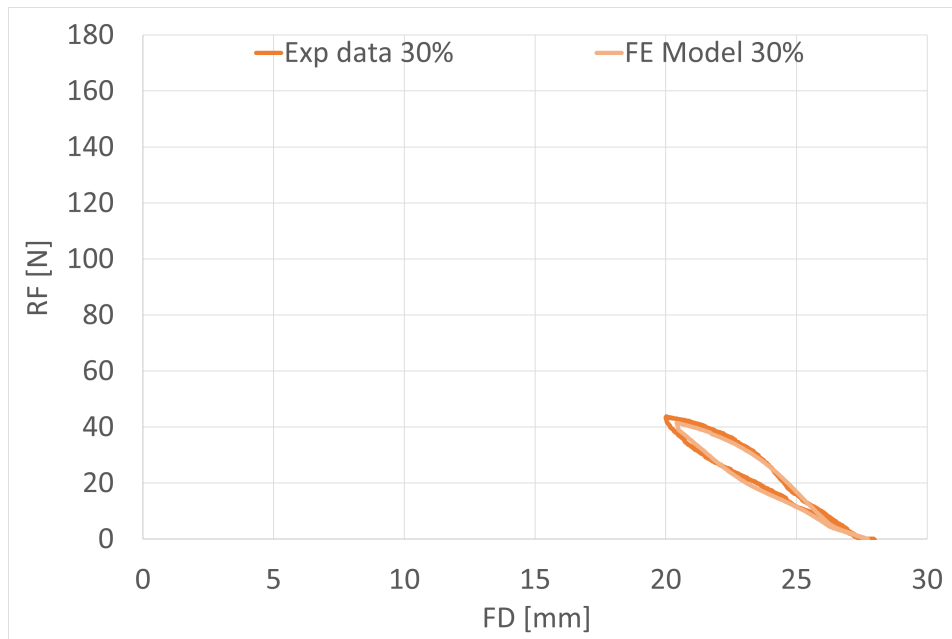
Param	Nominal [mm]	Expr Mean [mm]	FE value [mm]	Δ_{Exp} [mm]	$\Delta_{Exp}^{\%}$	Δ_{FE} [mm]	$\Delta_{FE}^{\%}$
FD	27.5	26.84	27.88	-0.658	-2.39%	+0.38	+1.37%
ID	25.00	24.91	25.00	-0.09	-0.35%	0.00	0.00%
H	31.1	30.67	30.69	-0.43	-1.38%	-0.41	-1.31%
RT	0.45	0.491	0.45	+0.04	+9.19%	0.00	+0.02%

These findings indicate that while minor deviations exist, the computational model accurately reflects the intended stent geometry and provides a reliable basis for the subsequent validation steps.

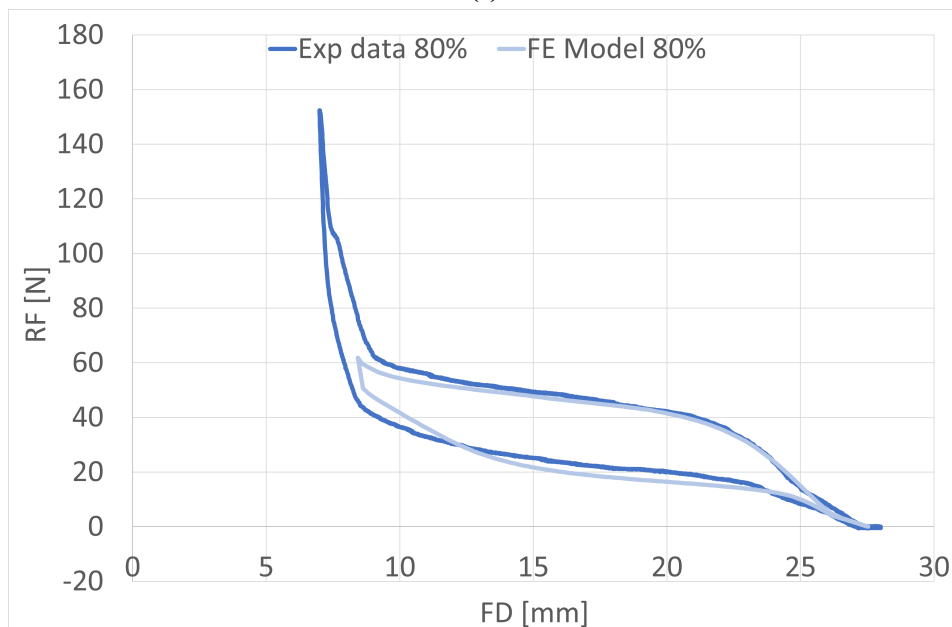
3.3.2.2. MATERIAL MODEL VALIDATION

The first validation simulation, encountered at Step 3 of the model development pipeline, is responsible for validating the NiTiNol material model against an independent dataset of three tests conducted by a partner company. A post-processing Python script extracts the flare diameter and the reaction forces sensed by the crimping surface, evaluating the stent stiffness k_{Stent}^{Rad} in the 23-24 mm FD range and comparing it with the dataset values. The script also resamples both datasets and model results over 1000 datapoints in the 20-28 mm FD range for the 30% FD compression case and in the 9-28 mm FD range for the 80% case, computing the NRMSE between the model and the dataset for both crimping and release phases.

The difference between the model and dataset stiffness values was found to be 1.77% for the 30% compression case and -5.65% for the 80% case. The NRMSE on the sensed RFs follows a progres-



(a)



(b)

Figure 3.19. Reaction force - flare diameter curves, as found in the Radial compression resistance test simulations for both the 30% and 80% FD reduction, compared with the experimental results as provided by the external partner company. Figure 3.19a highlights the comparison of the obtained 30% curves, while Figure 3.19b reports a comparison of the two 80% reduction curves.

sively worsening trend, increasing from crimping to release and from 30% to 80% compression, as reported in Table 3.15. While a deterioration in predictive accuracy for extreme deformations is expected, due to geometrical rearrangement, self-contact, and other nonlinear behaviors, it is particularly notable that a consistent deviation occurs during the release step, after the removal of loading conditions. This behavior is attributed to an imprecise and unvalidated self-contact interaction, which becomes prevalent during the 80% radial compression simulation.

Table 3.15. Results overview of the radial compression resistance test simulation, used to validate the applied NiTiNol material model, including computed stiffness values and RMSE for crimping and release phases.

Case	k_{Radial}^{Data} [N/mm]	R_{Data} value	k_{Radial}^{Model} [N/mm]	R_{Mdl} value	$E_k^{\%}$	Compress. NRMSE [%]	Release NRMSE [%]
30%	0.1294	99.11	0.1221	99.83	-5.65	5.70	7.65
80%	0.1299	99.31	0.1321	97.94	1.77	4.78	14.60

In Figure 3.19, which compares the RF-FD curve obtained from the simulation with the experimental dataset, a mathematical artifact is visible at the end of the loading phase (FD = ~20 mm). While unverified, this phenomenon likely affects the NRMSE evaluation, particularly in the most extreme region of the curve. Interestingly, this effect is not as clearly present in the 80% case, suggesting that the inclusion of the reversion point, where the transition from compression to release occurs, has a major impact on the sampling process and, consequently, on the NRMSE computation. Despite this observation, an analysis of the R-values reported in Table B.22 did not reveal a clear underlying cause for this effect.

Despite these deviations, both the stiffness evaluation error and NRMSE remain well below the 10% validation threshold, meeting the credibility scope of this project, with the exception of the NRMSE in the release phase of the 80% FD reduction test. This specific deviation is strongly influenced by self-contact effects, which become significant only at extreme deformations well beyond the nominal working range of the valve. As such, it is considered outside the COU of this project, and does not compromise the validation of the material model.

3.3.2.3. STENT MODEL VALIDATION

The crush resistance test simulation was conducted to validate the fully assembled stent model, ensuring that both the NiTiNol material behavior and the final shaped configuration were accurately modelled. This test represents a critical step in the bottom-up validation approach established within the model validation framework, reinforcing the structural fidelity of the stent geometry after the shaping simulation and prior to its integration into the complete TAVI assembly.

Table 3.16. Results overview of the crush resistance test simulation (Validation 2), used to validate the obtained NiTiNol stent geometry and complex shaping. The table includes stiffness values, correlation coefficient, percentage error, and NRMSE for compression and release phases.

k_{Crush}^{Data} [N/mm]	Data St.D.	k_{Crush}^{Model} [N/mm]	$R_{Model}^{\%}$	$E_k^{\%}$	Compress. NRMSE [%]	Release NRMSE [%]
0.4018	0.012	0.3781	99.90	-5.89%	11.52	12.19

The simulation results exhibited a 5.89% variation in stiffness evaluation within the 0.5–3.5 mm displacement range, as extracted via a Python post-processing script. The computed stiffness for the model was 0.3781 N/mm, with an R-value of 99.90%, while the experimental dataset recorded a stiffness of 0.4018 N/mm over 25 runs, with a standard deviation of 0.012, confirming a strong correlation between the numerical and experimental force response trends. However, the NRMSE evaluation revealed a progressive degradation, reaching 11.52% in compression and 12.19% in release, slightly exceeding the 10% validation threshold.

These small deviations in NRMSE are attributed to limitations in the fastening mechanism used in the experimental setup, as well as the presence of unintended self-contact in the tested specimens. This self-contact likely arises due to discrepancies between the actual experimental stent shapes and the nominal geometry on which the computational model was based. As such, the observed

variations do not stem from inaccuracies in the material model or computational framework but rather from the constraints of the experimental methodology.

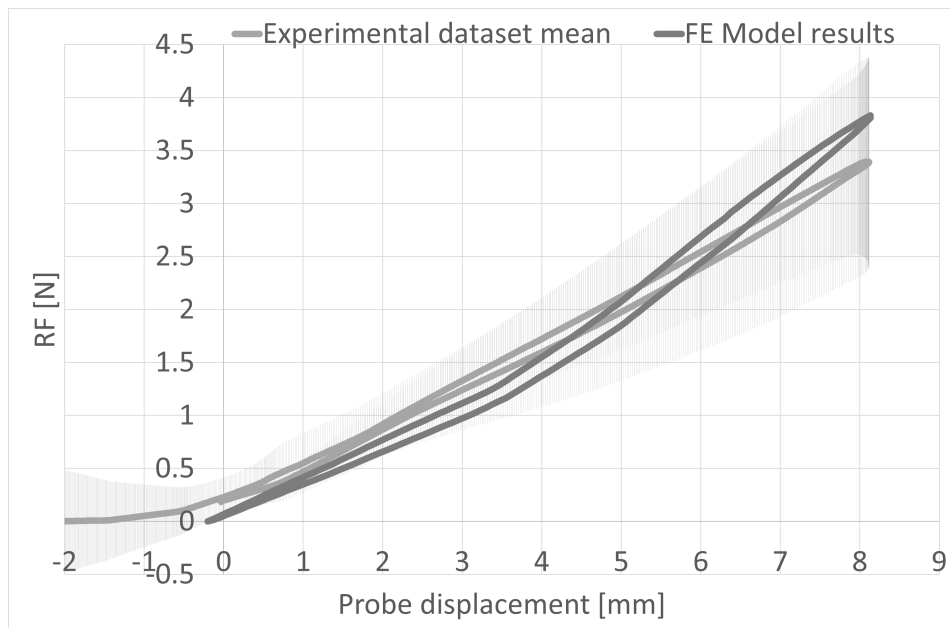


Figure 3.20. Comparison between the mean reaction force - displacement curve found for the crush resistance test, complete with the statistical standard deviation, and the curve obtained via FE simulation, as part of the validation process of the obtained geometrical configuration of the NiTiNol stent.

These results align with trends already observed in the radial compression test validation, where release phase inaccuracies were attributed to self-contact effects. In the crush resistance test, similar deviations arise from geometrical rearrangements and complex nonlinear interactions, which become more pronounced under higher strain conditions.

Despite these challenges, the stiffness evaluation and overall mechanical response remain within acceptable tolerances, supporting the conclusion that the stent model is structurally validated within the COU of this study. In fact, since these extreme loading conditions do not represent the nominal operating range of the valve, the observed deviations are considered non-critical for the model's intended application.

This validation step further reinforces the robustness of the TAVI NiTiNol stent model, ensuring its suitability for physiological simulations and, as such, the analysis of the hypothesis focus of this study.

3.3.2.4. COMPLETE TAVI MODEL VALIDATION

The indentation test simulation represents the final validation step, ensuring that the complete TAVI valve assembly accurately captures the structural interactions between its multiple components. This test evaluates the mechanical response of the fully assembled model, validating the integration of material properties, shaped geometry, and interaction forces under indentation loading.

The stiffness comparison between the dataset and model, available in Table 3.17 computed within the 3-5 mm probe displacement range, revealed a model stiffness of 3.805 N/mm and a dataset stiffness of 3.711 N/mm, with a difference of only 2.54%. The interpolation R-value for the dataset was 99.38%, while the model achieved 94.86%, extending the high correlation in stiffness response to the complete TAVI assembly model.

Table 3.17. Results overview of the indentation test simulation (Validation 3), used to validate the complete TAVI assembly at the end of the scaffold insertion simulation. The table includes stiffness values, correlation coefficient, percentage error, and NRMSE for compression and release phases.

k_{Indent}^{Data} [N/mm]	Data St.D.	k_{Indent}^{Model} [N/mm]	$R_{Model}^{\%}$	$E_k^{\%}$	Compress. NRMSE [%]	Release NRMSE [%]
0.3058	0.022	0.3805	94.87	24.43	25.59	349.88

To further assess the predictive accuracy, both the experimental and simulation results were re-sampled over the -0.036 to 7.5 mm probe displacement range, and the NRMSE was evaluated. The interpolation R-values degraded, showing 89.91% for dataset indentation, 53.85% for dataset release, 87.33% for model indentation, and 60.64% for model release, with NRMSE reaching 25.59% overall and an extreme 349.88% for the release phase.

The large discrepancy in the NRMSE observed in the release phase is likely caused by an erroneous initial positioning of the indenter probe in the simulation. This misalignment affects the interpolation of the force-displacement data at the upper extreme of the probe displacement range, leading to an unreliable error estimation. The same issue also influences the indentation phase but with a lower impact, as extreme nonlinear deformations due to self-contact have yet to occur in either the specimens and the model.

Nevertheless, the good quantitative agreement observed between the experimental and model-derived strain-stress curves, along with the absence of strong nonlinear deformations within the COU of the model, ensures that this discrepancy does not compromise the validity of the results obtained in the transvalvular simulation. This conclusion is further supported by the findings of Bailey *et al.* [10].

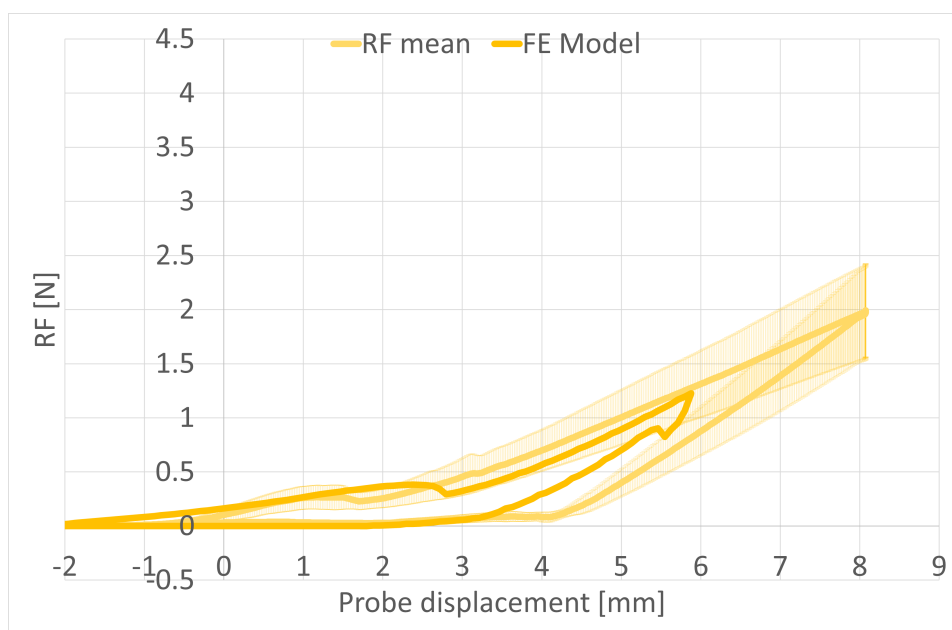


Figure 3.21. Comparison between the mean reaction force - displacement curve found for the Indentation test (with relative standard deviation) and the curve obtained via FE simulation, as part of the validation process of the complete TAVI model.

Examining the RF vs. probe displacement curve in Figure 3.21, a notable discrepancy of approximately 0.8 N is observed in the maximum RF estimation, indicating the presence of highly nonlinear behaviors. A portion of this variability is likely due to complex contact interactions and stress redis-

tribution at the assembly level, where multiple interconnected parts introduce additional degrees of uncertainty. Furthermore, the experimental dataset itself exhibits significant inter-sample variability, with stiffness deviations reaching 30%, as reported in Section 3.1.3. This suggests limitations in the experimental protocol followed, reinforcing the need for independent validation of the leaflet model alone to isolate its mechanical response from assembly-level interactions.

Table 3.18. Overview of R-values from resampling in the indentation test, comparing correlation coefficients between experimental data and the FE model during indentation and release phases.

Phase	$R_{Data}^{\%}$	$R_{Model}^{\%}$
Indentation	89.90	87.33
Release	53.85	60.64

This observation is further supported by the presence of several discontinuities at the extremes of the probe displacement range, visible in Figure 3.21. These inconsistencies likely indicate limitations in the fastening mechanism, the 'Bridge' part shown in Figure 2.7a reducing the overall reliability of the test.

Despite these complexities, it is important to highlight the presence and correct correspondence of the localized peak between 2.5 and 3 mm of the indenter probe displacement range, where the internal folding of the leaflet occurs. The accurate representation of this localized mechanical feature confirms the model's ability to replicate critical structural behaviors. Given the strong agreement in k_{Radial}^{TAVI} and the overall mechanical response between the experimental TAVI sample and the simulation results, the complete TAVI valve assembly model is considered fully validated and reliable within the COU of this research, allowing for the next research phase.

3.4. TRANSVALVULAR PRESSURE SIMULATION RESULTS

The transvalvular pressure simulation was conducted to assess the impact of NiTiNol material parameters on the mechanical response of the complete TAVI valve assembly. The nominal NiTiNol parameters values obtained via Monte Carlo parameter fitting study were compared with 10 simulation runs, in which the material parameters were varied within the 5.34% NRMSE range obtained from MC analysis (see Table B.20). Additionally, an expanded hypothesis exploration range, derived from literature data [22], was tested in 10 further runs.

The sensed reaction forces at the stent and the radial coordinates of both the external top node of the leaflet model and the internal node at the stent tip were monitored and compared with the nominal case, computing NRMSE values. The structural stiffness k_{Struct} was evaluated over the 12.5–10.57 mm range of the stent tip r-coordinate, assessing deviations introduced by parameter variations. The complete stiffness k_{Struct} , radial coordinates and NRMSE results are summarized in Table 3.19.

The analysis indicates that transformation parameters exert minimal influence under the loading conditions analysed as part of this study, implying that the valve assembly remains predominantly in the austenitic phase, without significant phase transformation activation. This observation supports the conclusion that within this physiological range, this model of TAVI valve operates primarily in the austenitic phase, with minimal martensitic transformation occurring in localized regions.

As shown in Figure 3.22a, the influence of E_A^{NiTi} on k_{Struct} exhibits a nearly linear trend at the lower bound of its range. However, as E_A^{NiTi} increases, a larger portion of the NiTiNol stent structure undergoes stress-induced transformation, leading to a saturation effect where further increases in stresses no longer correlate linearly with the imposed strains. This nonlinearity emerges because, at higher E_A^{NiTi} values, the available austenitic strain range upper bound is reduced, meaning that further variations in the stiffness no longer directly correlate with imposed strains. Instead, σ_{tL}^S and

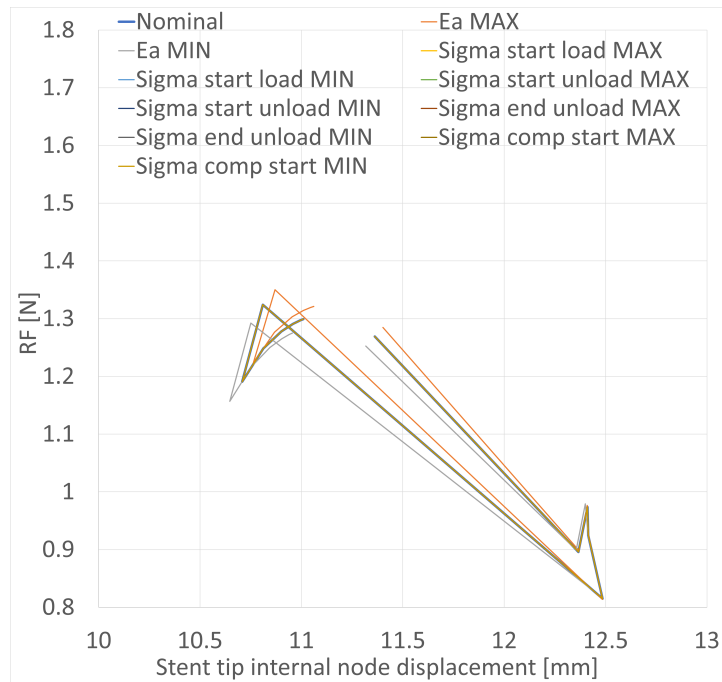
Table 3.19. Overview of results from the transvalvular pressure simulations, including estimation errors for minimal and maximal cases analyzed in the Sensitivity Analysis and Hypothesis Exploration studies.

Param	k_{Struct}^{Min} [MPa]	$E_{k_{Struct}}^{%Min}$	k_{Struct}^{Max} [MPa]	$E_{k_{Struct}}^{%Max}$	$\Delta RF_{Min}^{%}$	$\Delta RF_{Max}^{%}$	r_{coord}^{Min}	r_{coord}^{Max}
Sensitivity analysis								
E_A^{NiTi}	0.2402	-4.45	0.2621	4.27	1.96	1.76	0.35	0.45
σ_{tL}^S	0.2514	0.00	0.2514	0.00	0.00	0.00004	0.00001	0.00005
σ_{tU}^S	0.2514	0.00	0.2514	0.00	0.00003	0.00	0.00001	0.00001
σ_{tU}^E	0.2514	0.00	0.2514	0.00	0.00003	0.00	0.00001	0.00002
σ_{cL}^S	0.2514	0.00	0.2514	0.00	0.00	0.00	0.00001	0.00001
Hypothesis exploration								
E_A^{NiTi}	0.1677	-33.30	0.3302	31.36	12.44	10.60	1.90	2.32
σ_{tL}^S	0.2512	-0.07	0.2514	0.00	0.02	0.00	0.00047	0.00001
σ_{tU}^S	0.2514	0.00	0.2514	0.00	0.00	0.00	0.00001	0.00001
σ_{tU}^E	0.2514	0.00	0.2514	0.00	0.00	0.00	0.00001	0.00004
σ_{cL}^S	0.2514	0.00	0.2514	0.00	0.00	0.00003	0.00002	0.00001

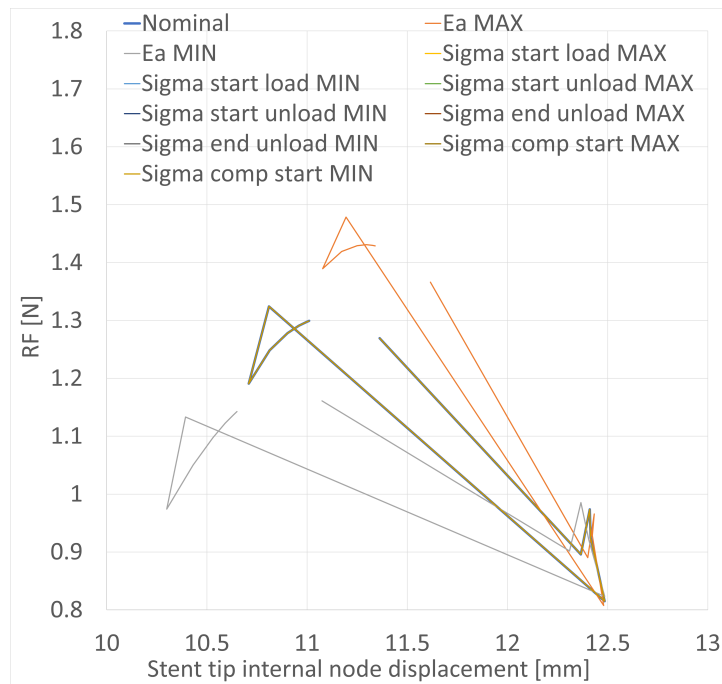
other transformation parameters begin to dominate the material response, limiting the influence of E_A^{NiTi} on k_{Struct} estimation error. The initial manifestation of this phenomenon is present in Table 3.19, where higher values of E_A^{NiTi} analysed as part of the hypothesis exploration research start to produce an estimation error less linearly correlated than the one found in the sensitivity analysis research.

In fact, given that a higher E_A^{NiTi} reduces the strain range available before the transformation, for higher E_A^{NiTi} values a larger portion of the NiTiNol stent structure undergoes phase transformation, amplifying the role of σ_{tL}^S and other phase transformation parameters in the material response and, as such, limiting the linearity between the E_A^{NiTi} upper bound value and the found k_{Struct} prediction error. This effect is also reflected in the higher prediction error observed in RF tracking and the leaflet external node r-coordinate in the hypothesis exploration case compared to the sensitivity analysis case when analyzing the influence of σ_{tL}^S . The explicit clinical implication of these findings is profound: validated NiTiNol parameters substantially reduce the predictive uncertainty of FE models, directly translating into safer, more predictable TAVI deployments in clinical practice.

The remaining three tested parameters demonstrated negligible influence on the simulation results, reinforcing the observation that no deep phase transformations occur for the given stent deformations. Additionally, the analysis highlights the dominant role of k_{Crush} in governing the overall mechanical response of the structure. While being evaluated based on stent tip displacement and sensed reaction forces, the computed structural stiffness aligns closely with the stiffness values found for both the Crush resistance test simulation and Indentation test simulation, as reported in Table 3.16. This observation suggests that the stent structure acts as main contribution to the overall stiffness of the assembly, with the leaflets being a neglectable load-bearing components. This finding aligns well with the previous literature, in particular *Bailey et al.* [10], which shows how the leaflets model results neglectable under certain simulation conditions.



(a)



(b)

Figure 3.22. Reaction forces - displacement curve evaluated at the tip of the stent model. Figure 3.22a shows the obtained curves for the Sensitivity analysis exploration, in which the NiTiNol parameters have been varied within the 5.24% NRMSE range derived from the MC study. Figure 3.22b shows the results of the broader NiTiNol parameters space explored as part of the Hypothesis exploration analysis.

4

RESULTS DISCUSSION

4.1. FINDINGS AND IMPLICATIONS FOR THE PREDICTIVE ACCURACY OF TAVI FE MODELING

A fully verified and validated FE model of a TAVI valve was developed to assess how variations in shape-memory alloy parameters influence the mechanical response of the FE model and the reliability of the simulation results. Ensuring that the baseline model was independent of physical assumptions, numerical solver choices, and discretization errors allowed the sensitivity analysis to focus exclusively on material parameter variability, minimizing the influence of external factors. The bottom-up validation approach, following ASME guidelines [20], ensured that each step in the model development process was reliable before increasing complexity, effectively reducing error propagation throughout the workflow. The validation framework encompassed experimental validation to confirm the model's ability to reproduce physical behavior, discretization error analysis to verify numerical stability, and numerical solver error verification to demonstrate that the results were independent of solver-specific settings.

With a high-confidence computational framework established, key NiTiNol material parameters presented in Table B.20 were varied within two defined ranges. The sensitivity analysis range, based on the 5.34% NRMSE Monte Carlo parameter fitting, ensured that parameter variations remained within experimental uncertainty, while the hypothesis exploration range, derived from literature-based values, examined how *non-case-specific* parameters influence model predictions. The results demonstrated that applying generic material parameters rather than case-specific ones can significantly alter FE simulation outcomes, potentially making them unreliable and non-representative of the actual system. As shown in Figure 3.22, progressive deviations in the validated material parameters induce a progressive degradation of the FE model estimation abilities, especially on the evaluated k_{Struct} and of the reaction forces, as well as the geometrical configuration of the valve under the same, consistent load. This highlights that material parameter selection directly impacts the mechanical response of the simulation, reinforcing the idea that averaged literature values are not directly applicable to complex, case-specific simulations. The necessity of integrating experimental validation with numerical modeling is therefore emphasized to ensure meaningful results. Explicitly linking these findings directly to clinical practice, it becomes clear that rigorous NiTiNol parameter validation significantly reduces uncertainty, directly supporting safer clinical decision-making processes.

While this study focused primarily on the linear elastic region relative to the austenitic phase of the NiTiNol stress-strain curve, the mechanical properties of the TAVI assembly demonstrated up to 33.3% variability in the ranges extrapolated from the available literature and analysed as part of the Hypothesis exploration analysis (Table 3.19), underscoring the significance of precise material characterization. Notably, the largest deviations were observed in k_{Struct} and sensed RF, reinforcing that even within physiological loading and in absence of severe phase transformation, the NiTiNol parameter assumptions introduce measurable differences. The comparison between the sensitivity analysis range and hypothesis exploration range, illustrated in Figure 3.22b, confirms that parameter deviations induce nontrivial variations in mechanical response. These findings reinforce that applying averaged literature-based NiTiNol parameters significantly compromises the reliability of FE simulations. In a clinical context, reliance on such parameters could lead to imprecise predictions of device performance during patient-specific implantation, potentially affecting patient safety. Furthermore, as regulatory bodies increasingly accept computational models, the use of non-case-specific parameters could hinder regulatory approvals due to increased uncertainty and reduced credibility.

In common scientific practice, the degree to which material parameter assumptions may influence FE modeling is highly application-dependent. In cases where deformation remains within the austenitic phase, as in this study, minor inaccuracies may be acceptable. However, in applications involving severe phase transformations, such as valve crimping or patient-specific implanta-

tion procedures, accurate material characterization becomes essential. This effect is expected to be even more pronounced in cases involving high strain cycling or extreme geometrical conformation changes, such as crimping onto a catheter for delivery. In these scenarios, phase transformation dynamics play a dominant role, as demonstrated by the strong dependence of E_A^{NiTi} variations on stiffness results in Figure 3.22a.

A further example of the degree to which a FE model desired credibility is highly dependant from the intended application is represented by the COU of the model itself. In the early-stage prototyping of a TAVI valve, minor inaccuracies in material behavior may be acceptable. However, in application such as surgical planning, device optimization, or regulatory approval, the credibility of the material characterization becomes critical. Failing to experimentally validate NiTiNol material properties risks degrading the predictive accuracy of FE simulations, potentially invalidating them as a tool for real-world decision-making, as demonstrated within this study. No matter how refined, a computational model without high-fidelity material characterization risks producing misleading predictions. In high-stakes applications such as surgical planning and device optimization, unreliable assumptions can propagate errors that compromise patient safety and regulatory compliance. Ensuring model credibility requires rigorous verification, validation, and uncertainty quantification in line with the latest ASME standards, reinforcing that FE simulation credibility demands more than numerical accuracy.

The observed variability underscores critical clinical implications, especially regarding patient safety and clinical decision-making. Employing non-case-specific material parameters can potentially lead to incorrect predictions of valve behavior during patient-specific deployment scenarios, increasing the risk of procedural complications. From a regulatory perspective, this uncertainty could delay approvals, emphasizing that rigorous experimental validation of FE models should become standard practice for medical device certification. Explicitly connecting these computational findings to clinical outcomes, it becomes clear that rigorously validated, patient-specific NiTiNol parameters significantly enhance the safety and efficacy of TAVI procedures by substantially reducing uncertainty in predictive FE modeling. Additionally, the Monte Carlo-based parameter fitting approach explicitly developed here provides improved uncertainty quantification, representing a clear methodological advancement over standard fitting methods typically reported in the literature. Consequently, compared explicitly to established FE models, this computational framework demonstrates superior predictive reliability, directly enhancing regulatory acceptance by offering robust, credible, and quantitatively validated outcomes.

4.2. KNOWN LIMITATIONS AND FUTURE DEVELOPMENTS

One of the key limitations of this study is the absence of an independent uniaxial compression dataset for NiTiNol, restricting the direct calibration of σ_{cL}^S through experimental parameter fitting. Without such a dataset, the Monte Carlo fitting procedure could not be applied to compressive stress states, reducing confidence in the predictive accuracy of simulations involving compressive loading. To mitigate this limitation, the nominal value of σ_{cL}^S was estimated from available literature and subsequently varied within the 5.34% Monte Carlo fitting range and the broader hypothesis exploration range, as summarized in Table 3.19. Although necessary, this approach introduces uncertainty in the observed deviations between the nominal case and the hypothesis exploration-sensitivity analysis cases, as the actual influence of σ_{cL}^S remains virtually unverified. A key refinement for future research is the inclusion of an experimental dataset enabling direct Monte Carlo fitting of σ_{cL}^S and other compression-related parameters. Without this data, material calibration remains incomplete, limiting the confidence in simulations that involve compressive stress states.

Addressing this limitation through the explicit integration of experimental compression data into the Monte Carlo parameter-fitting framework would greatly enhance the scientific rigor and credibility of the FE model. This step would substantially strengthen predictive confidence by providing

more comprehensive validation coverage, actively reducing uncertainties related to compressive deformation scenarios encountered clinically.

Another key limitation concerns the selected loading conditions. While the simulated scenario was intentionally designed to be independent of case-specific anatomical factors and aligns with well-documented nominal loading conditions in the literature, it did not induce a significant phase transformation in the NiTiNol alloy. As illustrated in Figure 3.22, parameter influence was most noticeable in stiffness deviations, whereas transformation-related effects were negligible. Consequently, the full influence of phase transformation parameters could not be assessed within the simulated physiological range, as no significant transformation was observed. However, these parameters are expected to become highly influential in high-strain scenarios, such as valve crimping for catheter delivery or post-deployment interactions with patient-specific anatomical structures. To address this, future research should incorporate simulation conditions that induce severe phase transformations, enabling a more comprehensive assessment of the impact of transformation-related parameters on simulation accuracy.

An additional limitation concerns the geometric discrepancies between the nominal model values and the TAVI prototypes used for experimental validation. The tested prototypes exhibited slight deviations from the original valve blueprint, which likely influenced experimental activities, such as the radial compression test and the crush resistance test. While the impact of this geometrical incongruence was not analyzed in detail, it is expected to have played a role in the observed deviations between experimental and simulation results during the model validation process. The differences between nominal and experimental geometries, particularly at the leaflet-stent interface, introduce uncertainties in validation steps that rely on direct comparisons between measured and simulated mechanical responses. Future studies should quantify this influence and refine the geometric agreement between simulated and experimental models to enhance model credibility.

Resolving these limitations, particularly the absence of experimental compression data, would notably enhance the real-world applicability of FE models, especially under conditions involving severe deformation, such as valve crimping or interactions with patient-specific anatomy. By filling this critical gap, future studies can significantly improve predictive accuracy, benefiting patient-specific clinical planning and device optimization processes and facilitating smoother regulatory acceptance.

Despite these limitations, this study successfully demonstrates the critical impact of material parameter selection on FE model reliability, serving as a proof of concept that applying NiTiNol properties from literature without case-specific validation can lead to unreliable simulation outcomes. Future research should prioritize expanding experimental datasets for compression calibration, enabling a more comprehensive Monte Carlo parameter fitting for compressive loading conditions. Additionally, incorporating simulation scenarios that induce significant phase transformation will provide further insights into its impact on model accuracy, particularly in high-strain conditions such as crimping and post-deployment interactions. Finally, refining the geometric agreement between simulated and experimental models, especially at the stent-leaflet interface, will ensure a more precise correspondence between numerical and physical testing results. Addressing these challenges will enhance the credibility and predictive accuracy of FE modeling in TAVI simulations, reinforcing the necessity of integrating experimental validation with computational studies. Future work should explicitly build on the creativity demonstrated in the Python-driven parametric exploration methodology developed in this study, further extending it to real-time adaptive FE modeling for patient-specific scenarios. By combining these advancements, future research can significantly enhance the reliability and accuracy of FE simulations, ensuring their applicability in clinical and engineering contexts.

5

CONCLUSIONS

5.1. CONCLUSIONS

This study investigated the influence of shape-memory alloy parameter variations on the predictive accuracy and reliability of finite element modeling for transcatheter aortic valve Implantation devices. A fully verified and validated FE model was developed using a bottom-up approach, ensuring that numerical solver settings, discretization choices, and design assumptions did not influence the analysis. Model validation against experimental tests demonstrated strong agreement in mechanical response, with deviations primarily occurring under extreme deformation conditions. Explicitly compared to other FE models in literature, this study presents a model with substantially reduced uncertainty, significantly enhancing regulatory acceptance and TAVI FE modeling techniques due to the credibility and rigor explicitly demonstrated throughout the validation process.

The sensitivity analysis revealed that NiTiNol transformation parameters exhibited minimal influence under the tested physiological loading conditions, except for Austenite Young's modulus (E_A), which displayed a linear correlation with the deviation in the model predictive ability. The role of σ_{tS}^L became more pronounced in higher E_A cases, where an increased fraction of the stent underwent phase transformation due to the strain-controlled nature of the system. Other material parameters had negligible influence, reinforcing that deep phase transformations were not prevalent in this specific loading scenario.

The findings emphasize that generic material properties from literature are inadequate for complex, case-dependent simulations. While experimentally fitted material parameters ensured high reliability, the use of non-case-specific values introduced up to 30% variability in the mechanical response of the simulation. This reinforces the necessity of case-specific material validation, particularly for applications involving severe phase transformations, such as valve crimping or interactions with patient-specific anatomical structures.

Despite limitations, such as the absence of experimental compression data for σ_{tS}^L calibration and the exclusion of high-strain loading scenarios, the findings presented here offer a solid foundation for future research. The findings highlight the importance of integrating verification, validation, and uncertainty quantification (VVUQ) activities in biomedical FE simulations, reinforcing that credible modeling requires more than numerical accuracy. Instead, rigorous experimental validation remains essential to ensure that FE simulations are applicable in clinical and engineering contexts. The results highlight the critical importance of rigorous, experimentally validated, case-specific NiTiNol parameter characterization to ensure reliable FE predictions. In clinical terms, adopting such validated FE models can substantially improve the safety and efficacy of TAVI valve implants by accurately predicting structural and functional performance under patient-specific conditions. Additionally, from an industrial and regulatory perspective, ensuring the credibility of FE simulations through case-specific parameter validation will streamline regulatory acceptance, reducing uncertainties in regulatory submissions and expediting the pathway from design to patient deployment.

The insights gained from this research directly translate into improved patient safety by enhancing the accuracy of device deployment predictions. Furthermore, establishing validated material properties as standard practice will streamline regulatory processes, reducing uncertainties and accelerating the pathway from innovative device design to clinical implementation. By emphasizing the necessity of case-specific material validation, this study contributes to the ongoing evolution of FE modeling practices in the medical device industry, reinforcing the importance of integrating experimental validation with computational studies to ensure reliable and accurate predictions.

BIBLIOGRAPHY

- [1] S. Coffey, B. Cox, and M. J. Williams. “The Prevalence, Incidence, Progression, and Risks of Aortic Valve Sclerosis: A Systematic Review and Meta-Analysis”. In: *Journal of the American College of Cardiology* 63 (25 PART A July 2014), pp. 2852–2861. ISSN: 15583597. DOI: [10.1016/j.jacc.2014.04.018](https://doi.org/10.1016/j.jacc.2014.04.018). pmid: 24814496.
- [2] M. Lindroos, M. Kupari, J. Heikkilii, and H. Finland. *Prevalence of Aortic Valve Abnormalities in the Elderly: An Echocardiographic Study of a Random Population Sample*.
- [3] M. W. A. Chu, M. A. Borger, F. W. Mohr, and T. Walther. “Transcatheter Heart-Valve Replacement: Update”. In: *Canadian Medical Association Journal* 182.8 (May 18, 2010), pp. 791–795. ISSN: 0820-3946, 1488-2329. DOI: [10.1503/cmaj.080064](https://doi.org/10.1503/cmaj.080064). URL: <http://www.cmaj.ca/cgi/doi/10.1503/cmaj.080064> (visited on 04/22/2024).
- [4] G. M. Bosi, C. Capelli, M. H. Cheang, N. Delahunty, M. Mullen, A. M. Taylor, and S. Schievano. “A Validated Computational Framework to Predict Outcomes in TAVI”. In: *Scientific Reports* 10.1 (Dec. 2020). ISSN: 20452322. DOI: [10.1038/s41598-020-66899-6](https://doi.org/10.1038/s41598-020-66899-6). pmid: 32555300.
- [5] A. Kheradvar, E. M. Groves, C. J. Goergen, S. H. Alavi, R. Tranquillo, C. A. Simmons, L. P. Dasi, K. J. Grande-Allen, M. R. Mofrad, A. Falahatpisheh, B. Griffith, F. Baaijens, S. H. Little, and S. Canic. *Emerging Trends in Heart Valve Engineering: Part II. Novel and Standard Technologies for Aortic Valve Replacement*. Kluwer Academic Publishers, Apr. 2015. DOI: [10.1007/s10439-014-1191-5](https://doi.org/10.1007/s10439-014-1191-5). pmid: 25449148.
- [6] T. Duerig. “The Metallurgy of Nitinol as It Pertains to Medical Devices”. In: *Titanium in Medical and Dental Applications*. Elsevier, 2018, pp. 555–570. ISBN: 978-0-12-812456-7. DOI: [10.1016/B978-0-12-812456-7.00025-1](https://doi.org/10.1016/B978-0-12-812456-7.00025-1). URL: <https://linkinghub.elsevier.com/retrieve/pii/B9780128124567000251> (visited on 05/18/2024).
- [7] F. Auricchio and R. L. Taylor. “Shape-Memory Alloys: Modelling and Numerical Simulations of the Finite-Strain Superelastic Behavior”. In: *Computer Methods in Applied Mechanics and Engineering* 143.1-2 (Apr. 1997), pp. 175–194. ISSN: 00457825. DOI: [10.1016/S0045-7825\(96\)01147-4](https://doi.org/10.1016/S0045-7825(96)01147-4). URL: <https://linkinghub.elsevier.com/retrieve/pii/S0045782596011474> (visited on 04/22/2024).
- [8] F. Auricchio, M. Conti, S. Morganti, and A. Reali. “Simulation of Transcatheter Aortic Valve Implantation: A Patient-Specific Finite Element Approach”. In: *Computer Methods in Biomechanics and Biomedical Engineering* 17.12 (2014), pp. 1347–1357. ISSN: 14768259. DOI: [10.1080/10255842.2012.746676](https://doi.org/10.1080/10255842.2012.746676). pmid: 23402555.
- [9] F. Auricchio, M. Conti, A. Ferrara, S. Morganti, and A. Reali. “Patient-Specific Simulation of a Stentless Aortic Valve Implant: The Impact of Fibres on Leaflet Performance”. In: *Computer Methods in Biomechanics and Biomedical Engineering* 17.3 (Feb. 2014), pp. 277–285. ISSN: 10255842. DOI: [10.1080/10255842.2012.681645](https://doi.org/10.1080/10255842.2012.681645). pmid: 22553900.
- [10] J. Bailey, N. Curzen, and N. W. Bressloff. “Assessing the Impact of Including Leaflets in the Simulation of TAVI Deployment into a Patient-Specific Aortic Root”. In: *Computer Methods in Biomechanics and Biomedical Engineering* 19.7 (May 2016), pp. 733–744. ISSN: 14768259. DOI: [10.1080/10255842.2015.1058928](https://doi.org/10.1080/10255842.2015.1058928). pmid: 26194804.

- [11] M. Bianchi, G. Marom, R. P. Ghosh, H. A. Fernandez, J. R. Taylor, M. J. Slepian, and D. Bluestein. “Effect of Balloon-Expandable Transcatheter Aortic Valve Replacement Positioning: A Patient-Specific Numerical Model”. In: *Artificial Organs* 40.12 (Dec. 2016), E292–E304. ISSN: 15251594. DOI: [10.1111/aor.12806](https://doi.org/10.1111/aor.12806). pmid: [27911025](https://pubmed.ncbi.nlm.nih.gov/27911025/).
- [12] G. M. Bosi, C. Capelli, S. Khambadkone, A. M. Taylor, and S. Schievano. “Patient-Specific Finite Element Models to Support Clinical Decisions: A Lesson Learnt from a Case Study of Percutaneous Pulmonary Valve Implantation”. In: *Catheterization and Cardiovascular Interventions* 86.6 (2015), pp. 1120–1130. ISSN: 1522-726X. DOI: [10.1002/ccd.25944](https://doi.org/10.1002/ccd.25944). URL: <https://onlinelibrary.wiley.com/doi/abs/10.1002/ccd.25944> (visited on 04/24/2024).
- [13] C. Capelli, G. M. Bosi, E. Cerri, J. Nordmeyer, T. Odenwald, P. Bonhoeffer, F. Migliavacca, A. M. Taylor, and S. Schievano. “Patient-Specific Simulations of Transcatheter Aortic Valve Stent Implantation”. In: *Medical and Biological Engineering and Computing* 50.2 (Feb. 2012), pp. 183–192. ISSN: 01400118. DOI: [10.1007/s11517-012-0864-1](https://doi.org/10.1007/s11517-012-0864-1). pmid: [22286953](https://pubmed.ncbi.nlm.nih.gov/22286953/).
- [14] D. Carbonaro, D. Gallo, U. Morbiducci, A. Audenino, and C. Chiastra. “In Silico Biomechanical Design of the Metal Frame of Transcatheter Aortic Valves: Multi-Objective Shape and Cross-Sectional Size Optimization”. In: *Structural and Multidisciplinary Optimization* 64.4 (Oct. 2021), pp. 1825–1842. ISSN: 1615-147X, 1615-1488. DOI: [10.1007/s00158-021-02944-w](https://doi.org/10.1007/s00158-021-02944-w). URL: <https://link.springer.com/10.1007/s00158-021-02944-w> (visited on 05/08/2024).
- [15] A. Finotello, R. Gorla, N. Brambilla, F. Bedogni, F. Auricchio, and S. Morganti. “Finite Element Analysis of Transcatheter Aortic Valve Implantation: Insights on the Modelling of Self-Expandable Devices”. In: *Journal of the Mechanical Behavior of Biomedical Materials* 123 (Nov. 2021). ISSN: 18780180. DOI: [10.1016/j.jmbbm.2021.104772](https://doi.org/10.1016/j.jmbbm.2021.104772). pmid: [34481297](https://pubmed.ncbi.nlm.nih.gov/34481297/).
- [16] G. Luraghi, W. Wu, F. D. Gaetano, J. F. R. Matas, G. D. Moggridge, M. Serrani, J. Stasiak, M. L. Costantino, and F. Migliavacca. “Evaluation of an Aortic Valve Prosthesis: Fluid-structure Interaction or Structural Simulation?” In: *Journal of Biomechanics* 58 (June 2017), pp. 45–51. ISSN: 18732380. DOI: [10.1016/j.jbiomech.2017.04.004](https://doi.org/10.1016/j.jbiomech.2017.04.004). pmid: [28454910](https://pubmed.ncbi.nlm.nih.gov/28454910/).
- [17] E. A. Ovcharenko, K. U. Klyshnikov, A. E. Yuzhalin, G. V. Savrasov, A. N. Kokov, A. V. Batranin, V. I. Ganyukov, and Y. A. Kudryavtseva. “Modeling of Transcatheter Aortic Valve Replacement: Patient Specific vs General Approaches Based on Finite Element Analysis”. In: *Computers in Biology and Medicine* 69 (Feb. 2016), pp. 29–36. ISSN: 18790534. DOI: [10.1016/j.combiomed.2015.12.001](https://doi.org/10.1016/j.combiomed.2015.12.001). pmid: [26708469](https://pubmed.ncbi.nlm.nih.gov/26708469/).
- [18] W. Wu, D. Pott, B. Mazza, T. Sironi, E. Dordoni, C. Chiastra, L. Petrini, G. Pennati, G. Dubini, U. Steinseifer, S. Sonntag, M. Kuetting, and F. Migliavacca. “Fluid-Structure Interaction Model of a Percutaneous Aortic Valve: Comparison with an in Vitro Test and Feasibility Study in a Patient-Specific Case”. In: *Annals of Biomedical Engineering* 44.2 (Feb. 2016), pp. 590–603. ISSN: 15739686. DOI: [10.1007/s10439-015-1429-x](https://doi.org/10.1007/s10439-015-1429-x). pmid: [26294009](https://pubmed.ncbi.nlm.nih.gov/26294009/).
- [19] O. Faris and J. Shuren. “An FDA Viewpoint on Unique Considerations for Medical-Device Clinical Trials”. In: *New England Journal of Medicine* 376.14 (Apr. 6, 2017). Ed. by J. M. Drazen, D. P. Harrington, J. J. McMurray, J. H. Ware, and J. Woodcock, pp. 1350–1357. ISSN: 0028-4793, 1533-4406. DOI: [10.1056/NEJMr1512592](https://doi.org/10.1056/NEJMr1512592). URL: <http://www.nejm.org/doi/10.1056/NEJMr1512592> (visited on 04/09/2024).
- [20] Asme. *ASME V&V 40-2018*. 2018. URL: <http://go.asme.org/InterpsDatabase..>
- [21] *Cardiovascular Implants-Cardiac Valve Prostheses-Part 3: Heart Valve Substitutes Implanted by Transcatheter Techniques Implants Cardiovasculaires-Prothèses Valvulaires-Partie 3: Valves Cardiaques de Substitution Implantées Par Des Techniques Transcathéter ISO 5840-3:2021(E) li COPYRIGHT PROTECTED DOCUMENT Published in Switzerland*. 2021.

- [22] D. Carbonaro, S. Zambon, A. Corti, D. Gallo, U. Morbiducci, A. L. Audenino, and C. Chias-tra. “Impact of Nickel–Titanium Super-Elastic Material Properties on the Mechanical Performance of Self-Expandable Transcatheter Aortic Valves”. In: *Journal of the Mechanical Behavior of Biomedical Materials* 138 (Feb. 1, 2023), p. 105623. ISSN: 1751-6161. DOI: [10.1016/j.jmbbm.2022.105623](https://doi.org/10.1016/j.jmbbm.2022.105623). URL: <https://www.sciencedirect.com/science/article/pii/S1751616122005288> (visited on 04/05/2024).
- [23] Microsoft Corporation. *Microsoft Excel*. Spreadsheet software. 2024. URL: <https://www.microsoft.com/en-us/microsoft-365/excel>.
- [24] *Cardiovascular Implants-Cardiac Valve Prostheses-Part 3: Heart Valve Substitutes Implanted by Transcatheter Techniques Implants Cardiovasculaires-Prothèses Valvulaires-Partie 3: Valves Cardiaques de Substitution Implantées Par Des Techniques Transcathéter ISO 5840-3:2021(E) Ii COPYRIGHT PROTECTED DOCUMENT Published in Switzerland*. 2021.
- [25] “Testing Methods for Solid Friction”. In: *Mechanical Testing and Evaluation*. Ed. by H. Kuhn and D. Medlin. ASM International, 2000, pp. 306–316. ISBN: 978-1-62708-176-4. DOI: [10.31399/asm.hb.v08.a0003281](https://doi.org/10.31399/asm.hb.v08.a0003281). URL: <https://dl.asminternational.org/books/book/47/chapter/533100/testing-methods-for-solid-friction> (visited on 05/31/2024).
- [26] D. Brown. *Tracker*. Open Source Physics. 2024. URL: <https://physlets.org/tracker/>.
- [27] P. S. Foundation. *Python 2.7*. Scripting Language. 2022. URL: <https://www.python.org/>.
- [28] D. Systèmes. *Abaqus 2021.HF3*. Finite Element Analysis Software. Vélizy-Villacoublay, France, 2021.
- [29] *Cardiovascular Implants-Cardiac Valve Prostheses-Part 1: General Requirements Implants Cardiovasculaires-Prothèses Valvulaires-Partie 1: Exigences Générales COPYRIGHT PROTECTED DOCUMENT Published in Switzerland*. 2021.
- [30] D. Systèmes. *SolidWorks 2023*. Computer-Aided Design (CAD) Software. Vélizy-Villacoublay, France, 2023. URL: <https://www.solidworks.com/>.

A

APPENDIX - EXPERIMENTAL TEST DEVICES

A

A.1. FASTENING DEVICE DESIGN

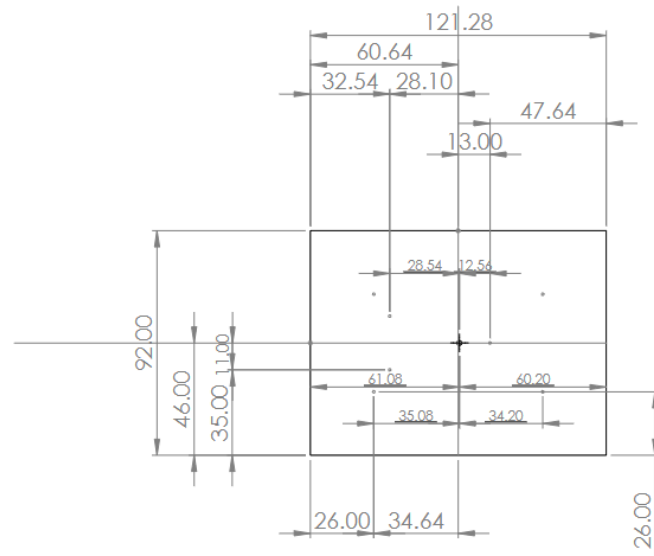


Figure A.1. Aluminum bottom plate, threaded with M6 holes, as designed in SolidWorks as part of this study (SolidWorks 2023, Dassault Systèmes [7]). All distances are in millimeters.

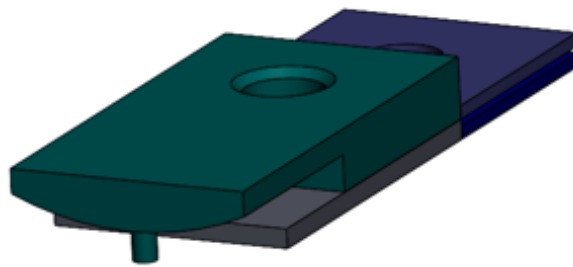


Figure A.2. Bridge CAD model developed in SolidWorks as part of this study (SolidWorks 2023, Dassault Systèmes [30]), shown in an alternative view including 3D-printer raisers (in grey and different blue tonalities), which were later removed from testing.

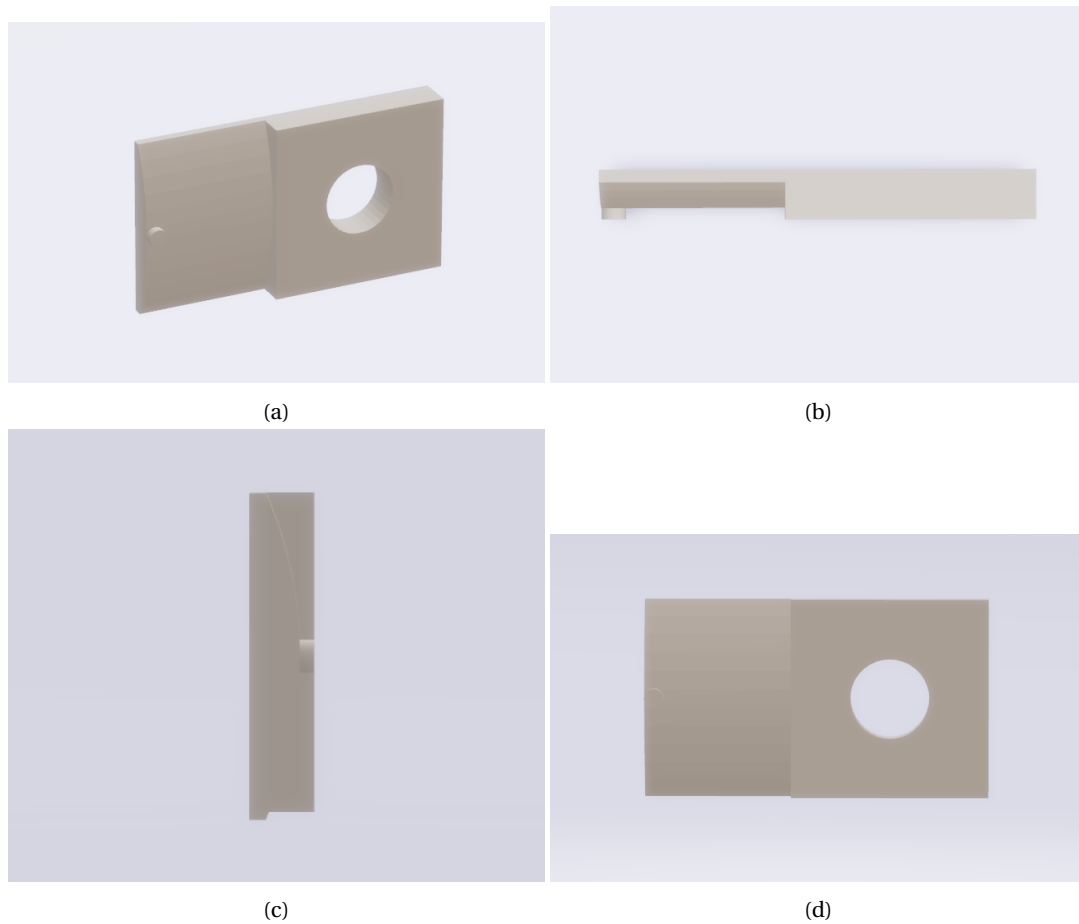


Figure A.3. Developed Bridge CAD model in SolidWorks (SolidWorks 2023, Dassault Systèmes [7]), shown in a tridimensional view (A.3a) along with three orthogonal projections: XZ side view (A.3b), XY side view (A.3c), and YZ side view (A.3d).

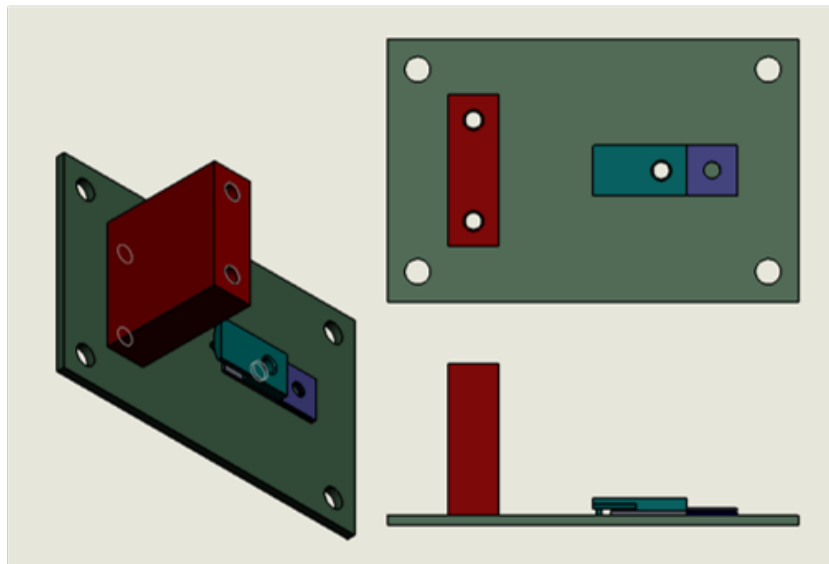


Figure A.4. Complete fastening device assembly developed in SolidWorks as part of this study (SolidWorks 2023, Dassault Systèmes [30]), including the Bridge (light green), the bottom plate (dark green, detailed in Figure A.1), the Holder (red) ensuring half-model symmetry by restricting XY-axis rotation, and the 3D-printed raisers (removed in testing, detailed in Figure A.2).

B

APPENDIX - ADDITIONAL TABLES

B.1. TABLES CHAPTER 2 - MATERIALS AND METHODS

B

Table B.1. Overview of the data implementation flow for the Stent Frame CAE step, outlining the provided inputs and obtained outputs essential for the computational modeling process.

Inputs	Outputs
Provided flat geometry User selected parameters (mesh, materials etc.) Python preprocessing script	Solid model .inp file Analysis parameters

Table B.2. Summary of the data flow in the Stent model shaping simulation, listing the initial solid model, applied analysis parameters, and the final geometrical validation results.

Inputs	Outputs
Solid model .inp file Analysis parameters .inc Analysis definition .inp Python postprocessing script	Metallic stent final geometry Geometrical validation parameters

Table B.3. Data pipeline for the Stent model crimping simulation (Step 3), detailing how the model evolves from its solid state to an analyzed crimped configuration, including extracted reaction forces and radial stiffness.

Inputs	Outputs
Solid model from .odb file (Step 2 results) Analysis definition .inp Python postprocessing script	Metallic stent model crimping response analysis Stent model reaction forces [N] Stent model <i>Flare Diameter (FD)</i> [mm] Stent model <i>radial stiffness</i> [$\frac{N}{mm}$]

Table B.4. Implementation details of the half-symmetry model CAE step (Step 4), used to assess deformation and stent-bridge interactions.

Inputs	Outputs
CAE file Solid model from .odb file (Step 2 results) Python preprocessing script	Deformed assembly .odb (Stent + Bridge)

Table B.5. Data implementation flow for the crush resistance test analysis (Step 5), specifying the extracted forces and stiffness values derived from the model response.

Inputs	Outputs
Solid model .inp file Analysis definition .inp Python postprocessing script	Metallic stent model crush resistance response analysis Stent model reaction forces [N] Stent model <i>FD</i> [mm] Stent model k_{Crush} [$\frac{N}{mm}$]

Table B.6. Steps involved in the complete assembly CAE (Step 6), covering the integration of components into the final computational model.

Inputs	Outputs
CAE file Solid model from .odb file (Step 2 results) Python preprocessing script	Complete assembly model .inp file

Table B.7. Simulation flow for leaflet insertion (Step 7), listing how the complete model is updated post-leaflet integration.

Inputs	Outputs
Complete model .inp file Analysis definition .inp	Complete assembly model .odb file

Table B.8. Data flow for the complete assembly CAE step (Step 8), showing the refinement process leading to a finalized computational model.

Inputs	Outputs
Complete assembly .odb file Python preprocessing script	Complete assembly model .inp file

Table B.9. Overview of the transvalvular simulation (Step 9), including the physiological mechanical response assessment and reaction force extraction.

Inputs	Outputs
Complete assembly model .inp file Analysis definition .inp	TAVI valve physiological mechanical response .odb file Metallic stent ID [mm] Complete assembly sensed reaction force [N] Complete model $k_{Radial} [\frac{N}{mm}]$

Table B.10. Steps in the indentation probe CAE setup (Step 10), detailing the integration of the indenter probe into the computational framework.

Inputs	Outputs
Complete assembly model .odb file Indentation probe CAE Python preprocessing script Analysis definition .inp	Complete assembly and indenter probe model .inp file

Table B.11. Data implementation for the indentation simulation (Step 11), specifying extracted displacement and reaction force parameters.

Inputs	Outputs
Complete assembly .inp file Analysis definition .inp	Complete assembly and indenter probe model .odb file Indenter probe translation [mm] Indenter probe sensed reaction force [N] Complete model $k_{Indent} [\frac{N}{mm}]$

B

Table B.12. Summary of the applied transvalvular pressure loading conditions, with reference to time-dependent parameters in Figure 2.11.

Loading condition	Nominal value
Left ventricular pressure	Time-dependent (Fig. 2.11)
Aortic pressure	Time-dependent (Fig. 2.11)
Cardiac output	5.0 L/min
Heart rate	70 bpm
Stroke volume	71.4 mL
Peak systolic aortic pressure	120 mmHg (~0.16 MPa)

Table B.13. Nominal values and tolerances of the metallic stent and polymeric leaflets geometrical parameters, including relevant post-processing evaluations.

Parameter	Nominal [mm]	Tolerance [mm]	Notes
Metallic stent forming geometric parameters			
Flat geometry base	5.236		
Flat geometry H	35.1		
Pre-radial expansion FD	10.9		
Pre-radial stent ID	10		
Post-radial expansion FD	27.5	±0.5	
Post-radial expansion ID	25	±0.5	
RT	0.45	±0.02	
Post-radial expansion H	31.1	±0.5	
Polymeric leaflets forming geometric parameters			
Leaflets initial base arc	13.09		Eval via script
Leaflets thickness	0.57	±0.02	Mean from sample
Leaflets Z-axis translation	29.7		
Smaller crimper R-transl	6.875		Eval via script

B.2. TABLES CHAPTER 3 - RESULTS

Table B.14. Comprehensive dataset of geometrical measurements for TAVI stents, including flare diameter, internal diameter, height, and radial thickness, along with their standard deviations.

#	M1 [mm]	M2 [mm]	M3 [mm]	Mean [mm]	σ [mm]	$\Delta_{Mean}^{\%}$	Temp. [°C]	RH%
Mean flare diameter FD				26.84	0.11	-2.39%	23.3	53.1%
1	26.74	26.72	26.76	26.74		-2.76%	22.6	55.4%
2	26.80	26.87	26.83	26.83		-2.42%	23.2	53.2%
3	26.87	27.01	26.97	26.95		-2.00%	23.4	52.6%
4	27.05	26.95	26.87	26.96		-1.98%	23.5	52.3%
5	26.66	26.75	26.78	26.73		-2.80%	23.8	51.8%
Mean internal diameter ID				24.91	0.05	-0.35%	23.4	52.6%
1	24.89	24.85	24.83	24.86		-0.57%	23.1	53.6%
2	24.91	24.89	24.85	24.88		-0.47%	23.3	52.9%
3	24.96	24.93	24.93	24.94		-0.24%	23.5	52.4%
4	24.95	25.01	24.97	24.98		-0.09%	23.5	52.4%
5	24.86	24.96	24.88	24.90		-0.40%	23.8	51.7%
Mean stent height H				30.67	0.01	-0.01%	23.2	53.44%
1	30.74	30.71	30.67	30.67		-1.37%	22.8	54.6%
2	31.01	30.65	30.81	30.82		-0.89%	22.8	54.6%
3	30.95	30.67	29.71	30.44		-2.13%	22.8	54.6%
4	30.89	30.51	30.71	30.70		-1.28%	23.6	52.3%
5	30.70	30.76	30.68	30.71		-1.24%	23.8	51.7%
Mean radial thickness RT				0.49	0.01	+9.19%	23.3	52.8%
1	0.50	0.51	0.52	0.51		+13.32%	22.7	54.9%
2	0.48	0.47	0.51	0.49		+8.15%	23.2	53.1%
3	0.49	0.48	0.48	0.48		+7.40%	23.5	52.4%
4	0.48	0.49	0.48	0.48		+7.40%	23.6	52.3%
5	0.50	0.48	0.50	0.49		+9.61%	23.7	51.7%

Table B.15. Complete leaflet thickness measurements dataset for TAVI valves, reporting mean values across multiple samples under controlled conditions.

Sample	M1 [mm]	M2 [mm]	M3 [mm]	Mean [mm]	T [°C]	RH%
1	0.53	0.55	0.58	0.55	23.6	51.9%
2	0.55	0.55	0.54	0.55	23.7	51.7%
3	0.57	0.57	0.58	0.57	23.7	51.7%
4	0.58	0.57	0.56	0.58	23.7	51.8%
5	0.58	0.60	0.61	0.60	23.7	51.5%

B

Table B.16. Full dataset of experimentally obtained static friction coefficients for Aluminium-NiTiNol, including mean values and environmental conditions at the time of measurement.

#	Test	A [m]	B [m]	$\mu_s^{Al-NiTi}$	T [°C]	RH%
S1	1	0.013	0.035	0.354	21.6	41.7%
	2	-	-	-	21.7	41.8%
	3	0.011	0.028	0.412	21.8	41.5%
S1 Mean:				0.383	21.7	41.7%
S2	1	0.009	0.040	0.215	21.7	41.9%
	2	0.009	0.035	0.241	21.8	41.4%
	3	0.009	0.039	0.227	21.9	41.3%
S2 Mean:				0.228	21.8	41.5%
S3	1	0.010	0.036	0.261	22.0	41.3%
	2	0.010	0.039	0.266	22.1	41.3%
	3	0.011	0.029	0.392	22.1	41.3%
S3 Mean:				0.306	22.1	41.3%
S4	1	0.010	0.040	0.250	22.2	41.1%
	2	0.011	0.039	0.270	22.2	40.8%
	3	0.009	0.041	0.212	22.1	40.9%
S4 Mean:				0.244	22.2	40.9%
S5	1	-	-	-	22.2	40.8%
	2	-	-	-	22.2	41.1%
	3	0.009	0.039	0.229	22.2	40.9%
S5 Mean:				0.229	22.2	40.9%
Mean:				0.277	22.0	41.3%

Table B.17. Dataset of static friction coefficients for Leaflet-Indenter interactions, structured similarly to Table B.16 for consistency in experimental evaluation.

#	A [m]	B [m]	$\mu_s^{Llt-Prb}$	T [°C]	RH%
S1	0.023	0.049	0.473	22.2	41.0%
S2	0.027	0.040	0.676	22.2	41.2%
S3	0.027	0.044	0.620	22.2	41.0%
S4	0.026	0.048	0.549	22.1	41.3%
S5	0.026	0.044	0.589	22.1	41.3%
Mean:			0.581	22.2	41.2%

Table B.18. Complete results from the crush resistance test, detailing reaction force values and their statistical distribution.

Sample	Test	$k_{crush}[\frac{N}{mm}]$	$R_{Value}^{\%}$	$\Delta_{k_{crush}}^{\% Mean}$	$NRMSE_{RF}^{\%}$	T [°C]	RH%
S1	1	0.401	99.95	-0.13	9.22	22.2	48.7%
	2	0.398	99.79	-0.84	9.21	22.3	48.4%
	3	0.400	99.80	-0.41	10.06	22.1	48.6%
	4	0.402	99.52	0.13	9.39	21.1	48.5%
	5	0.423	99.95	5.28	10.89	22.0	48.9%
S1 Mean:		0.405		0.74	9.75	21.9	48.6%
S2	1	0.391	99.88	-2.79	16.89	22.0	47.5%
	2	0.415	99.92	3.19	17.35	22.0	46.8%
	3	0.410	99.86	2.09	16.58	22.1	47.0%
	4	0.403	99.81	0.35	18.42	21.9	46.3%
	5	0.395	99.90	-1.74	17.42	21.9	46.6%
S2 Mean:		0.403		0.249	17.33	22.0	46.8%
S3	1	0.387	99.78	-3.79	12.05	22.2	45.1%
	2	0.378	99.87	-6.04	14.21	22.3	45.4%
	3	0.392	99.74	-2.54	9.74	22.3	45.0%
	4	0.376	99.75	-6.51	10.75	22.2	45.1%
	5	0.386	99.44	-3.91	8.84	22.2	45.0%
S3 Mean:		0.383		-4.73	11.12	22.2	45.2%
S4	1	0.414	99.93	3.11	6.73	22.4	44.7%
	2	0.410	99.69	1.93	6.89	22.4	44.4%
	3	0.412	99.87	2.51	8.18	22.4	44.4%
	4	0.397	99.69	-1.07	7.13	22.5	44.2%
	5	0.410	99.66	1.03	7.75	22.3	44.1%
S4 Mean:		0.409		1.74	7.33	22.4	44.3%
S5	1	0.396	99.73	-1.37	10.92	22.6	43.8%
	2	0.407	99.75	1.43	11.05	22.6	43.3%
	3	0.411	99.77	2.22	11.76	22.6	43.6%
	4	0.426	99.89	5.91	10.26	22.7	43.0%
	5	0.406	99.80	1.03	12.31	22.6	43.0%
S5 Mean:		0.409		1.74	11.26	22.6	43.3%
Mean:		0.402			11.36	22.3	45.7%

Table B.19. Dataset of indentation test results, including measured reaction forces and their associated normalized error metrics.

Sample	Test	$k_{crush}[\frac{N}{mm}]$	$R_{Value}^{\%}$	$\Delta_{k_{crush}^{Mean}}^{\%}$	$NRMSE_{RF}^{\%}$	T [°C]	RH%
S1	1	0.294	99.99	-3.68	11.99	21.4	59.9%
	2	0.306	100.0	0.10	7.64	21.4	59.4%
	3	0.295	99.79	-3.39	6.37	21.4	59.7%
	4	0.292	99.71	-4.59	6.77	21.4	59.5%
	5	0.283	99.88	-7.37	9.19	21.4	59.9%
S1 Mean:		0.294		-3.79	8.39	21.4	59.7%
S2	1	0.316	99.84	3.44	10.90	21.7	57.5%
	2	0.274	99.82	-10.28	21.13	21.7	57.2%
	3	0.287	99.71	-6.25	25.87	21.6	57.2%
	4	0.297	99.78	-2.79	29.81	21.5	57.4%
	5	0.290	99.62	-5.00	28.67	21.6	57.4%
S2 Mean:		0.293		-4.18	23.28	21.6	57.3%
S3	1	0.355	100.0	16.15	41.37	21.7	56.4%
	2	0.325	100.0	6.27	29.11	21.7	56.4%
	3	0.333	99.82	8.75	25.97	21.7	56.5%
	4	0.344	99.58	12.58	23.44	21.6	56.5%
	5	0.342	99.60	11.91	23.49	21.8	56.2%
S3 Mean:		0.383		11.13	28.68	21.7	56.4%
S4	1	0.288	99.98	-5.80	12.46	22.0	56.1%
	2	0.283	99.17	-7.47	23.90	21.9	54.9%
	3	0.281	99.99	-7.93	24.23	21.8	55.1%
	4	0.282	99.92	-7.84	26.05	21.9	55.4%
	5	0.290	99.98	-5.27	26.52	21.9	55.8%
S4 Mean:		0.285		-6.86	22.63	21.9	55.3%
S5	1	0.314	99.68	2.65	28.04	22.2	53.7%
	2	0.333	99.56	8.99	21.43	22.2	53.8%
	3	0.316	99.74	3.38	15.04	22.2	53.3%
	4	0.311	99.94	1.87	13.73	22.2	53.4%
	5	0.311	99.96	1.60	12.75	22.2	52.9%
S5 Mean:		0.409		3.70	18.20	22.2	53.4%
Mean:		0.306			20.23	21.8	56.4%

Table B.20. Monte-Carlo parameter fitting results for the NiTiNol material model, listing deviations from nominal values and their influence on simulation accuracy.

Parameter	Nominal value	MC value	Unit
E_A	60000.0	61938.9	[MPa]
E_M	30000.0	27787.3	[MPa]
ϵ_L	0.05	0.049	[-]
σ_{tL}^S	350	389.1	[MPa]
σ_{tL}^E	450	429.5	[MPa]
σ_{tU}^S	150	177.1	[MPa]
σ_{tU}^E	100	91.4	[MPa]

Table B.21. Full results of the scaffold Discretization Error (DE) analysis, comparing stiffness, reaction forces, and computed errors.

GBS [mm]	ElemType	$k_{Scaff} [N/mm]$	$E_k^%$	RF [N]	$E_{RF}^%$	$\sigma_{Max}^{InPlane}$	$E_{\sigma_{Max}}^%$	$\sigma_{Min}^{InPlane}$	$E_{\sigma_{Min}}^{InPlane}$	Time [s]	$\Delta T^%$
1	S4	0.0131	-0.68	0.0537	1.79	0.4871	-5.76	-0.1331	-29.52	474	-99.14
0.5	S4	0.0131	-0.68	0.0530	0.44	0.5022	-2.84	-0.1664	-11.84	1744	-96.84
0.5	S4R	0.0131	-0.28	0.0530	0.44	0.5022	-2.84	-0.1664	-11.84	1609	-87.1
0.25	S4	0.0131	-0.10	0.0528	0.04	0.5146	-0.44	-0.1834	-2.86	11223	-79.7
0.25	S4R	0.0132	-0.08	0.0528	0.04	0.5126	-0.82	-0.1826	-3.28	7115	-87.1
0.125	S4	0.0132		0.0528		0.5169		-0.1888		55198	

Table B.22. Overview of R-values for radial compression test interpolations and resampling across both Compression and Release phases, allowing assessment of data consistency.

Phase	$R_{FD_{Data}}^{30\%}$	$R_{FD_{Model}}^{30\%}$	$R_{FD_{Data}}^{80\%}$	$R_{FD_{Model}}^{80\%}$
Compression	97.94	97.32	87.31	84.33
Release	99.36	98.50	94.85	90.83

Table B.23. Overview of R-values obtained for Crush resistance test interpolations and resampling, structured in a manner similar to Table B.22 to facilitate comparisons across validation tests.

Phase	$R_{Data}^{30\%}$	$R_{Model}^{30\%}$
Compression	99.92	99.70
Release	99.74	97.71

C

LIST OF TABLES

2.1.	Summary of inputs and outputs for each step of the FE model implementation process, from initial geometry processing to final TAVI assembly.	20
2.2.	Discretization parameters applied for the meshing process of the stent and the leaflets models, with details on meshing size, element type selection, and key meshing parameters.	22
2.3.	Summary of interaction modelling parameters applied throughout the FE model implementation process, with details on the specific contact pairs involved and the Simulations in which they are implemented.	23
2.4.	Summary of BCs applied across simulations, detailing constraints and displacements for stent shaping, mechanical tests, and leaflet instertion and interactions, together with the final application simulation.	25
2.5.	Numerical Solver Error (NSE) parameter selection and relative variability ranges investigated as part of the verification process. The table is divided in two parts: the top section shows the parameters involved in the solver setup, while the bottom section shows an overview of the applied contact parameters.	28
3.1.	Nominal and mean values of key geometrical parameters obtained from experimental measurements of five stent specimens and five complete TAVI specimens, along with their standard deviations.	32
3.2.	Experimentally measured friction coefficients and their standard deviations for two material pairs: Aluminium-NiTiNol and Leaflet-Indenter. These values characterize the static friction interactions relevant to the mechanical behavior of the tested components.	34
3.3.	Selected geometrical parameters relative to the metallic stent, as found in the stent model at the end of the Stent Shape Setting simulation and extracted by the Python postprocessing script. compared with their nominal values as provided from the manufacturing company.	37
3.4.	Summary of stiffness values obtained from FE model validation simulations, including radial compression, crush resistance, and indentation tests, with corresponding correlation coefficients	41
3.5.	Numerical solver error analysis results, showing the evaluated radial stiffness k_{NSE} for nominal, minimum, and maximum values of explored solver parameter ranges	41
3.6.	Results of DE analysis (Test 1), comparing four global seed size values (GBS) in terms of evaluated stiffness precision, sensed reaction forces precision and computation time.	42

3.7.	Discretization error analysis results, comparing the performance of different element types under various global seed sizes (GBS) in terms of evaluated stiffness, accuracy, and computational efficiency.	43
3.8.	Discretization error analysis results, examining the influence of the number of elements along the radial thickness (RT) under different element types and global seed sizes (GBS) in terms of stiffness evaluation and computational performance.	44
3.9.	Discretization error analysis, exploration of the influence of the implementation of a biased meshing approach along the structural thickness ST (Test 4). The table compares the Test 4 analysis results with the results from the C3D20R-0.014-32RT-16ST case.	45
3.10.	Discretization error analysis, exploration of the influence of the implementation of a biased meshing approach along the longitudinal direction of the stent feeler (Test 5). The table compares the Test 5 analysis results with the results from the C3D20R-0.014-32RT-16ST case.	46
3.11.	Percentage errors in stiffness and reaction force evaluation from the Scaffold model discretization error analysis. The table provides an overview of Test 1 (variation in global seed size, GBS) and Test 2 (comparison of element types).	48
3.12.	Percentage errors in maximal and minimal in-plane stresses from the Scaffold model discretization error analysis. The table presents results from Test 1 (variation in global seed size, GBS) and Test 2 (comparison of element types).	48
3.13.	Differences in completion time observed in the Scaffold model discretization error analysis, comparing results from Test 1 (variation in global seed size, GBS) and Test 2 (comparison of element types).	49
3.14.	Comparison of mean experimental measurements and FE model geometrical parameters, showing absolute and percentage errors relative to nominal values, as evaluated using a Python post-processing script.	49
3.15.	Results overview of the radial compression resistance test simulation, used to validate the applied NiTiNol material model, including computed stiffness values and RMSE for crimping and release phases.	51
3.16.	Results overview of the crush resistance test simulation (Validation 2), used to validate the obtained NiTiNol stent geometry and complex shaping. The table includes stiffness values, correlation coefficient, percentage error, and NRMSE for compression and release phases.	51
3.17.	Results overview of the indentation test simulation (Validation 3), used to validate the complete TAVI assembly at the end of the scaffold insertion simulation. The table includes stiffness values, correlation coefficient, percentage error, and NRMSE for compression and release phases.	53
3.18.	Overview of R-values from resampling in the indentation test, comparing correlation coefficients between experimental data and the FE model during indentation and release phases.	54
3.19.	Overview of results from the transvalvular pressure simulations, including estimation errors for minimal and maximal cases analyzed in the Sensitivity Analysis and Hypothesis Exploration studies.	55
B.1.	Overview of the data implementation flow for the Stent Frame CAE step, outlining the provided inputs and obtained outputs essential for the computational modeling process.	72
B.2.	Summary of the data flow in the Stent model shaping simulation, listing the initial solid model, applied analysis parameters, and the final geometrical validation results.	72

B.3.	Data pipeline for the Stent model crimping simulation (Step 3), detailing how the model evolves from its solid state to an analyzed crimped configuration, including extracted reaction forces and radial stiffness.	72
B.4.	Implementation details of the half-symmetry model CAE step (Step 4), used to assess deformation and stent-bridge interactions.	72
B.5.	Data implementation flow for the crush resistance test analysis (Step 5), specifying the extracted forces and stiffness values derived from the model response.	72
B.6.	Steps involved in the complete assembly CAE (Step 6), covering the integration of components into the final computational model.	73
B.7.	Simulation flow for leaflet insertion (Step 7), listing how the complete model is updated post-leaflet integration.	73
B.8.	Data flow for the complete assembly CAE step (Step 8), showing the refinement process leading to a finalized computational model.	73
B.9.	Overview of the transvalvular simulation (Step 9), including the physiological mechanical response assessment and reaction force extraction.	73
B.10.	Steps in the indentation probe CAE setup (Step 10), detailing the integration of the indenter probe into the computational framework.	73
B.11.	Data implementation for the indentation simulation (Step 11), specifying extracted displacement and reaction force parameters.	73
B.12.	Summary of the applied transvalvular pressure loading conditions, with reference to time-dependent parameters in Figure 2.11.	74
B.13.	Nominal values and tolerances of the metallic stent and polymeric leaflets geometrical parameters, including relevant post-processing evaluations.	74
B.14.	Comprehensive dataset of geometrical measurements for TAVI stents, including flare diameter, internal diameter, height, and radial thickness, along with their standard deviations.	75
B.15.	Complete leaflet thickness measurements dataset for TAVI valves, reporting mean values across multiple samples under controlled conditions.	75
B.16.	Full dataset of experimentally obtained static friction coefficients for Aluminium-NiTiNol, including mean values and environmental conditions at the time of measurement.	76
B.17.	Dataset of static friction coefficients for Leaflet-Indenter interactions, structured similarly to Table B.16 for consistency in experimental evaluation.	76
B.18.	Complete results from the crush resistance test, detailing reaction force values and their statistical distribution.	77
B.19.	Dataset of indentation test results, including measured reaction forces and their associated normalized error metrics.	78
B.20.	Monte-Carlo parameter fitting results for the NiTiNol material model, listing deviations from nominal values and their influence on simulation accuracy.	78
B.21.	Full results of the scaffold Discretization Error (DE) analysis, comparing stiffness, reaction forces, and computed errors.	79
B.22.	Overview of R-values for radial compression test interpolations and resampling across both Compression and Release phases, allowing assessment of data consistency.	80
B.23.	Overview of R-values obtained for Crush resistance test interpolations and resampling, structured in a manner similar to Table B.22 to facilitate comparisons across validation tests.	80

D

APPENDIX - ADDITIONAL FIGURES

D.1. FIGURES CHAPTER 2 - MATERIALS AND METHODS

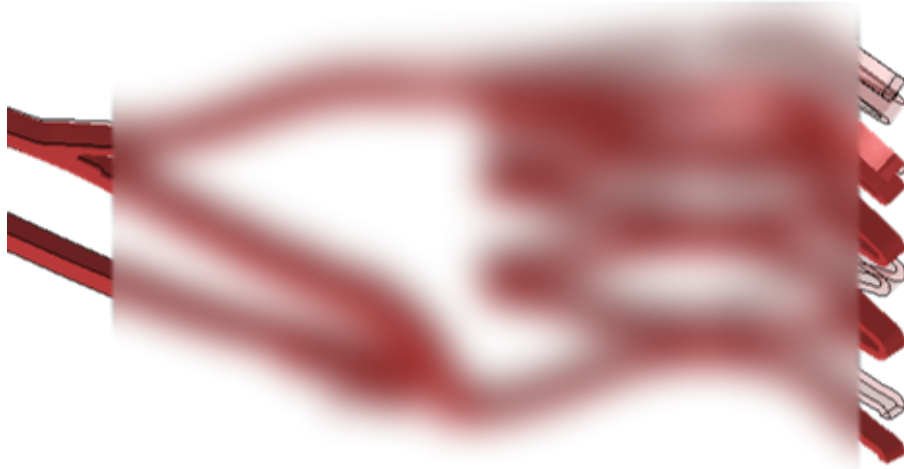


Figure D.1. Difference in flare diameter (FD) of the ring sealing section of the stent before and after scaffold insertion. To preserve intellectual property rights, the stent design has been partially obscured.

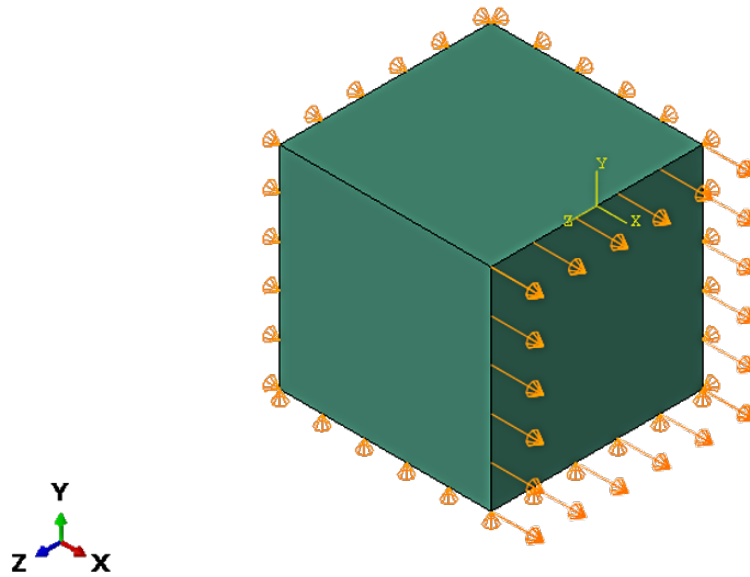
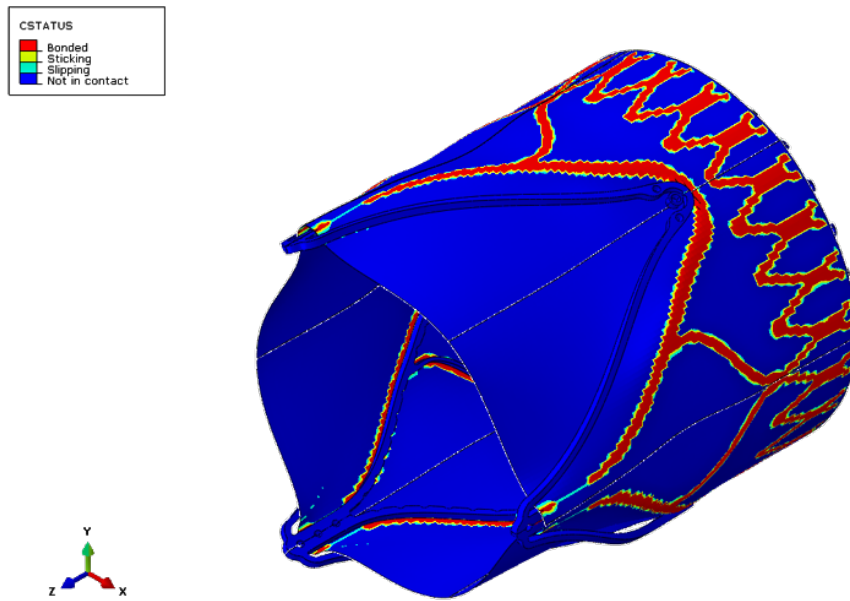


Figure D.2. Abaqus CAE representation of the cubic material calibration model used in this study.



D

Figure D.3. CSTATUS visualization of the contact status between the stent and leaflet models.

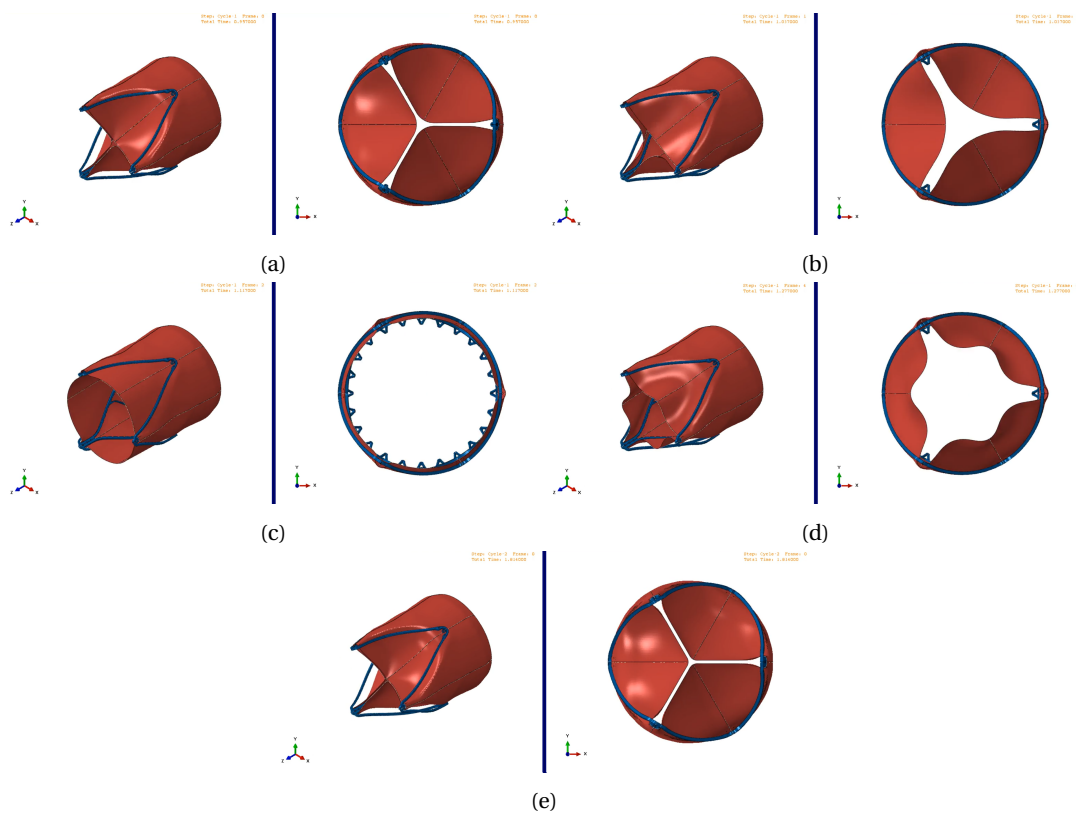


Figure D.4. Sample frames from the cardiac pressure application simulation during one cardiac cycle at different simulation steps: Figure D.4a: End preconditioning step, Figure D.4b: Frame 1, Figure D.4c: Frame 2, Figure D.4d: Frame 4, Figure D.4e: End of cycle/beginning of cycle 2.

D

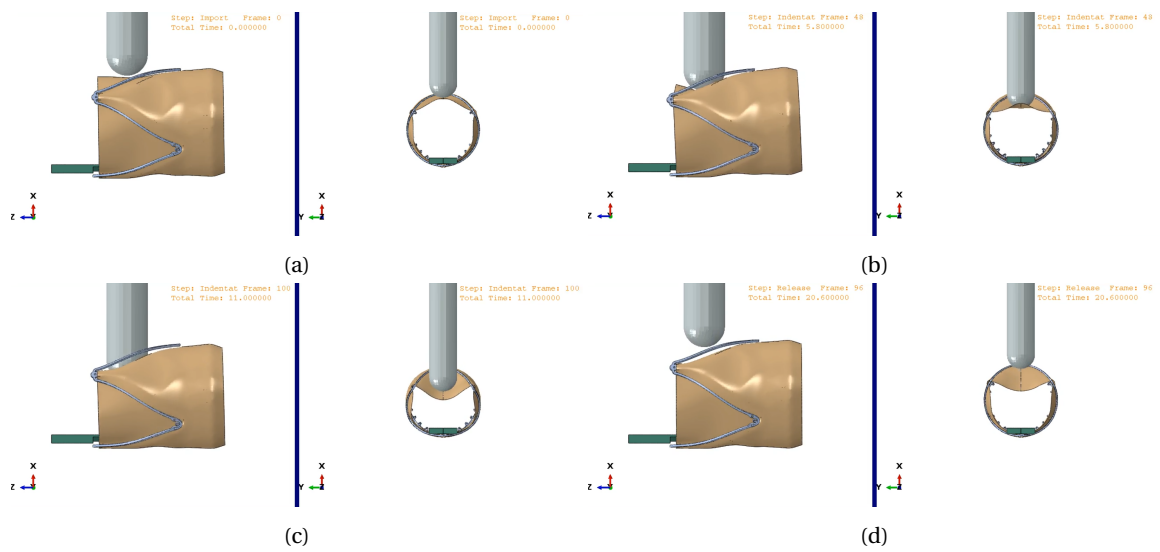
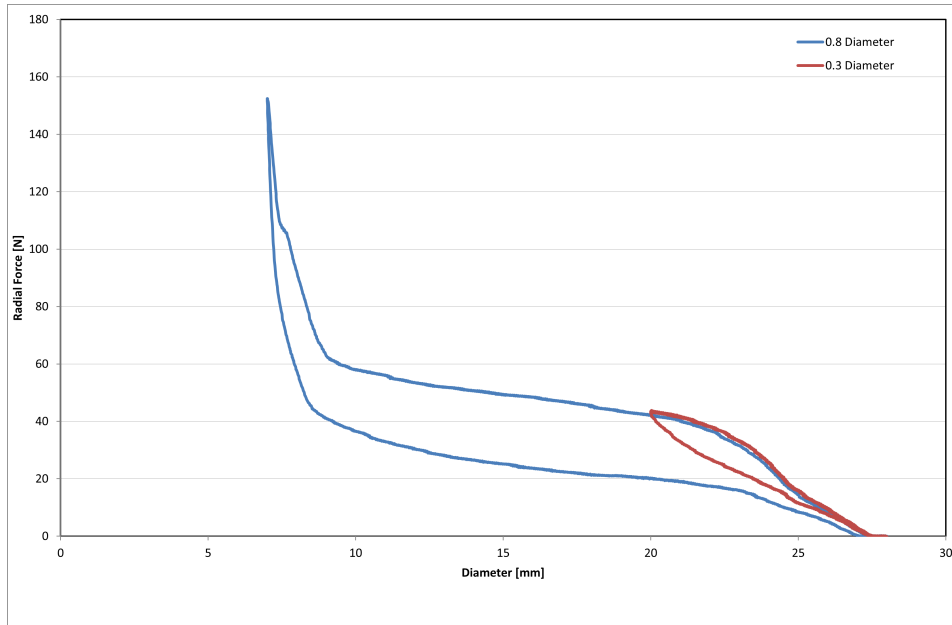


Figure D.5. Stepwise visualization of the indentation test simulation, highlighting the internal folding of the leaflet model: Figure D.5a Import model, Figure D.5b Indentation detail before leaflet folding, Figure D.5c Indentation after leaflet folding, Figure D.5d End of the release phase.

D.2. FIGURES CHAPTER 3 - RESULTS



D

Figure D.6. Reaction force response during the radial stiffness test for the TAVI stent, showing a force spike around an 8 mm diameter due to self-contact at high crimping levels.

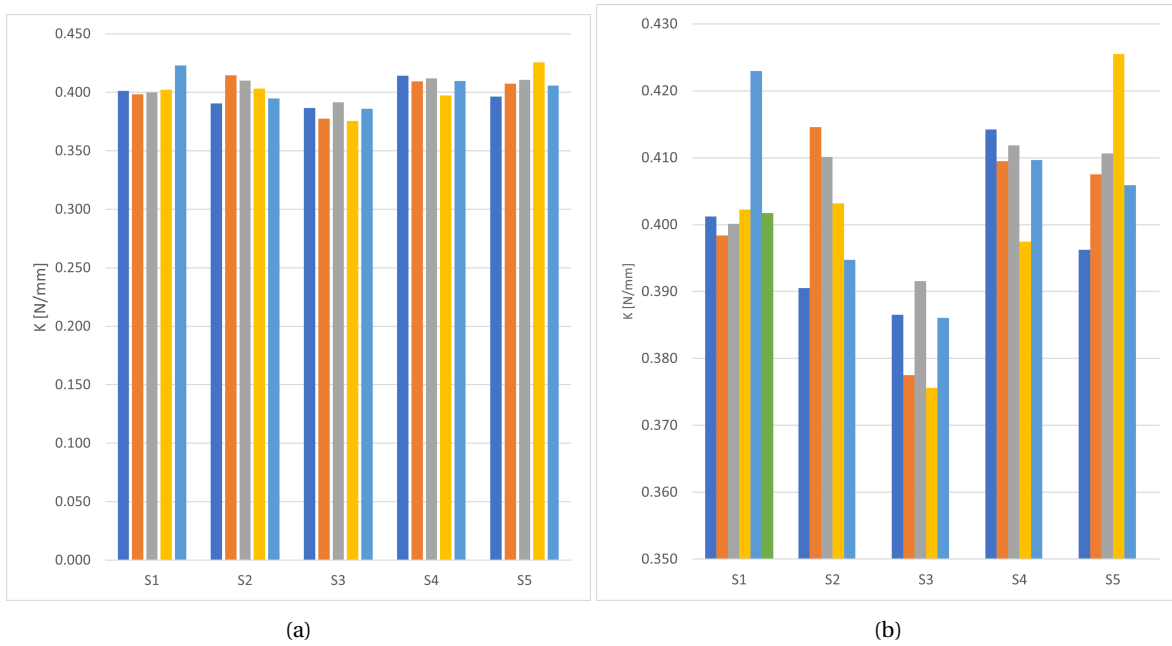


Figure D.7. Evaluated stiffness results from the crush resistance test, per sample, over complete scale (Figure D.7a), and a detail (Figure D.7b).

D

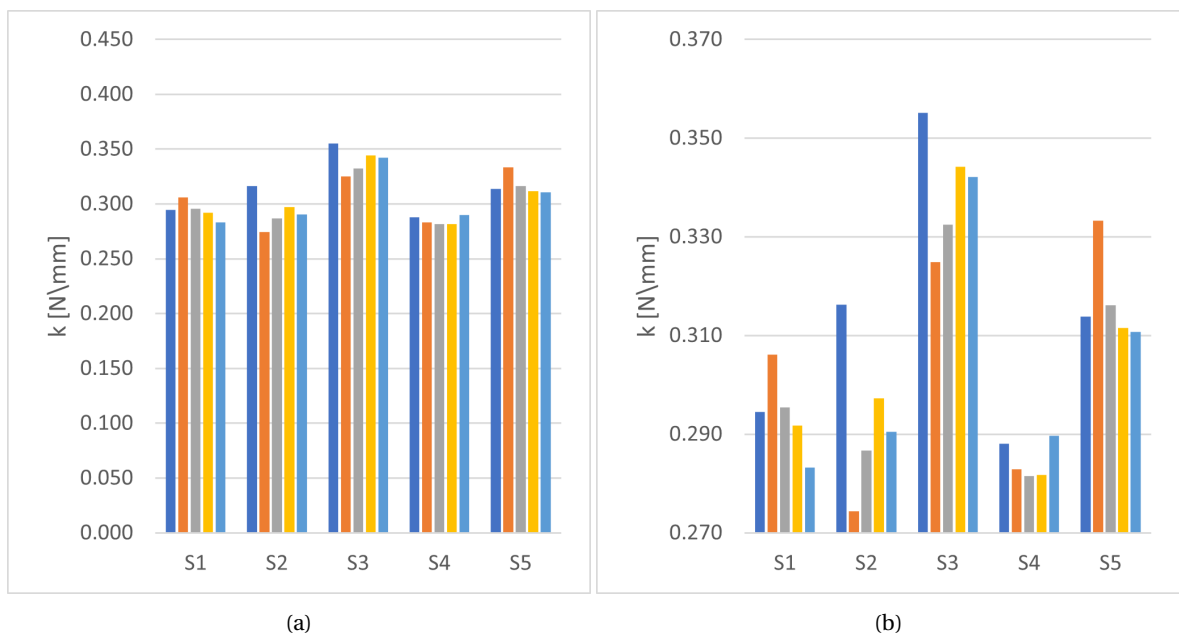
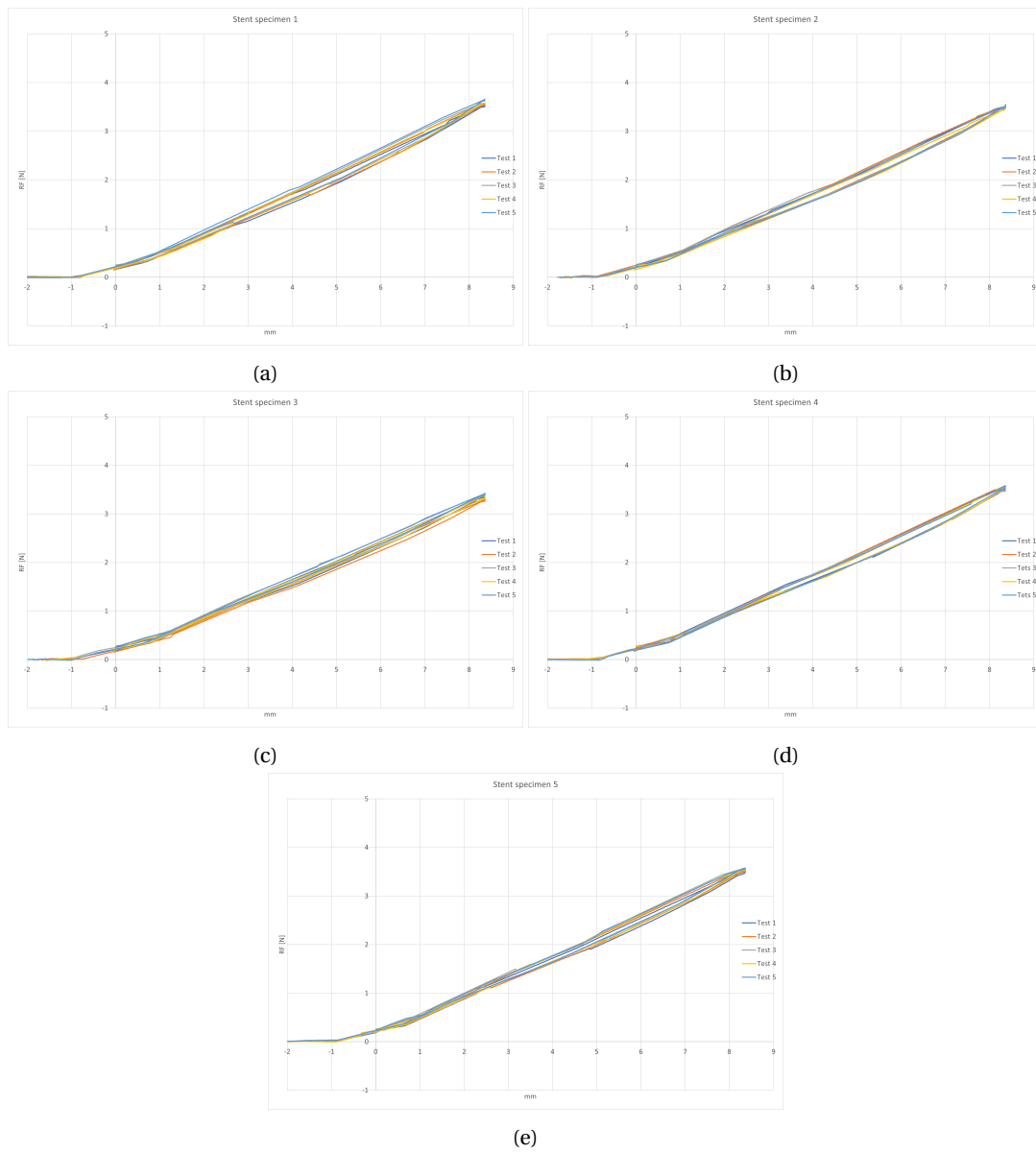


Figure D.8. Evaluated stiffness results from the indentation test, per sample, over complete scale (Figure D.8a), and a detail (Figure D.8b).



D

Figure D.9. Experimental crush resistance test results for each sample: [D.9a](#) Sample 1, [D.9b](#) Sample 2, [D.9c](#) Sample 3, [D.9d](#) Sample 4, [D.9e](#) Sample 5.

D

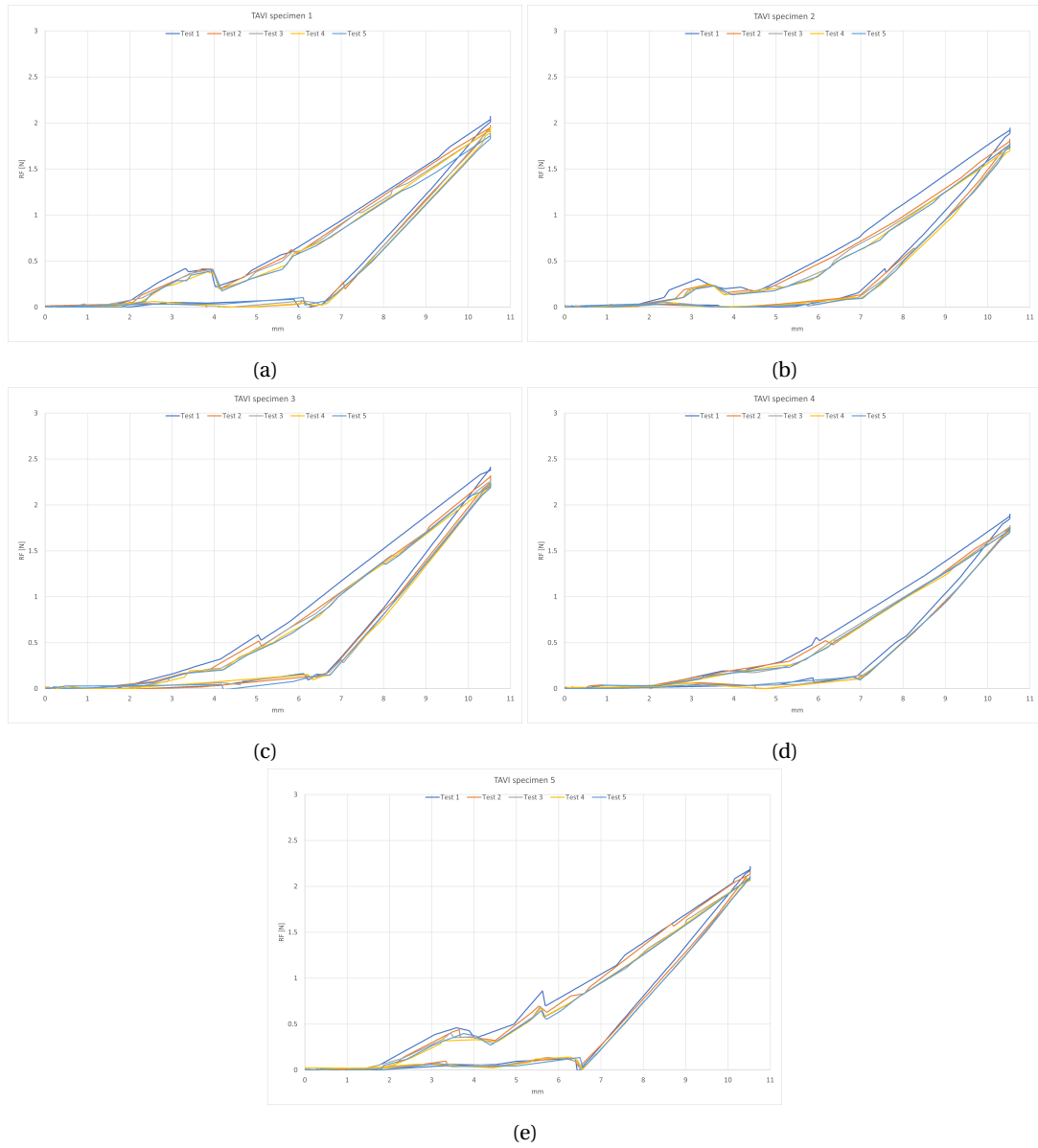
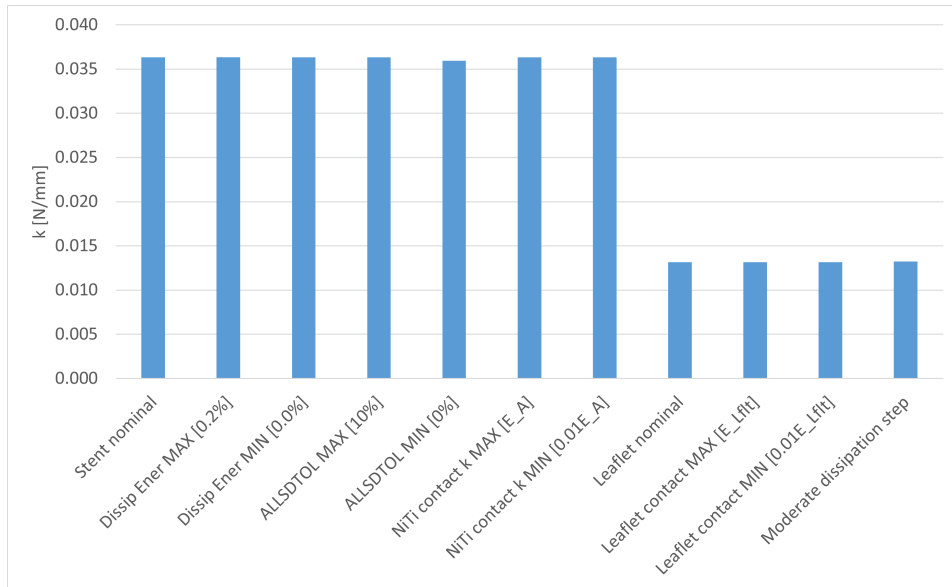
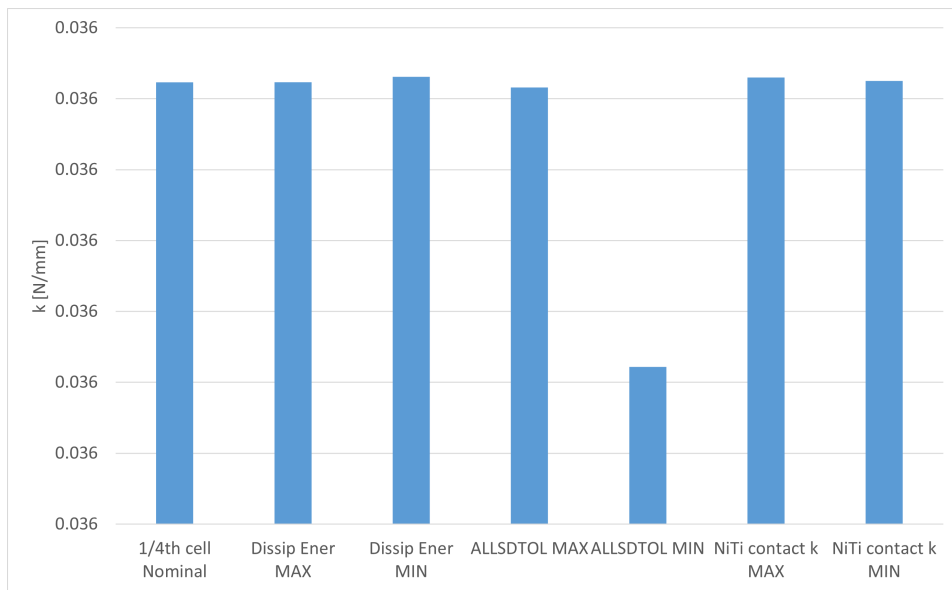


Figure D.10. Experimental indentation test results for each sample: [D.10a](#) Sample 1, [D.10b](#) Sample 2, [D.10c](#) Sample 3, [D.10d](#) Sample 4, [D.10e](#) Sample 5.



(a)



(b)

Figure D.11. Analysis of numerical solver error due to different solver parameters: Figure D.11a Full comparison of stiffness results across tested models in relation to analyzed parameters, Figure D.11b Detailed view of the lower stiffness found for the minimum ALLSDTOL solver parameter, responsible for automatic stabilization.

D

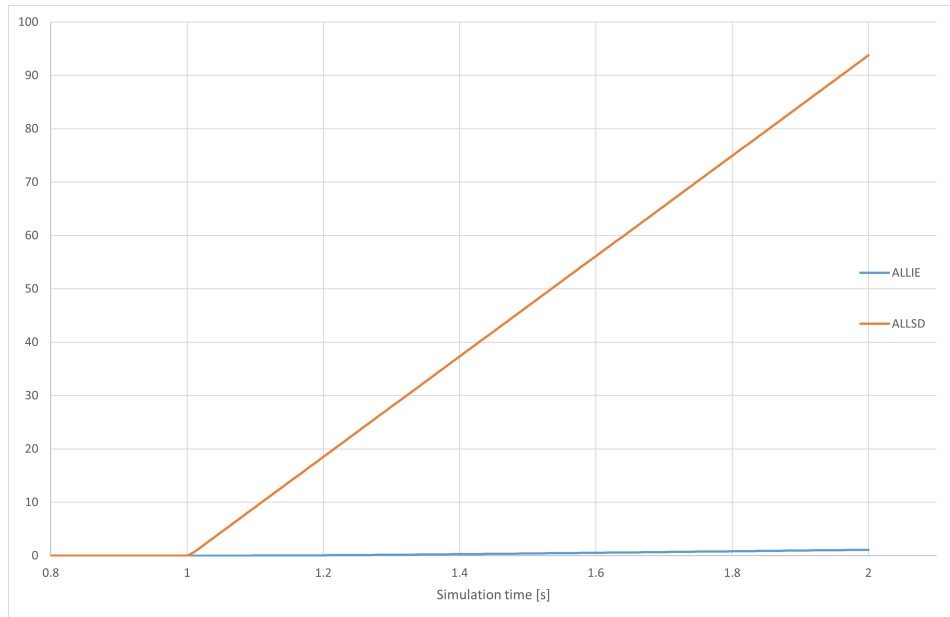


Figure D.12. Visualization of internal energy (ALLIE) and stabilization energy (ALLSD) during the NSE simulation, highlighting the invalidation of results when the ALLSDTOL parameter reaches 0.0% due to the ALLSD/ALLIE ratio exceeding the allowed 5% limit.

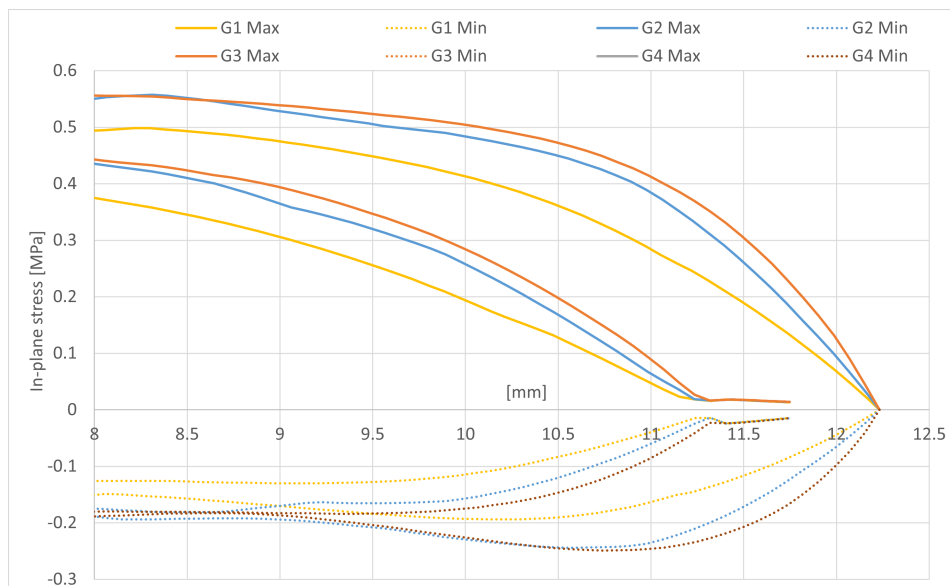


Figure D.13. In-plane stress distribution from the DE scaffold analysis in Test 1.

E

LIST OF FIGURES

1.1.	Examples of commercially available TAVI valves. The Edwards Sapien series (Edwards Lifesciences) are balloon-expandable valves with a cobalt-chromium frame and bovine pericardial leaflets. The Medtronic CoreValve (Medtronic) is a self-expanding valve with a nitinol frame, designed for enhanced adaptability to the native aortic anatomy. These devices are commonly used for treating severe aortic stenosis, as reported in <i>Kheradvar et al.</i> [5].	2
1.2.	Stress-strain response of NiTiNol based on Auricchio's material formulation, illustrating pseudoelastic behavior with phase transformation between austenite and martensite. Adapted from <i>Carbonaro et al.</i> [22].	4
2.1.	Graphical representation of the stent geometrical parameters. Subfigure 2.1a shows the XY plane and a detail of the Radial Thickness RT, while subfigure 2.1b shows the ZY plane and a detail of the flare diameter FD, the internal diameter ID and height H. To preserve intellectual property rights, the stent design has been partially obscured.	8
2.2.	Schematic representation of the inclined plane method for measuring the static coefficient of friction μ_s . This method is widely used in frictional studies to characterize material surface interactions. Adapted from <i>Kuhn and Medlin, Testing Methods for Solid Friction</i> [25].	9
2.3.	Experimental setup for the crush resistance test and indentation test. Subfigure 2.3a shows the Lloyd Instruments LR 5K compression testing machine, while subfigure 2.3b shows the 3D-printed indenter probe.	12
2.4.	Implementation process followed to develop the complete Finite Element model of the TAVI valve, comprehensive of the CAE levels (in orange), the model development simulations (in blue), the validation simulations (in green), and the hypothesis exploration simulations (in white).	14
2.5.	Flat geometry and obtained wrapped solid stent frame model. Figure 2.5a shows the flat geometry as provided by the partner company and imported into Abaqus CAE. Figure 2.5b shows the solid stent frame model obtained from the Python pre-processing script, after solid extrusion and cylindrical wrapping, as imported at the beginning of the Stent Shape Setting simulation. To preserve intellectual property rights, the stent design has been partially obscured.	14
2.6.	XY-plane view of the metallic stent model at the beginning of the radial stiffness test simulation, as obtained at the end of the Stent Shape Setting simulation.	15

2.7.	Half-symmetry model and physical parts for the crush resistance test. Figure 2.7a shows the 3D-printed Bridge part used to secure the valve assembly during the experimental tests. Figure 2.7b shows the initial configuration of the half-symmetry model, completed of the Bridge part model used for fastening, while Figure 2.7c shows the Bridge and the top plate parts lowered by the Python preprocessing script into their final position for the crush resistance test simulation. To preserve intellectual property rights, the stent design has been partially obscured.	16
2.8.	Crush resistance test simulation phases. Figure 2.8a shows the initial configuration of the half-symmetry model at the beginning of the crush resistance test simulation, with the Bridge part and top plate already lowered in their starting positions, while Figure 2.8b shows the model at the end of the compression phase. To preserve intellectual property rights, the stent design has been partially obscured. . .	17
2.9.	Leaflets insertion simulation steps. <i>Import</i> represents the model as imported from previous results. <i>Crimping</i> shows the crimping of the ring sealing section of the stent. <i>Insert</i> depicts the insertion of the leaflets model into the stent structure. <i>Release</i> shows the release of the ring sealing section of the stent.	18
2.10.	Example of a 4.5 bias factor application along the longitudinal direction of the ring sealing structure.	21
2.11.	Pressure curves applied to the internal and external surfaces of the leaflet model in the transvalvular pressure simulation, showing aortic and left ventricular pressures along with the resulting transvalvular pressure difference.	26
2.12.	Half-symmetry leaflets FE model used for DE analysis. The model geometry represents half of the leaflet structure, meshed with shell elements, and is employed to independently evaluate the numerical accuracy and computational stability of the indentation test simulation.	27
3.1.	Box-and-whisker plots of key stent geometrical variables: final diameter (FD), initial diameter (ID), height (H) in 3.1a, and radial thickness (RT) in 3.1b. The plots show median values, interquartile ranges, and whiskers extending to the minimum and maximum measured values.	32
3.2.	Box-and-whisker plot of leaflet thickness (LT) measurements from five complete TAVI specimens, showing the mean, interquartile range, and whiskers extending to the minimum and maximum values.	33
3.3.	Box-and-whisker plot of the measured friction coefficients for both Al-NiTiNol and Scaffold-Polymer friction tests, illustrating the variability and spread of the experimental results across different test samples. The plot includes mean values, interquartile ranges, and whiskers extending to the minimum and maximum values of the evaluated friction coefficients.	34
3.4.	Mean reaction force–displacement curve with experimental standard deviation from the crush resistance test on NiTiNol stent specimens.	35
3.5.	Mean reaction force–displacement curve with experimental standard deviation from the indentation test on complete TAVI valve specimens.	36
3.6.	Box-and-whisker plot of evaluated experimental stiffness values from crush resistance and indentation tests, displaying mean values, interquartile ranges, and whiskers extending to the minimum and maximum measured values.	37
3.7.	Steps of the Stent Shape Setting simulation, including the used shaping surfaces. The detail marked via a red square over the XY-plane view on the left highlights the top tip of the metallic stent model, where RT is evaluated by the Python postprocessing script.	38

3.8.	Stress-strain curves of the NiTiNol material, comparing experimental data from the partner company (dotted lines) with Monte Carlo parameter fitting results (solid lines)	38
3.9.	Reaction force vs. flare diameter curve from the FE validation models of radial compression tests, comparing the structural response under 30% and 80% original diameter reduction conditions.	39
3.10.	Reaction force vs. top plate vertical displacement curve from the FE simulation of the crush resistance test on the stent model, illustrating the progressive stiffening behavior of the structure.	40
3.11.	Reaction force - indenter probe displacement curve obtained for indentation test simulation, together with the characteristic small bump observed between 1 - 3 mm indentation and attributed to the internal folding of the polymeric leaflets	40
3.12.	Stent model discretization error analysis, Test 1 results. The radial displacement - reaction force curves as found for the four different GBS size tested. Figure 3.12a shows the complete RF-FD curves, while Figure 3.12b focuses on the overshoot noticeable for the coarsest mesh at the beginning of the transformation phase characteristic plateau.	42
3.13.	Stent model discretization error analysis Test 2 results. Figure 3.13a shows the percentage error in stiffness evaluation as depending from the element type, while Figure 3.13b gives an overview of the completion time (in seconds) as a function of the element type.	43
3.14.	Stent model discretization error analysis Test 3 results. Figure 3.14a shows the percentage error in stiffness evaluation as depending from the number of elements along RT, while Figure 3.13b gives an overview of the influence of the number of elements along RT over the completion time (in seconds).	44
3.15.	Stent model discretization error analysis Test 4 results. Figure 3.15a shows the percentage error in stiffness evaluation as depending from the bias factor along ST, while Figure 3.14b gives an overview of the influence of implementing a biased approach along ST over the completion time (in seconds).	45
3.16.	Stent model discretization error analysis Test 5 results. Figure 3.16a shows the percentage error in stiffness evaluation as depending from the application of a bias factor along the longitudinal direction of the stent feeler, while Figure 3.16b gives an overview of the influence of implementing a biased approach along the feeler over the analysis completion time (in seconds). For an easier readability of Figure 3.16b, the completion time relative to the C3D20R elements, uniform mesh has been neglected.	46
3.17.	Results overview of the Scaffold Discretization Error analysis Test 1. Figure 3.17a shows the percentage error on the maximal and minimal in-plane stresses as per function of the global mesh seed sizes (1, 0.5 and 0.25), while Figure 3.17b shows the influence of the global mesh size on the analysis completion time, in seconds.	47
3.18.	Results overview of the Scaffold Discretization Error analysis, Test 2. The influence of the element type over the model accuracy in accurately representing the maximal and minimal in-plane stresses is shown in Figure a, while Figure 3.18b shows the element type influence over the analysis completion time, in seconds.	48
3.19.	Reaction force - flare diameter curves, as found in the Radial compression resistance test simulations for both the 30% and 80% FD reduction, compared with the experimental results as provided by the external partner company. Figure 3.19a highlights the comparison of the obtained 30% curves, while Figure 3.19b reports a comparison of the two 80% reduction curves.	50

3.20.	Comparison between the mean reaction force - displacement curve found for the crush resistance test, complete with the statistical standard deviation, and the curve obtained via FE simulation, as part of the validation process of the obtained geometrical configuration of the NiTiNol stent.	52
3.21.	Comparison between the mean reaction force - displacement curve found for the Indentation test (with relative standard deviation) and the curve obtained via FE simulation, as part of the validation process of the complete TAVI model.	53
3.22.	Reaction forces - displacement curve evaluated at the tip of the stent model. Figure 3.22a shows the obtained curves for the Sensitivity analysis exploration, in which the NiTiNol parameters have been varied within the 5.24% NRMSE range derived from the MC study. Figure 3.22b shows the results of the broader NiTiNol parameters space explored as part of the Hypothesis exploration analysis.	56
A.1.	Aluminum bottom plate, threaded with M6 holes, as designed in SolidWorks as part of this study (SolidWorks 2023, Dassault Systèmes [7]). All distances are in millimeters.	68
A.2.	Bridge CAD model developed in SolidWorks as part of this study (SolidWorks 2023, Dassault Systèmes [30]), shown in an alternative view including 3D-printer raisers (in grey and different blue tonalities), which were later removed from testing.	68
A.3.	Developed Bridge CAD model in SolidWorks (SolidWorks 2023, Dassault Systèmes [7]), shown in a tridimensional view (A.3a) along with three orthogonal projections: XZ side view (A.3b), XY side view (A.3c), and YZ side view (A.3d).	69
A.4.	Complete fastening device assembly developed in SolidWorks as part of this study (SolidWorks 2023, Dassault Systèmes [30]), including the Bridge (light green), the bottom plate (dark green, detailed in Figure A.1), the Holder (red) ensuring half-model symmetry by restricting XY-axis rotation, and the 3D-printed raisers (removed in testing, detailed in Figure A.2).	69
D.1.	Difference in flare diameter (FD) of the ring sealing section of the stent before and after scaffold insertion. To preserve intellectual property rights, the stent design has been partially obscured.	86
D.2.	Abaqus CAE representation of the cubic material calibration model used in this study.	86
D.3.	CSTATUS visualization of the contact status between the stent and leaflet models.	87
D.4.	Sample frames from the cardiac pressure application simulation during one cardiac cycle at different simulation steps: Figure D.4a: End preconditioning step, Figure D.4b: Frame 1, Figure D.4c: Frame 2, Figure D.4d: Frame 4, Figure D.4e: End of cycle/beginning of cycle 2.	87
D.5.	Stepwise visualization of the indentation test simulation, highlighting the internal folding of the leaflet model: Figure D.5a Import model, Figure D.5b Indentation detail before leaflet folding, Figure D.5c Indentation after leaflet folding, Figure D.5d End of the release phase.	88
D.6.	Reaction force response during the radial stiffness test for the TAVI stent, showing a force spike around an 8 mm diameter due to self-contact at high crimping levels.	89
D.7.	Evaluated stiffness results from the crush resistance test, per sample, over complete scale (Figure D.7a), and a detail (Figure D.7b).	89
D.8.	Evaluated stiffness results from the indentation test, per sample, over complete scale (Figure D.8a), and a detail (Figure D.8b).	90
D.9.	Experimental crush resistance test results for each sample: D.9a Sample 1, D.9b Sample 2, D.9c Sample 3, D.9d Sample 4, D.9e Sample 5.	91

D.10.	Experimental indentation test results for each sample: D.10a Sample 1, D.10b Sample 2, D.10c Sample 3, D.10d Sample 4, D.10e Sample 5.	92
D.11.	Analysis of numerical solver error due to different solver parameters: Figure D.11a Full comparison of stiffness results across tested models in relation to analyzed parameters, Figure D.11b Detailed view of the lower stiffness found for the minimum ALLSDTOL solver parameter, responsible for automatic stabilization.	93
D.12.	Visualization of internal energy (ALLIE) and stabilization energy (ALLSD) during the NSE simulation, highlighting the invalidation of results when the ALLSDTOL parameter reaches 0.0% due to the ALLSD/ALLIE ratio exceeding the allowed 5% limit.	94
D.13.	In-plane stress distribution from the DE scaffold analysis in Test 1.	94

